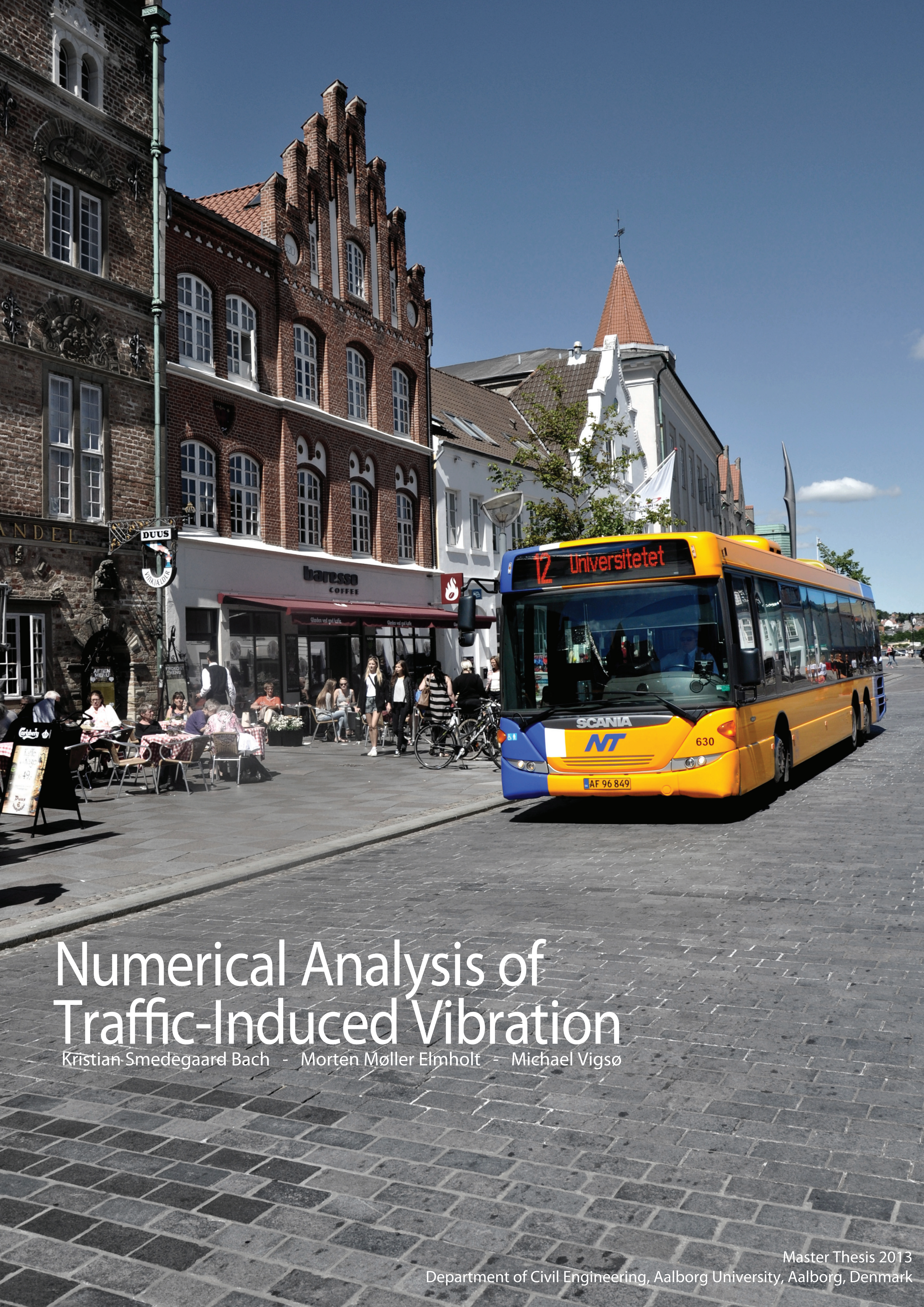

Numerical Analysis of Traffic-Induced Vibration

Kristian Smedegaard Bach - Morten Møller Elmholt - Michael Vigsø

Master Thesis 2013
Department of Civil Engineering, Aalborg University, Aalborg, Denmark

AALBORG UNIVERSITY
Students' report

The School of Engineering and Science
Study Board of Civil Engineering
Sohngårdsholmsvej 57
9000 Aalborg
http://www.ses.aau.dk

Title:
Numerical Analysis of Traffic-Induced Vibration

Project:
Master Thesis

Project period:
4th semester MSc
February 2013 - June 2013

Students:
Kristian Smedegaard Bach
Morten Møller Elmholt
Michael Vigsø

Supervisor:
Lars Vabbersgaard Andersen

Project Review pages: 38

Article Collection pages: 30

Background Report pages: 75

Completed:
Monday the 10th of June 2013

Synopsis:

The following master thesis presents a study of traffic-induced vibration problems. The main body of the thesis consists of three articles. The first article, *A fully coupled finite-element model for prediction of traffic-induced vibration in buildings*, presents methods for constructing a finite-element model for estimating vibration in buildings caused by traffic. The finite-element model includes a two-storey frame building, a soil body and a moving vehicle. Different approaches for coupling of the systems are presented and an example is provided.
The second article, *Parameter studies of traffic-induced vibration using a finite-element model*, contains the outcome of a parameter study using the finite-element model described in the first article. The study presents an analysis of how different parameters such as surface composition, vehicle properties and soil stratification influence the generation of vibrations.
The third article, *Considerations concerning finite-element modelling of traffic-induced vibration*, concerns aspects regarding dynamic interaction effects and quantifies the consequences of treating the systems as decoupled. Futhermore a three-dimensional finite-element model is constructed and a qualitative comparison is made with the two-dimensional model.
The three articles are accompanied by a project review and a background report containing the main considerations during construction of the models.

Preface and reading guide

The thesis is divided into three parts: an article collection, a project review and a background report. The background report is meant as an appendix and contains considerations made during the construction phase. Each of the three articles can be read independently of the others. Hence, some repetitions may be expected.

Within the articles, background report and project review, references will appear, and these will be collected in a bibliography in the back of each paper. Sources are presented when it is relevant using the *Harvard method*, where a source in the text is referred to as [Surname, Year]. If there is more than two authors, the first is mentioned while the remaining are indicated by 'et al.'. If the same author appears several times, the surnames will also be alphabetically ordered. A reference leads to the bibliography, where books are listed with author, title, edition and possible publishers, while websites are indicated by author, title and the date where it is used.

Figures and tables are numbered according to sections/chapters. Thus, the first figure in Section 3 is number 3.1, the second is number 3.2, etc. Explanatory text for figures and tables, can be found under and above the given figures and tables, respectively. Formulas, equations and expressions are indicated by number in parentheses, where the numbering is similar to figures and tables. All written material can be found in the enclosed DVD.

Kristian Smedegaard Bach

Morten Møller Elmholt

Michael Vigsø

Date: Monday the 10th of June 2013

Abstract

Traffic-induced vibration in an urban environment can be an issue for neighbouring buildings and residents. Modifications in the pavement or construction of speed bumps may induce inconvenient vibration and in rare cases cause damage in buildings. Today's methods, used for estimation of vibration from traffic, are mainly based on empirical knowledge and are relatively insecure. In the literature several examples can be found in which traffic-induced vibration and the response in nearby buildings are modelled numerically. However, no distinct consensus appears in the way the models are constructed, and the uncertainties are generally significant. The following master thesis with the title *Numerical Analysis of Traffic-Induced Vibration* deals with the construction of a dynamic finite-element model for simulation of traffic-induced vibration. The model includes a vehicle, a road, a soil body and a building.

A plain two-dimensional finite-element model of a soil body with absorbing boundary conditions is constructed and a two-storey building is attached. A generic vehicle model is developed in which the wheels and the suspension system are modelled as discrete spring-dashpot-mass systems. Two types of surfaces are considered for the road: a plane surface with different types of speed bumps and a cobblestone pavement defined by stochastic parameters. The interface between the vehicle and the soil body is modelled using Mindlin beam elements supported by interface elements and Kelvin foundations.

A key issue in the project is to examine the interaction effects between vehicle and soil body and between soil body and building. The interaction between vehicle and soil body is modelled in the time domain using three different time integration schemes: A decoupled, an explicit and an implicit scheme. The interaction between soil body and building is modelled by including the finite-element model of the soil body and the building in the same system.

The parameters included in the model are calibrated for a reference case in which a three-axel vehicle similar to a Scania City bus runs across a soil of silty clay. A parameter study is conducted in order to clarify, which parameters are essential for the magnitude of the vibration in the building. Studies are performed for both speed bumps and cobblestone pavements. The necessity of coupling between the individual sub parts of the model is examined by conducting simulations for both a coupled and a decoupled model. Ultimately a three-dimensional model is developed for comparison in order to investigate whether a two-dimensional model is applicable for simulation of the three-dimensional vibration problem.

Resumé

Vibrationer fra trafik i bymiljøet kan belaste de omkringliggende bygninger og genere beboere. Ændringer af vejbelægning eller etablering af fartbump har i visse tilfælde vist sig at skabe uhensigtsmæssige vibrationer eller i specielle tilfælde forårsaget skade på bygninger. De nuværende metoder til at estimere belastningen fra trafikvibrationer baserer sig i høj grad på empiri og er relativt usikre. I litteraturen findes flere eksempler på, hvordan trafikvibrationer og disses indvirkninger på bygninger kan modelleres numerisk. Der ses dog ikke nogen konsensus omkring metoder for at opstille disse modeller, samtidig med at usikkerheden i modellerne er relativ stor. Dette afgangsprojekt med titlen *Numerisk Analyse af Trafikinducerede Vibrationer* omhandler derfor opstillingen af en koblet dynamisk finite element model med køretøj, vej, jordlegeme og bygning for beregning af vibrationer fra trafik.

En plan finite element model af et jordlegeme med absorberende randbetingelser opstilles med en bygning modelleret som en toetages rammekonstruktion, hvor fundamentet er sammenkoblet med jorden. En generisk køretøjsmodel opstilles, hvor både hjul og affjedringssystem modelleres med et diskret fjeder, dæmper og masse system. Vejbelægningen kan opbygges som enten en flad overflade med flere typer af fartbump, konstrueret efter Vejdirektoratets anvisninger eller som en stokastisk model af en brostensbelægning. Grænsefladen mellem vejbelægning og jordlegeme opbygges af bjælkeelementer, som understøttes delvist interfaceelementer og Kelvin-understøtninger.

En central del af projektet omhandler koblingen mellem køretøj og jordlegeme og mellem jordlegeme og bygning. Interaktionen mellem køretøj og jordlegeme evalueres i tidsdomænet ved hjælp af tre forskellige fremgangsmåder: en dekoblet, en eksplicit og en implicit metode. Interaktionen mellem jordlegeme og bygning modelleres ved at koble bygningens fundament sammen med jordlegemet.

Parametrene der indgår i modellen kalibreres til et referencetilfælde, hvor en treakslet Scania bus passerer et jordlegeme af siltet ler. Et parameterstudie udføres for at belyse hvilke parametre, der er essentielle for ændringer i det oplevede vibrationsniveau på første sal af en bygning, når en bus passerer et fartbump eller en brostensbelægning foran bygningen. Nødvendigheden af at modellere koblingen mellem de forskellige dele af modellen undersøges ved at dekoble de enkelte led af modellem og sammenligne resultaterne med den samlede model. En tilsvarende tredimensionel model af problemet opstilles for at undersøge begrænsningerne i at anvende en todimensionel model.

Introduction

Introduction

Sound and vibration is one of the major fields within civil engineering. Mechanics, signal processing and electrical engineering are only a part of the subjects in which the theory of waves and propagation constitute the principal matter. The majority of vibration propagating around us are insensible to human beings due to the frequency of the waves. Typically, the acoustic range is defined from 20 Hz to 20 kHz, and frequencies below and above are denoted infrasound and ultrasound, respectively. Especially ultrasound is utilized in a wide range of applications such as human medicine and ultrasonic testing, see Figure 1.

The detection of sound and vibration depends on both the frequency and the magnitude of the oscillations. The magnitude of oscillations is typically described based on a reference value using the decibel scale. For sound, a decibel level of 40 is comparable to the noise of rain drops, while a decibel level of 110 can be experienced at a rock concert [Grand, 2013]. The perception of sound and vibration is highly depended on the affected person. However, for extreme cases such as in Figure 2, the oscillations are generally unpleasant.

Vibrations from earthquakes are unusual events in the northern part of Europe. In Denmark, vibration problems are typically caused by construction work such as pile driving or from heavy vehicle traffic. Traffic-induced vibrations can be generated if a vehicle crosses an irregularity in the road. Irregularities such as man holes, speed bumps and cobblestones are the most common causes of vibrations. In practical engineering, issues regarding vibration from traffic and construction work are typically dealt with in a non-precautions manner. The procedure is to monitor the vibration of nearby structures and take action if the vibrations exceed a critical level.

The method is generally inexpedient as a vibration problem may not be discovered before the relevant project is completed. The cobblestone pavement at Boulevarden in Aalborg is an example of this. In 2005 the asphalt pavement was replaced by a relatively expensive cobblestone pavement from China, see Figure 3. Boulevarden is used for public transportation and the bus transport induced vibrations in the surrounding shops and cafes. The municipality received several complaints from the residents of neighbouring buildings, and after some time the problems were described and discussed in the local media. In 2008 the cobblestones were removed for most of the

Figure 1. Application of ultrasound: (left) medical scanning of fetus [UPMC, 2013], (right) ultrasonic testing of pipeline [NDT, 2013].

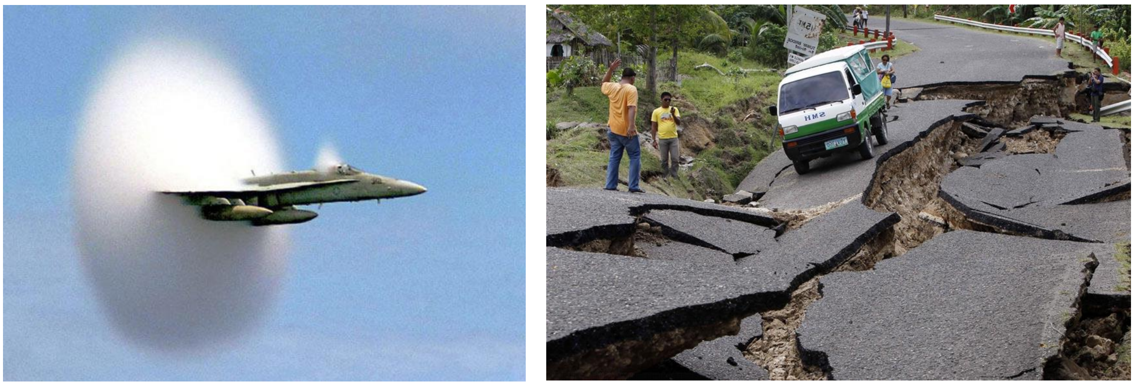

Figure 2. Extreme oscillations: (left) jet plane breaking the sound barrier [US, 2013], (right) consequences from earthquake in the philippines [NBC, 2012].

stretch and the asphalt pavement was reconstructed [Nordjyske, 2012]. The expenses connected to the episode were comprehensive and could possibly have been avoided if a dynamic analysis of the problem had been conducted in the design phase. The case from Aalborg has served as inspiration for the following project description.

Project Description

The project investigates traffic-induced vibration through road and soil, and analyses the effect for persons in neighbouring buildings. A two-dimensional dynamic finite-element model is constructed to include vehicle, soil and building in a single coupled model in order to investigate the interaction effects between the different modules. Different litterature, current models and practice are outlined and compared with the finite-element model in order to examine whether or not, it is necessary to use a coupled model, or the different modules, vehicle, soil and building can be modelled separately.

Figure 3. Photo from Boulevarden in Aalborg.

Project Review

Project Review

The following chapter provides a brief review of the project based on the individual parts including three articles, a background report and electronic material. The articles are reproduced in this paper, while the background report can be read from the enclosed DVD along with the electronic material. Although the three articles can be read separately, the following order is recommended in order to achieve a chronological impression.

Article # 1

The article denoted *A fully coupled finite-element model for prediction of traffic-induced vibration in buildings* contains a detailed description of the model developed for simulation. The three-dimensional problem is simplified to a two-dimensional model containing a vehicle, a road, a soil body and a building, see Figure 4. Each sub part of the model is described and the selected element types are outlined.

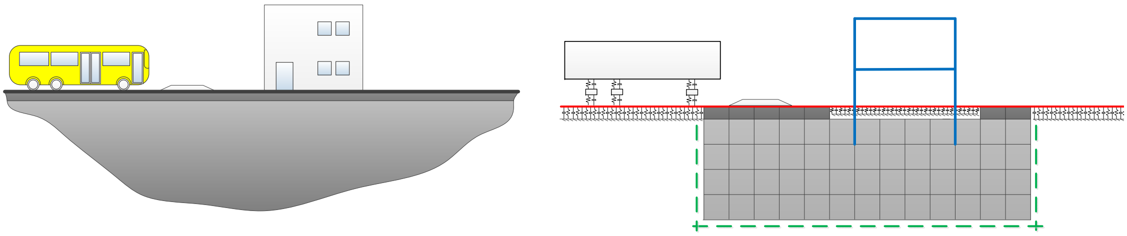

Figure 4. (left) Plane view of the 3D problem, (right) Simplified 2D model used for simulation.

The vehicle travels with constant velocity across the surface of the road and it is therefore insufficient to assemble a single system matrix. The simplest method, to implement the motion of the vehicle, is to use two separate independent systems in which forces from the vehicle are inserted as external forces on the road. Consequently, the simple method does not account for interaction between the moving vehicle and the deforming road. In order to evaluate the effect of interaction, two time integration schemes are developed. An explicit scheme using two interacting system matrices and an implicit scheme in which the system matrices are updated continuously.

Two types of surface irregularities are considered in the articles. Three different types of speed bumps, described deterministically, and a cobblestone pavement, described stochastically are analysed. In the first article, the speed bumps are considered and it is found that a trapeze shaped speed bump causes higher vibrations in neighbouring buildings compared to sinus and circle bumps. The sinus bump resulted in lower vibrations in the building but also in the vehicle, whereby the bump is less effective as a speed limiting precaution. In Figure 5 a snapshot is given from a simulation with the trapeze bump.

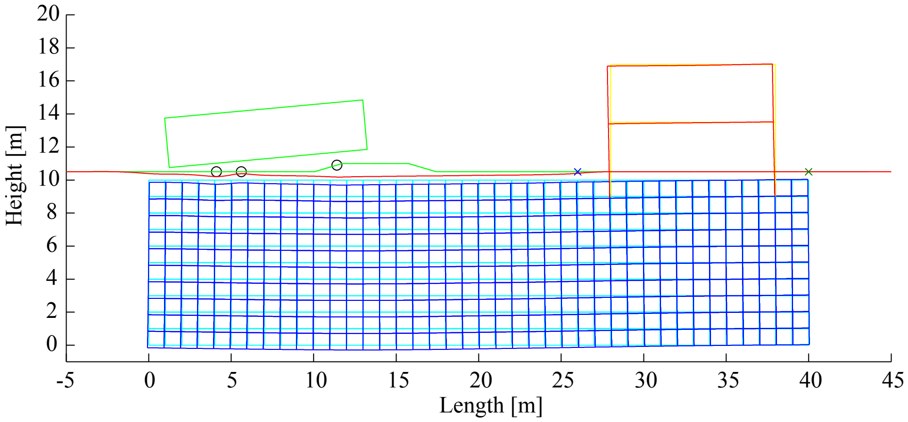

Figure 5. Snapshot from simulation with trapeze bump.

Article # 2

In the article denoted *Parameter studies of traffic-induced vibration using a finite-element model* the model described above is used to quantify the influence on vibration for different parameters. In order to quantify the vibrations, simulations are conducted in which accelerations at the first floor of the building are measured. Residents in the building will be exposed to whole-body vibrations which can cause discomfort at high levels. The maximum transient vibration value based on the frequency weighted running root mean square acceleration is used as a quantitative measure of the vibration.

The surface profile of a cobblestone pavement is considered in the study. Due to similarity of the cobblestones, resonance can occur in both the vehicle and in the building. Simulations are conducted in which the velocity of the vehicle is calibrated to match different critical frequencies, e.g. the natural frequency of the floor division in the building or the frequency causing resonance in the axels of the vehicle. The studies demonstrate that parameters such as the variation in cobblestone length and the damping ratio of the vehicle are essential to the amplification of vibration while the properties of the soil body have a secondary influence.

Article # 3

The third article *Considerations concerning finite-element modelling of traffic-induced vibration* deals with the validity of the finite-element model. Several simplifications are made when the real-case scenario is approximated by the model in Figure 4. Some of the more comprehensive simplifications are the assumptions regarding soil behaviour and homogeneity, the lack of shell elements in the building and the transition from three to two dimensions. The effect of the simplifications can in most cases be diminished by increasing the complexity of the model at the cost of computation time.

An improvement is made compared to similar studies as the effects of interaction are implemented. Interaction between vehicle and road has shown to be significant in case of wide span bridges but in the case of a soil-supported road the effects have shown to be negligible. Deviations between the interaction method and the simple method using separate systems only appear for unrealistically soft soil. However, the interaction effects between the soil body and the building have proven to be significant, especially for soft soil types.

In the second part of the article, a three-dimensional (3D) model is constructed to simulate the

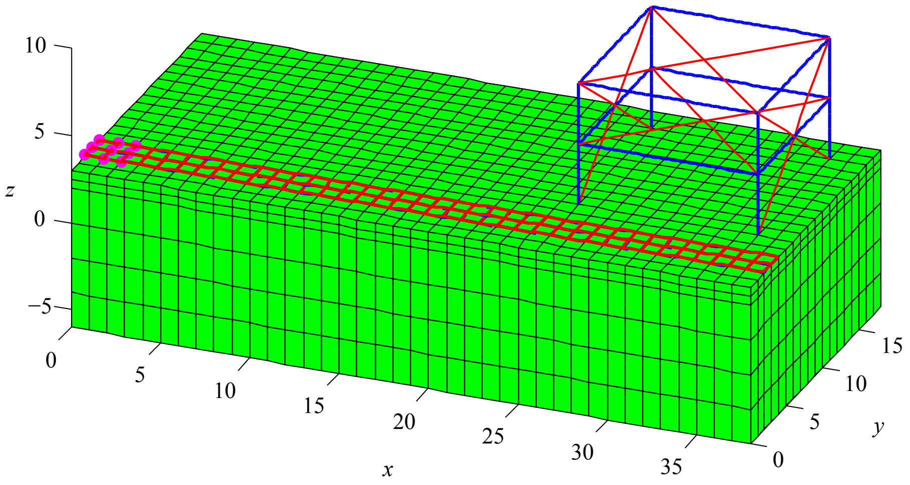

Figure 6. 3D model used for evaluation of the 2D model.

vibration problem, see Figure 6. In general the 3D model requires a vast amount of computational power compared to the two-dimensional (2D) model and it is therefore unsuitable for parameter studies. The scope of the study has been to evaluate the deviations between the two models and to assess whether or not the 2D model is applicable for simulation of traffic-induced vibration. Based on simulations of similar cases in both models it has been found that the amplitudes of the vibrations are overestimated significantly in the 2D model. However, the change in vibration due to a change in a parameter is comparable for the two models, whereby the 2D-model is applicable for parameter studies.

Background Report

The primary scope of the background report is to validate the individual sup parts of the finite-element model and to elaborate the theory behind it. The chapters in the report and the content within are outlined in the following.

Vehicle Model

The system matrices for the vehicle are derived and relevant assumptions are described. The procedure for implementation of movable supports are explained and a simulation is conducted.

Vehicle-Road Interaction

The system matrices for the Bernoulli beam finite-element are presented and the procedure for nodal interpolation is explained. A numerical model of a simply supported beam is constructed and static deformation and frequencies of eigenvibrations are compared to analytical expressions. The use of a surface profile is introduced and the computational procedure for modelling the contact surface between wheel and road is described. The two methods of implementing the interaction are explained and a simple example is conducted for a single-degree-of-freedom vehicle crossing a bridge.

Soil-Building Interaction

The chapter contains a detailed description of the simulations supporting the first part of article 3. Deviations between the interaction procedures are quantified for different soil properties. Three different procedures for evaluating the natural frequencies of the building are presented and evaluated. Simulations are conducted in which the soil body and the building are modelled both coupled and decoupled.

Two-dimensional elements

The properties and the system matrices for the quadrilateral eight-noded continuum elements used in the model are presented. To validate the elements a cantilever beam is modelled and static deformation and frequencies of eigenvibrations are compared to analytical expressions. A more complicated case is set up in which a harmonic line load acts at the top of a soil body. The same analysis is performed in Plaxis and the results are compared both with and without transmitting boundary conditions.

Transmitting Boundary Conditions

The theory behind transmitting boundary conditions in a finite-element model is explained and the procedure for implementation during assembly of the system matrices is described. The functionality of the boundaries is tested using simple models in which pure shear and pure pressure waves are generated. A model with layered soil is created and the reflection at the stratum interface is compared to expectations based on the impedance mismatch.

Frequency Domain Solution

The procedure for solving dynamic problems in the frequency domain is outlined. An analysis is conducted in which the response of a simply supported beam is calculated in the time domain and in the frequency domain. A soil body subjected to a harmonic load is evaluated in the frequency domain as an additional validation of the boundary conditions.

Road Elements

The road is supported by Kelvin supports and interface elements. The analytical solution for the Kelvin foundation is compared to a numerical model with transmitting boundary conditions. A similar model is constructed in which the Kelvin supports are replaced by interface elements. The stiffness matrix for the three-noded Mindlin element is derived and validated using a convergence analysis.

Three-dimensional elements

The system matrices for the 26-noded quadrilateral element are presented. A cantilever beam is constructed and the static response is compared to analytical expectations. A study of the geometrical dissipation of waves is performed. The setup for simulation of the traffic-induced vibration problem is described.

Evaluation of Vibrations

The concept of frequency weighting of vibrations is explained and the procedure for application of one-third octave bands is presented.

Electronic Material

The electronic material can be found in the enclosed DVD at the back of the report. The main part of the material consists of the program codes for the two-dimensional finite-element model. Additional independent programs are included as well, such as programs for evaluation of vibration, calculation in the frequency domain and simulation using the three-dimensional finite-element model. An overview of the main program and some of the independent programs is included in the Program Review.

Articles

A fully coupled finite-element model for prediction of traffic-induced vibration in buildings

Kristian S. Bach Michael Vigsø Morten M. Elmholt
Lars V. Andersen
Department of Civil Engineering, Aalborg University, Aalborg, Denmark

Abstract

In practical engineering, issues regarding vibration caused by traffic or construction work are usually dealt with in a non precautious manner. Vibration monitors are attached to the foundations of sensitive structures and alarms are activated at high accelerations. The method is unsafe due to the chronology of events and the necessary number of monitors may be comprehensive in densely populated areas. In order to estimate the vibrations from traffic, a two-dimensional finite-element model is constructed, containing models of a vehicle, a road, a soil body and a building. The interaction between the vehicle moving with constant velocity and the road beneath can be implemented in two ways: An explicit method where the two systems are treated separately with a time shift and an implicit method where the system matrices are joined and updated for each time step. Relevant assumptions and considerations are discussed and examples are presented with a three-axel bus passing different speed bumps.

1 Introduction

Vibrations from traffic can be generated from vehicles crossing speed bumps or rough pavements. The vibrations propagate in the surrounding soil and cause excitation in structures, and in critical cases the exitations can be uncomfortable for residents or cause damage to structures. Several studies, experimental as well as analytical, have been performed in order to quantify the issue of vibration.

In the article by Watts and Krylov, (1999), field studies of different vehicles crossing speed bumps are compared to analytical predictions in order to develop recommendations for the design and positioning of speed bumps. The article focuses on ground vibrations only, while a study by Hunaidi et al., (2000) includes the propagation in the structure as well. The article presents a field study in which the dynamic pavement loads and vibrations are measured for two transit buses with different characteristics. The experiments revealed that, even though the dynamic pavement loads and the frequency response for loads in the ground were different for the two vehicles, the vibration response in the structure was less significant.

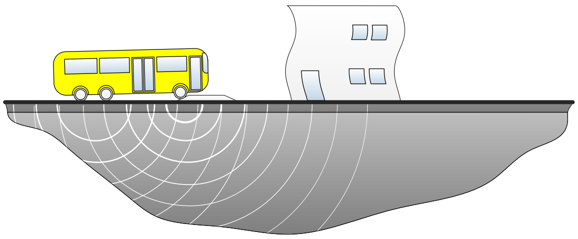

Figure 1: Illustration of problem with traffic-induced vibration.

A pure analytical approach is applied in the article by Mhanna et al., (2011). A four-degrees-of-freedom vehicle runs across different speed bumps whereafter the load response at the surface is applied to a three-dimensional (3D) finite-difference model. A parametric study is conducted, revealing that low vehicle speed, a moderate slope on the speed bump and an elastic suspension system can reduce the vibrations. The model, however, does not include a structure. In the study by Fiala et al., (2006) a numerical model is constructed to simulate the vibrations from a high speed train passing a multistory portal frame office building. Forces from the vehicle are transmitted to the soil which is modelled using a 3D boundary element formulation. The building is modeled separatly by applying deformations at the foundation. The model is used to evaluate the effect of different isolation types.

Except for the field study by Hunaidi et al., (2000), the studies described make use of decoupled systems, in which the vehicle, the soil and the structure are considered separately. However, in the article by Hunaidi et al., (2000), it was demonstrated that the interaction between the soil and the structure had a significant influence for the response. In an article by Henchi et al., (1997) regarding bridge vibrations it is explained how a coupled system in which the bridge and the moving vehicle interact can be constructed. The model revealed that differences between the coupled and the uncoupled system occurred at low vehicle velocities. In the study by Fiala et al., (2006) it is stated that decoupling of soil body and building is an appropriate simplification solely for cases, in which the soil body is significantly stiffer than the building.

The aim of this article is to construct a finite-element

(FE) model in which a moving vehicle, a soil body and a structure are included and interact. Each sub part of the model will be presented in Section 2 and possibilities of variation are discussed. In Section 3 two methods to include the interaction will be explained and implemented with the necessary precautions. The vibrations are generated due to irregularities in the surface profile. Two profile types, speed bumps and cobblestone pavements, are implemented and will be described in Section 4. To demonstrate the use of the model, examples with three different speed bumps are conducted. The setup for the simulations are described in Section 5 and the results are analysed in Section 6. In other words the aim of the article is to model the problem illustrated in Figure 1.

2 The Finite Element Model

The model is programmed in MatLab and consists of one- and two-dimensional finite elements assuming plane strain in the ground and beam bending in the road and building. The problem is dynamic due to the moving vehicle as illustrated in Figure 2. The model is intended for a parametric study and therefore contains a range of variation possibilities. The depth of the soil body, the road and the building is set to one meter out of the plane. In general a significant error is made regarding the wave propagation when the three-dimensional problem is simulated using a two-dimensional model. The influence of the error is discussed in Section 6.

2.1 The Vehicle

The vehicle model is constructed with inspiration from Henchi et al., (1997). Each axel is modelled using two pairs of viscoelastic springs and dashpots representing the mechanics of the tyres and the suspension system, respectiely. The rest of the vehicle is modeled as a rigid rectangular body which can rotate a translate vertically, see Figure 3. The vehicle moves horizontally at a constant speed, i.e. without acceleration.

The number of axels is denoted A and the mass of the system is lumped. All tyres are assumed to have the same properties k_1 and c_1 and the same assumption is made for the suspension system. In the case with a three-axel vehicle, the system matrices are given by:

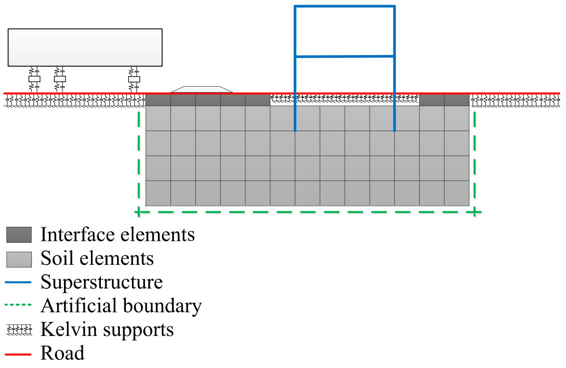

Figure 2: Finite-element model of the problem in Figure 1.

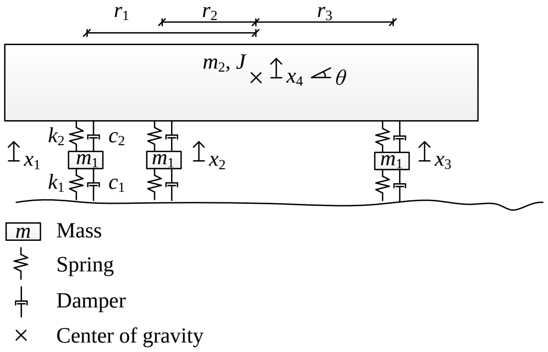

Figure 3: Dynamic model of three-axel vehicle.

$$\mathbf{M}_v = \begin{bmatrix} m_1 & 0 & 0 & 0 & 0 \\ 0 & m_1 & 0 & 0 & 0 \\ 0 & 0 & m_1 & 0 & 0 \\ 0 & 0 & 0 & m_2 & 0 \\ 0 & 0 & 0 & 0 & J \end{bmatrix}, \qquad (1)$$

$$\mathbf{K}_v = \begin{bmatrix} k_1+k_2 & 0 & 0 & -k_2 & k_2 \cdot r_1 \\ 0 & k_1+k_2 & 0 & -k_2 & k_2 \cdot r_2 \\ 0 & 0 & k_1+k_2 & -k_2 & k_2 \cdot r_3 \\ -k_2 & -k_2 & -k_2 & 3 \cdot k_2 & \sum_{i=1}^{3} -k_2 \cdot r_i \\ k_2 \cdot r_1 & k_2 \cdot r_2 & k_2 \cdot r_3 & \sum_{i=1}^{3} -k_2 \cdot r_i & \sum_{i=1}^{3} r_i \cdot k_2 \cdot r_i \end{bmatrix}. \qquad (2)$$

The damping matrix $\mathbf{C}_v$ is constructed similar to the stiffness matrix. Generalization to more complex vehicles, e.g. with more axels, is straightforward. The parameters in the system matrices can be determined experimentally for the individual vehicle. If no information is available concerning the stiffness and damping coefficients, the parameters can be calibrated from the following assumptions:

1. The value of k_1 is five times higher than the value of k_2.
2. The damping matrix is stiffness proportional.
3. The vehicle has a damping ratio of 0.40 in the first eigen mode.
4. The driver will experience an acceleration of 0.65 g when the vehicle crosses a speed bump at the nominal speed.

The damping ratio for a vehicle is typically in the range of 0.20 - 0.80 according to (Dixon, 2007). A high damping ratio improves the handling, while a low damping ratio makes the ride more comfortable. It is assumed that the lower edge of the tyre is connected to the surface at any time. Hence, the external forces on the vehicle can be calculated from:

$$\mathbf{M}_v\ddot{\mathbf{x}} + \mathbf{C}_v\dot{\mathbf{x}} + \mathbf{K}_v\mathbf{x} = \mathbf{C}_v\mathbf{U}\dot{\mathbf{y}}(t) + \mathbf{K}_v\mathbf{U}\mathbf{y}(t), \qquad (3)$$

where $\mathbf{y}(t)$ and $\dot{\mathbf{y}}(t)$ denote the surface elevation and the rate of change in surface elevation at the three axels, respectively. $\mathbf{U}$ expresses the quasi-static response

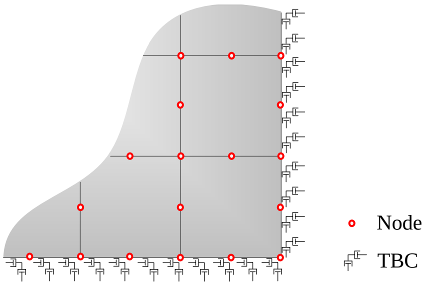

Figure 4: Eight noded quadrilateral elements and TBC.

to movement of a support and will be a five times three matrix in the case with five degrees of freedom and three movable supports.

If the surface is considered to be fixed, the vehicle-road interaction forces (surface forces) can be calculated from the relative compression and rate of compression of the tyres:

$$f_i = k_1\left(x_i - y_i\right) + c_1\left(\dot{x}_i - \dot{y}_i\right), \quad i = 1,2,..,A. \tag{4}$$

In case of a movable surface, the relative movement of the surface is included in the equation, see Section 3.

2.2 The Soil Body

The vibrations generated by the vehicle will propagate in the soil and into the structure. The soil is modelled using rectangular eight-noded quadrilateral elements as illustrated in Figure 4. Transmitting boundary conditions (TBC) are applied at the submerged boundaries to simulate the properties of an infinite half space. The procedure described by Lysmer and Kuhlmeyer, (1969) is used to implement the boundaries and it is assumed that waves propagate perpendicular to the boundaries. Hereby, the accuracy of the boundaries depends of the position of the vehicle. However, it is found that the reflection is generally insignificant.

The effect of the boundaries are illustrated in Figure 5. A harmonic vertical line load is applied at the center of the surface of a rectangular soil body. The stationary response is calculated from the frequency domain solution with and without transmitting boundary conditions.

2.3 The Road

In order to simulate the effect of pavement and subgrade, a beam layer is constructed supported by springs and dashpots. As illustrated in Figure 2, soil elements are included at the center of the model only, while the road is extended in both directions. The length of the road is increased to ensure that initiation effects in the vehicle are removed before the vehicle reaches the building. By reducing the soil body in the model, the computational cost is reduced and it is estimated that the vibrations generated outside the modelled soil body are negligible.

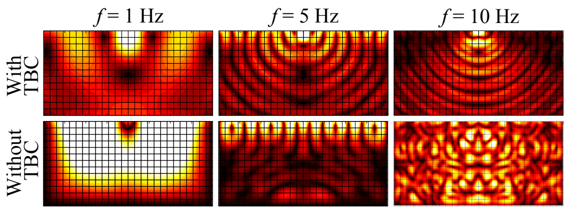

Figure 5: Stationary response at different load frequencies.

The subgrade outside the soil body is supported by a Kelvin foundation, cf. Andersen, (2006). The properties of the Kelvin foundation are calibrated to approximate the properties of the soil body. This is done by adding stiffness and mass to the road corresponding to a soil column with a height of $h/2$, where h is the height of the soil body. The simplification is inaccurate but in general the properties of the Kelvin foundation are insignificant in connection to the vibration in the building. At the soil body the forces generated by the vehicle are transmitted to the soil through interface elements. The interface elements each contain six nodes with vertical degrees of freedom only. As illustrated in Figure 6, linear and quadratic shape functions are used in the vertical and horizontal directions respectively. An issue arises as the interface elements in contrast to the Kelvin foundation does not contribute to the rotational stiffness. The problem, however, can be diminished by refining the mesh. A spurious mode may occur when nonconforming beam elements of cubic order are connected to continuum elements with quadratic shape functions as illustrated in Figure 7. The spurious mode can be prevented by applying Mindlin beam elements with quadratic shape functions cf. Cook et al., (2002). Mindlin beams are derived by separating the stiffness matrix in a contribution from bending and a contribution from shear:

$$U_s = \int \int_0^L \frac{1}{2} G \gamma_{zx}^2 dx\, dA, \tag{5}$$

$$U_b = \int \int_0^L \frac{1}{2} E \varepsilon_x^2 dx\, dA. \tag{6}$$

U denotes the element strain energy while E and G denote the elasticity and shear modulus respectively. The mass matrix is derived in the same manner as for the Bernoulli beam elements.

At both edges of the road, transmitting boundaries are applied according to Andersen, (2006). Section forces

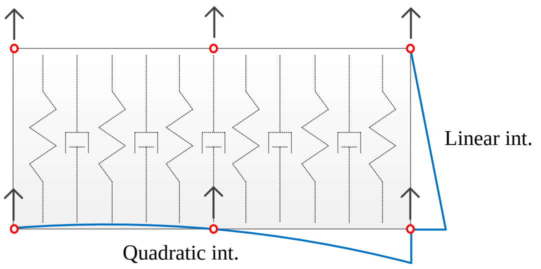

Figure 6: Six noded interface element.

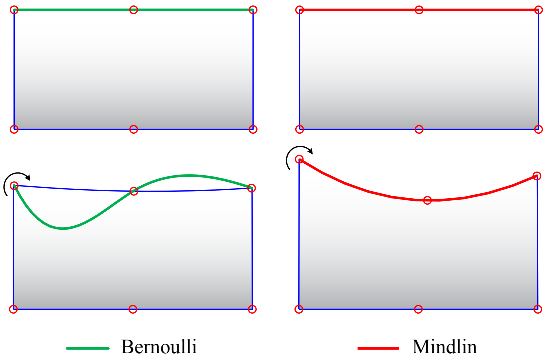

Figure 7: Spurious mode occurring with Bernoulli beam elements (left) but prevented with Mindlin beam elements (right).

are applied to represent the external beams. The boundary section forces are defined by:

$$\begin{bmatrix} Q_b(t) \\ M_b(t) \end{bmatrix} = \mathbf{K}_b \begin{bmatrix} u_b(t) \\ \theta_b(t) \end{bmatrix} + \mathbf{C}_b \begin{bmatrix} \dot{u}_b(t) \\ \dot{\theta}_b(t) \end{bmatrix}. \tag{7}$$

Here, u_b and θ_b represent the displacement and rotation at the boundaries, respectively. The boundary stiffness and damping matrices are calibrated to a circular load frequency ω_1. Partial reflection will occur at circular frequencies differing from ω_1.

2.4 The Building

The building is constructed using Bernoulli beam elements and in consideration of a future parametric study, a number of variation possibilities are incorporated. The geometry, the material properties of different sections and the structural system can be adjusted. Due to the relatively high stiffness of the foundation compared to the soil it has been found that spurious modes are unlikely to occur in the connection between soil body and building.

3 Model Interaction

The simplest way to implement a moving load is to consider the vehicle and the soil separately by running the vehicle across a fixed surface and afterwards apply the reaction forces to the road. This method, however, does not account for movements in the road which may influence the response of the vehicle. The interaction can be implemented by an explicit or implicit procedure.

3.1 Explicit Time Scheme

In the explicit scheme the vehicle and the road models are considered separately but the original surface is updated in every time step. The procedure is described in the following six steps:

1. The original surface profile is used in the first time step.
2. The equation of motion is solved for the vehicle model.
3. The reaction forces on the road are calculated.
4. The equation of motion is solved for the stationary part of the model, i.e. the road, the soil body and the building.
5. The displacement of the road is added to the original surface profile.
6. Steps 2 - 5 are repeated for the next time steps using the updated surface profile.

The procedure is relatively simple to implement in a time integration scheme, and shape functions can be used to interpolate nodal reaction forces or internal displacements for time steps, in which the axels are positioned between element nodes. The main disadvantage of the procedure is that a time shift occurs as the response of the vehicle is calculated before the displacement of the road is known, which in some cases causes instability in the calculations. Furthermore the evaluation of shape functions in every time step can increase the computation time significantly.

3.2 Implicit Time Scheme

In the implicit scheme the vehicle and the road are considered as a connected system whereby the two system matrices are joined. The unification of the system matrices is straightforward for the mass matrix:

$$\mathbf{M} = \begin{bmatrix} \mathbf{M}_s & \mathbf{0} \\ \mathbf{0} & \mathbf{M}_v \end{bmatrix}. \tag{8}$$

The subscript s refers to the stationary part of the model. The interaction between the systems is represented in the stiffness matrix which can be separated into two parts in which the second array contains the interaction:

$$\mathbf{K} = \begin{bmatrix} \mathbf{K}_s & \mathbf{0} \\ \mathbf{0} & \mathbf{K}_v \end{bmatrix} + \begin{bmatrix} \mathbf{N}^T k_1 \mathbf{N} & -\mathbf{N}^T k_1 \\ -\mathbf{N} k_1 & \mathbf{0} \end{bmatrix}, \tag{9}$$

where, $\mathbf{N}$ is the shape function for the road elements. $\mathbf{N}$ is evaluated for the position of every axel in the current time step. The damping matrix can be assembled in a similar manner. As in the explicit scheme shape functions are used to calculate the contribution to the stiffness matrix when an axel is positioned between element nodes. The system matrices change as the vehicle crosses the surface and need to be updated by evaluating $\mathbf{N}$ in every time step. The external forces in the system are determined from the surface roughness:

$$\mathbf{f}(t) = \begin{bmatrix} -\mathbf{N}^T \left(k_1 \cdot \mathbf{y}(t) + c_1 \cdot \dot{\mathbf{y}}(t)\right) \\ \mathbf{K}_v \mathbf{U} \cdot \mathbf{y}(t) + \mathbf{C}_v \mathbf{U} \cdot \dot{\mathbf{y}}(t) \end{bmatrix}. \tag{10}$$

The implicit scheme operates with a single system matrix whereby the issue regarding the time shift is eliminated and the method has generally shown to be more stable than the explicit scheme. For models consisting of a limited amount of degrees of freedom, e.g. a vehicle on a bridge, the computational time is significantly reduced compared to the explicit time scheme. However, when applying a soil body, the computation time increases substantially. The reason is that inversion of the system matrices is used in the Newmark time integration algorithm and has to be repeated in every time step as the system matrices change. This operation has a high computational cost for large matrices.

In general the implicit time integration scheme is assessed to be more reliable and elegant compared to the explicit scheme.

4 Surface Profile

Vibrations are generated as the vehicle crosses an uneven surface. The unevenness may be a result of speed bumps, cobblestones or simply small irregularities in the road due to lack of maintenance and cracks, as described by Nielsen and Kirkegaard, (1999). In articles such as (Kønigsfeldt, 2005), (Sønderup, 2008) and (Grønvald, 2013) it is described how vibrations due to the mentioned surface profiles have caused discomfort and sleep disturbances for residents. The surface profiles for speed bumps and cobblestone pavement are included in the program.

4.1 Speed Bumps

The implemented speed bumps are designed according to Danish regulations. Proclamations are given in (Retsinformation, 2002) while recommendations for approved speed bumps can be found in (Vejdirektoratet, 2009). The circle, the sinus and the trapeze bump are considered to be the most frequently used and will be included. The design of the speed bump is modified to the desired speed limit and in Figure 8 the three bump types are illustrated for a speed limit of 40 km/h. Details on the geometry of the speed bumps can be found in Table 1. The curve of the sinus bump corresponds to half a period.

If the contact surface between the wheel and the road is assumed to be a point, the vehicle will be subjected to unrealistically high accelerations at the beginning of the bump, due to the high gradient. In reality the contact surface is likely between 10 and 20 cm depending on the size of the tyre and the level of inflation. In order to account for this effect, the surface profile is smoothened using a moving average filter. The effect of a 15 cm filter is illustrated in Figure 9 for the circle bump.

Table 1: Geometrical values of the speed bumps.

Bump type	Circle	Sinus	Trapeze
Height	0.1 m	0.1 m	0.1 m
Width	6.5 m	6.5 m	7.4 m
Slope	-	-	5.9 %

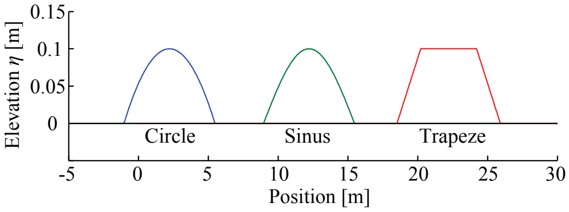

Figure 8: Different bump types implemented in the model.

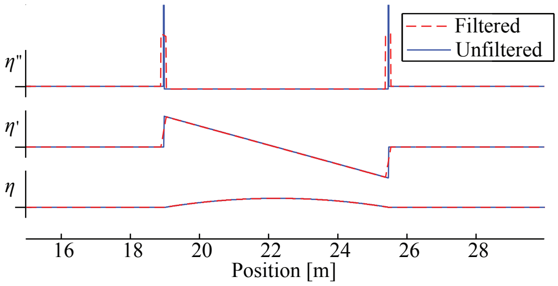

Figure 9: Effect of contact surface for circle bump.

As illustrated, the effect of the contact surface is difficult to identify when considering the elevation alone while the difference is significant when evaluating the derivatives of the elevation.

4.2 Cobblestone Pavement

The surface profile of a cobblestone pavement has a significant variation depending on the location and the traffic direction. Each brick is unique, and based on field studies it is assessed that a realistic estimate of the profile can be determined by considering the length and height of each brick and the gap between as normally distributed stochastic variables. The surface of a cobblestone is assumed to be circular. The presumed stochastic parameters are given in Figure 10. A lower limit has been implemented for the cobblestone height to prevent negative values.

A realization of a cobblestone pavement is illustrated in Figure 11 along with the result from the average filter procedure. It should be noticed that the filtered surface profile has been displaced 10 cm for visual purposes. Alternatively the contact between road and tyre can be modelled more accurately using methods described by Pacejka, (2006).

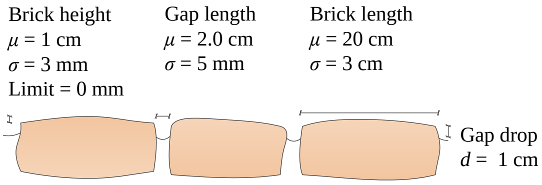

Figure 10: Stochastic description of cobblestone pavement.

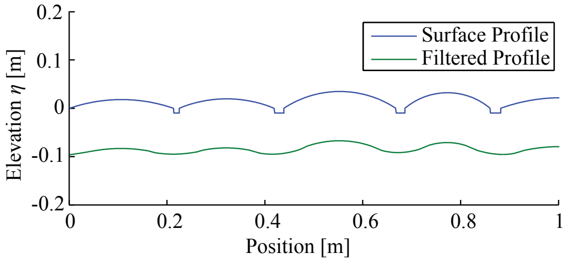

Figure 11: Realization of cobblestone pavement with and without filtering.

Table 2: Vehicle properties based on Scania A/S and calibration.

Parameter	Symbol	Unit	Value
Vehicle mass	m_2	ton	17
Axel mass	m_1	ton	1.0
Tyre stiffness	k_1	kN/m	3000
Tyre damping	c_1	kN s/m	727
Suspension stiffness	k_2	kN/m	600
Suspension damping	c_2	kN s/m	145
Contact surface	w	m	0.10

5 Simulation Setup

In order to evaluate the consequences of the different speed bumps with respect to vibrations, simulations are conducted for each of the three surface profiles illustrated in Figure 8. A reference case is set up to substantiate a comparision. The geometry of the reference case is illustrated in Figure 12.

Based on product specifications for a three axel bus provided by Scania A/S, the properties listed in Table 2 are assumed for the vehicle.

The geometry of the bus is illustrated in Figure 13. The position of the driver is essential when evaluating the vertical accelerations used to assess the usability of a speed bump.

The values of stiffness and dampers are calibrated according to the procedure in Section 2. The damping ratio of the vehicle is set to 1.00. The parameters can be verified by performing a simulation where the bus crosses a sinusoidal speed bump with a velocity of 25 km/h. The acceleration of the driver is given in Figure 14. Minor time shifts are added to the acceleration series for visual purposes.

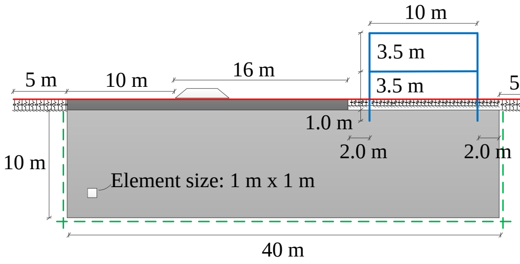

Figure 12: Geometry of model used for simulation.

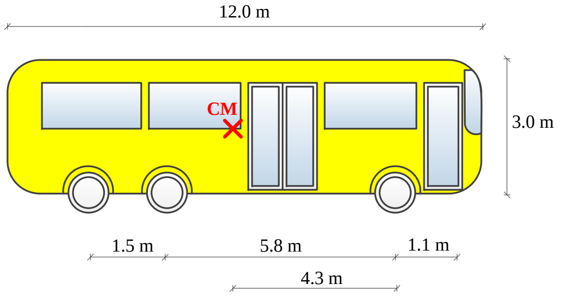

Figure 13: Geometry of vehicle used for simulation.

As illustrated in the figure it is not possible to calibrate the vehicle to satisfy the regulations in (Retsinformation, 2002) for all three bump types. The sinusodial shaped speed bump has a more gentle curve if it is designed according to Vejdirektoratet, (2009), and will always induce smaller accelerations. The selected properties are assesed to give the best fit. Furthermore it should be noticed that large negative vibrations are generated when the trapeze bump is used due to discontinuities in the slope.

Soil parameters such as density and Poisson's ratio are obtained from recommendations by Ovesen et al., (2009) and Zhu, (2012). A linear visco-elastic soil model is employed which is an appropriate simplification in case of small strains. A Poisson's ratio of $\nu = 0.3$ is assumed for unsaturated/draned conditions, while a ratio of $\nu = 0.495$ is used for saturated/undrained conditions. The dynamic stiffness of soil is considerably larger compared to static loading conditions and the stiffness of each material is therefore calibrated based on wave propagation velocities

$$c_p = \sqrt{\frac{\lambda + 2\mu}{\rho}}, \qquad c_s = \sqrt{\frac{\mu}{\rho}}, \tag{11}$$

$$\lambda = \frac{\nu E}{(1+\nu)(1-2\nu)}, \qquad \mu = \frac{E}{2(1+\nu)}, \tag{12}$$

where, λ and μ are Lamé constants. Typical propagation velocities based on the soil type can be estimated from (KTH and Engineering, 1979). Material damping in soil is described by Kramer, (2007) and for relatively

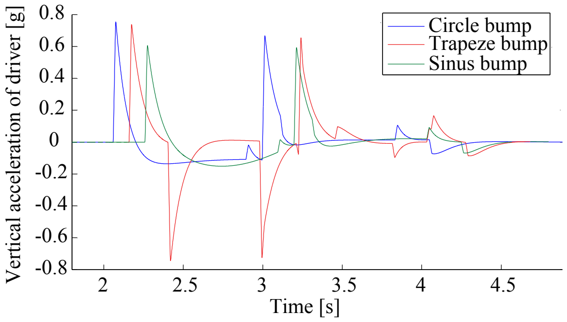

Figure 14: Acceleration of driver for different speed bumps.

Table 3: Soil and interface properties.

Parameter	Symbol	Unit	Value
Material	-	-	Silty clay
Density	ρ	kg/m^3	1600
Poissons ratio	ν	-	0.3
Young's modulus	E	MPa	300

Table 4: Road properties.

Parameter	Symbol	Unit	Value
Material	-	-	Asphalt
Height	h_{road}	m	0.30
Density	ρ	kg/m^3	2400
Young's modulus	E	GPa	5.0
TBC freq.	ω_1	rad/s	6.28

small shear strains the damping ratio will be in the range of 0 – 5 %. A damping ratio of 0 will be used in the simulations. The soil properties are given in Table 3.

The road is modelled as a beam layer of asphalt and the properties are based on (Tarefder et al., 2010). The Kelvin supports representing the soil volume at the edges of the model are calibrated to approximate the properties of the soil body. The transmitting boundaries applied to the road can be calibrated to a single frequency only, though traffic loads are generally described in a broad range of frequencies. In lack of better estimates a frequency of 1 Hz is selected and simulations have shown that the reflection from the boundary is insignificant. The road properties are given in Table 4.

The structural system and the material properties of the building have a substantial influence for the dynamic respons. However, in this case the scope is to evaluate whether or not a change in the surface profiles changes the overall response, whereby the building is of lesser importance. The properties of the building are given in Table 5. The building is assumed to be stiffness proportionally damped with a damping ratio of $\xi_1 = 1\%$ for the first eigen mode. Linear viscous damping is employed.

6 Simulation Results

Table 5: Properties of the building.

Parameter	Symbol	Unit	Value
Material	-	-	Concrete
Beam height			
Superstructure	h_{super}	m	0.40
Foundation	h_{found}	m	0.40
Density	ρ	kg/m^3	2500
Young's modulus	E	GPa	50

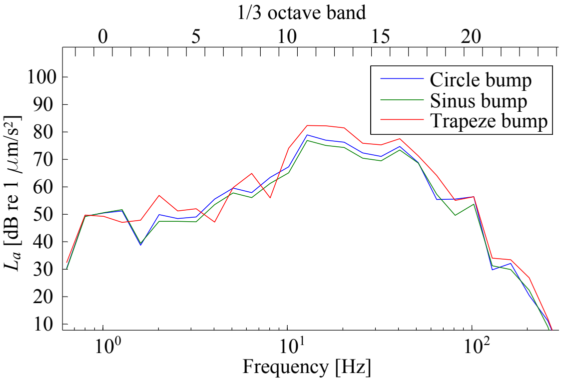

Figure 15: Frequency response for 1/3 octave bands.

Simulations are conducted for each of the speed bumps. In order to quantify the vibrations, a point at the floor division 2.5 metres from the left wall is considered. The object is to evaluate the human exposure which is done according to the procedure described in (ISO 2631, 1997). The vibrations generated from traffic are mainly occasional shocks and in such case it is recommended to use the running root-mean-square (r.m.s.) method:

$$a_w(t_0) = \left\{ \frac{1}{\tau} \int_{t_0-\tau}^{t_0} [a_w(t)]^2 \, dt \right\}^{\frac{1}{2}} , \tag{13}$$

where $a_w(t_0)$ is the instantaneous frequency-weighted acceleration for the observation time t_0, and τ is the integration time for running averaging and is set to one second. The frequency-weighting is performed based on one-third octave bands. The weighting functions and a guide for principal weightings are stated in (ISO 2631, 1997) as well.

The frequency response for the vertical direction in the observation point is illustrated for one-third octave bands in Figure 15. The response is unweighted and the entire time serie is considered. In general the different speed bumps induce accelerations at the same frequency bands though the amplitude is higher for the trapeze bump. According to Miljøstyrelsen, (1997) the limit level for noticeable vibrations is 71 – 72 dB whereby vibrations in the 10th – 17th one third octave bands may be noticed.

The running r.m.s. method is conducted for both vertical and horizontal direction and the maximum transient vibration value (MTVV) is determined from:

$$\text{MTVV} = \max\left(a_v(t)\right) \quad t \in [\tau; T], \tag{14}$$

$$a_v(t) = \sqrt{k_x^2\, a_{wx}^2(t) + k_y^2\, a_{wy}^2(t)}, \tag{15}$$

where k_x and k_y are multiplication factors stated in (ISO 2631, 1997). The multiplication factors depend on the perception type (health, comfort or motion sickness) and are often higher for cross-spinal vibrations. The maximum transient vibration value for each bump is stated in Table 6.

As indicated in Figure 15 the trapeze bump induces larger vibrations in the building. The MTVV for the

Table 6: Maximum transient vibration value for simulations.

Bump type	Sinus	Circle	Trapeze
MTVV [m/s^2]	0.09	0.11	0.20

trapeze bump is approximately twice as high compared to the circle bump even though the acceleration of the driver, and hereby the effectivity of the bump, is almost the same. The sinus bump and the circle bump induce approximately the same acceleration but it should be noticed that the sinus bump causes smaller vibrations for the driver, as illustrated in Figure 14. Drivers may therefore tend to cross the sinus bump at higher velocities whereby the vibration level will increase.

The perception of vibration is difficult to assess as the perception depends on the expectations of the resident. Guidelines for comfort levels are suggested in (ISO 2631, 1997) in which it is stated that vibration levels less than 0.325 m/s^2 are usually not experienced as uncomfortable. However, two assumptions have to be considered when evaluating the magnitude of the vibration. First of all, the speed bumps in the simulations are located around 10 – 11 metres from the building, and real-life situations may exist for which the distance is significantly shorter. Secondly the geometrical damping is underestimated when the problem is simplified to a two-dimensional case. The deviations between two- and three-dimensional simulations are studied by Vigsø et al., (2013). Conclusively it can be summarized that the model is applicable for comparision of different scenarios while the actual magnitude of vibration should be considered with some skepsis.

7 Conclusion

The construction of a two-dimensional finite element model to evaluate vibrations generated from traffic has been presented in the article. The four sub parts of the model (a vehicle model, a road, a soil body and a building) have been presented, and relevant assumptions regarding boundary conditions, element types etc. have been discussed in Section 2. Two solution methods for implementing the interaction between the stationary part of the model and the moving vehicle have been proposed in Section 3. It has been found that the implicit method with continuous updating of the system matrices is more reliable compared to the explicit method with a time shift. Deterministic surface profiles have been set up for three different speed bumps and stochastic profiles for cobblestone pavements have been implemented in Section 4. Furthermore the effect of the tyre contact surface is described.

The model has been used to analyse the vibrations generated at the floor division in the building from a three axel bus crossing different speed bumps. The calibration of parameters such as the vehicle system matrices, the soil stiffness and the dynamic properties of the building are explained in Section 5 and a reference case is set up. The simulations are conducted in Section 6 and it has been found that the largest vibrations are generated from the trapeze formed speed bump. The effectivity of a speed bump depends on the acceleration experienced by the driver and in this regard the trapeze and the circle bump caused approximately the same acceleration while the sinus bump caused smaller accelerations. Drivers may therefore tend to cross the sinus bump at higher velocities. All together the circle bump is assesed to be the most beneficial bump type. None of the three speed bumps induced vibrations large enough to cause discomfort for residents in the building but for speed bumps located closer to the building vibrations will be higher and may cause discomfort.

References

Andersen, 2006. Lars V. Andersen. *Linear Elastodynamic Analysis*. 2006.

Cook, Malkus, Plesha, and Witt, 2002. Robert D. Cook, David S. Malkus, Michael E. Plesha, and Robert J. Witt. *Concepts and Applications of Finite Element Analysis*. John Wiley and Sons, INC, fourth edition edition, 2002.

Dixon, 2007. John C. Dixon. *The Shock Absorber Handbook*. Wiley, 2007.

Fiala, Degrande, and Augusztinovicz, 2006. P. Fiala, G. Degrande, and F. Augusztinovicz. *Numerical modelling of ground-borne noise and vibration in buildings due to surface rail traffic*. 2006.

Grønvald, 2013. Henrik Grønvald. *Tung trafik ødelægger gamle huse*. 2013.

Henchi, Fafard, Talbot, and Dhatt, 1997. K. Henchi, M. Fafard, M. Talbot, and G. Dhatt. *An efficient algorithm for dynamic analysis of bridges under moving vehicles using a coupled modal and physical components approach*. 1997.

Hunaidi, Guan, and Nicks, 2000. O. Hunaidi, W. Guan, and J. Nicks. *Building vibrations and dynamic pavement loads induced by transit buses*. 2000.

ISO 2631, 1997. International Standard ISO 2631. *Mechanical vibration and shock - Evaluation of human exposure to whole-body vibration*, 1997.

Kønigsfeldt, 2005. Steen Kønigsfeldt. *Rystelser fra trafikken*. 2005.

Kramer, 2007. Steven L. Kramer. *Geotechnical Earthquake Engeneering*. Pearson, 2007.

KTH and Engineering, 1979. Department of Civil KTH and Architectural Engineering. *Soil and rock mechanics*. 1979.

Lysmer and Kuhlmeyer, **1969**. J. Lysmer and R.L. Kuhlmeyer. *Finite Dynamic Model for Infinite Media*. 1969.

Mhanna, Sadek, and Shahrour, **2011**. Mohannad Mhanna, Marwan Sadek, and Isam Shahrour. *Numerical modeling of traffic-induced ground vibration*. 2011.

Miljøstyrelsen, **1997**. Miljøstyrelsen. *Lavfrekvent støj, infralyd og vibrationer i eksternt miljø*. Miljø- og Energiministeriet, 1997.

Nielsen and Kirkegaard, **1999**. Søren R. K. Nielsen and P. H. Kirkegaard. *Influence of surface irregularities on the dynamic respons of minor highway bridges*. 1999.

Ovesen, Fuglsang, and Bagge, **2009**. Niels Krebs Ovesen, Leif Fuglsang, and Gunnar Bagge. *Lærebog i Geoteknik*. 978-87-502-0961-4. Polyteknisk Forlag, 2009.

Pacejka, **2006**. Hans B. Pacejka. *Tyre and Vehicle Dynamics*. Butterworth-Heinermann, 2006.

Retsinformation, **2002**. Retsinformation. *Bekendtgørelse om vejbump og andre hastighedsdæmpende foranstaltninger*, 2002.

Sønderup, **2008**. Anders Sønderup. *Asfalt på Boulevarden*. 2008.

Tarefder, Zaman, and Uddin, **2010**. Rafiqul A. Tarefder, Arif M. Zaman, and Waheed Uddin. *Determining Hardness and Elastic Modulus of Asphalt by Nanoindentation*. 2010.

Vejdirektoratet, **2009**. Vejdirektoratet. *Byens trafikarealer - Hæfte 7. Fartdæmpere*, 2009.

Vigsø, Elmholt, and Bach, **2013**. M. Vigsø, M. Elmholt, and K. S. Bach. *Considerations concerning finite-element modelling of traffic-induced vibration*. 2013.

Watts and Krylov, **1999**. G.R. Watts and V.V. Krylov. *Ground-borne vibration generated by vehicles crossing road humps and speed control cushions*. 1999.

Zhu, **2012**. Tieyuan Zhu. *Some Useful Numbers on the Engineering Properties of Materials*. 2012.

Parameter studies of traffic-induced vibration using a finite-element model

Morten M. Elmholt Kristian S. Bach Michael Vigsø
Lars V. Andersen
Department of Civil Engineering, Aalborg University, Aalborg, Denmark

Abstract

Noise and vibration caused by heavy vehicles in populated areas have in several cases proven to cause discomfort for nearby residents. Airborne noise may be transmitted directly via window and door openings in the facade, or in the form of ground and structure borne vibrations as discussed in this paper. More specifically a parameter study is conducted using a two dimensional finite-element model containing a vehicle, a road, a soil body and a building. The scope of the study is to examine how parameters such as surface composition, vehicle properties and soil stratigraphic influence the generation of vibrations. A brief description of the finite-element model is included and a reference case is set up in order to relate the results of the parameter study.

1 Introduction

Traffic-induced vibration can be generated when heavy vehicles cross surface irregularities. Irregularities such as speed bumps, rough pavements or manhole covers cause vertical accelerations of the vehicle whereby reaction forces are applied to the surface. The induced energy propagates through the underlying soil waves into nearby buildings. Several cases can be mentioned in which vibrations have caused discomfort for residents in Danish cities such as Aalborg (Sønderup, 2008), Aarhus (Grønvald, 2013) and Copenhagen (Kønigsfeldt, 2005).

In practical engineering the issue of vibration is usually dealt with by monitoring acceleration levels on buildings in risk of impact. The method can be expensive if several gauges are required and it does not ensure that vibration levels will be acceptable. A useful supplement to the method would therefore be to construct a scientific model to simulate and predict the generated vibrations prior to the exposure. Several models have been suggested as described by e.g. Mhanna et al., (2011) and Lombaert et al., (2000).

Common for these articles is that the sub parts of the model are treated separately. Hence, the vibrations are calculated without considering the interaction between vehicle, soil body and building. However, field studies conducted in (Hunaidi et al., 2000) have indicated that especially the interaction between soil and building may be important.

The aim of this article is to conduct a parameter study using a finite-element model which contains all three sub parts and accounts for the interaction. An illustration of the problem can be found in Figure 1.

A detailed description of the model is given by Bach et al., (2013), while the main structure including the selection of a reference case is summarized in Section 2.

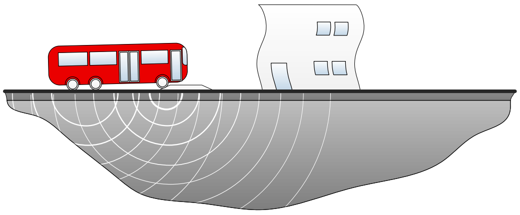

Figure 1: Illustration of problem with traffic-induced vibration.

The vibrations occurring in the building are evaluated according to the procedure in (ISO 2631, 1997) with respect to comfort, and the main principles are presented in Section 3. In Section 4 a parameter study is performed in which the vehicle is considered separate and the influence of vehicle velocity and damping ratio is investigated. The soil body and the building are included in Section 5 and different critical combinations are simulated and compared. In Section 6 the influence of the soil is analysed and a stratum is introduced to generate reflection. Each simulation is compared to the reference case in order to give a quantitative estimate of the influence of the given parameter.

2 The Reference Case

The finite-element model used in the simulations is illustrated in Figure 2 and can be devided into sub parts. The external forces are generated by a vehicle model with four or more degrees of freedom depending on the number of axels. The vehicle travels with constant velocity across an irregular surface profile, e.g. a speed bump or a cobblestone pavement. The geometry of the speed bump will be deterministic while a stochastic description is implemented for the cobblestones. The vehicle model used in the following study is illustrated in Figure 3.

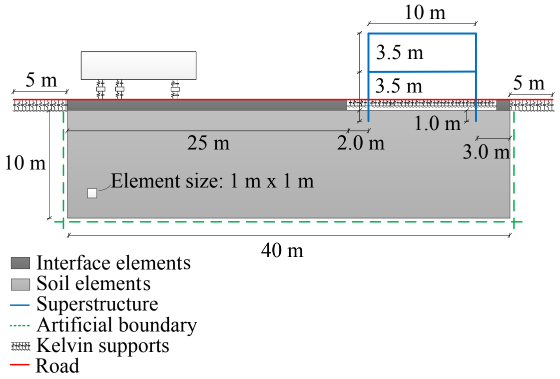

Figure 2: FE model of the problem in Figure 1.

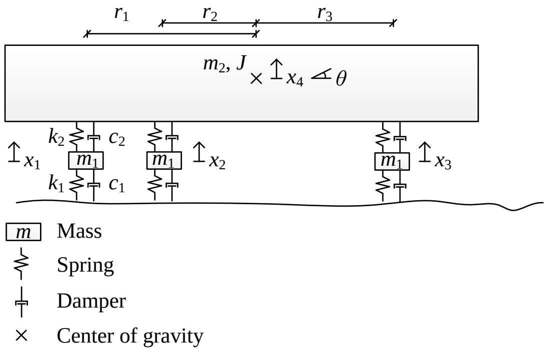

Figure 3: Dynamic model of three-axel vehicle.

The vehicle is supported by Mindlin beam elements cf. Cook et al., (2002) which are connected to the soil body through interface elements. The road is extended at both sides of the soil body, which is done in order to diminish initialization effects in the vehicle. Outside the soil body the road elements are supported by a Kelvin foundation. In reality the vehicle will pass the building with some distance in between which in this case is assumed to be 2 metres. In order to account for this effect the road elements beneath the building and two metres from it are supported by Kelvin foundations as well. When the vehicle is located on the Kelvin foundations, the surface loads will not be transmitted directly to the soil body. The Kelvin foundation is calibrated to approximate the properties of the soil body. This is done by adding stiffness and mass to the road corresponding to a soil column with half the height of the soil body in Figure 2. In (Bach et al., 2013) it is stated that the inaccuracy of the simplification is insignificant in connection to the vibration in the building.

The soil body is modelled using quadrilateral eight-noded continuum elements and transmitting boundary conditions are applied at the submerged boundaries to simulate the infinite half space, cf. Lysmer and Kuhlmeyer, (1969). The building consist of Bernoulli beam elements and all connections are rigid.

In a paper by Bach et al., (2013) a simulation is conducted in which a bus crosses a speed bump. The same setup will be used as a reference case in the parameter study. The amount of variables is comprehensive but some of the most descriptive parameters are presented in Table 1.

Table 1: Selected parameters for reference case.

Parameter	Symbol	Unit	Value
Vehicle			
Length	l_{veh}	m	12
Height	h_{veh}	m	3
Total mass	M_{veh}	t	20
Number of axels	A	-	3
Tyre stiffness	k_1	kN/m	3000
Suspension stiffness	k_2	kN/m	600
Eigenfreq. 1, 2	f_{12}	Hz	≈ 1.4
Eigenfreq. 3, 4, 5	f_{345}	Hz	≈ 9.6
Road			
Height	h_{road}	m	0.30
Density	ρ	kg/m^3	2400
Young's modulus	E	GPa	5.0
Soil and interface			
Density	ρ	kg/m^3	1800
Poisson's ratio	ν	-	0.3
Young's modulus	E	MPa	300
Material damping	none	-	-
Building			
Height	h_{build}	m	7.5
Width	w_{build}	m	10.0
Beam height	h_{beam}	m	0.4
Density	ρ	kg/m^3	2500
Young's modulus	E	GPa	50
Eigenfreq.			
Mode 2	f_{b2}	Hz	13.9
Mode 4	f_{b4}	Hz	16.5
Mode 6	f_{b6}	Hz	39.3
Damping ratio	ξ_1	-	0.01

Only two eigenfrequencies are stated for the five-degree-of-freedom vehicle as eigenfrequency 1 and 2 and eigenfrequency 3, 4 and 5 are coinciding. Mode 1 and 2 relate to motion of the vehicle chassis while mode 3 to 5 relate to motion of the individual axels, see Figure 4. The eigenfrequencies of the building are determined using the complete system matrices including both the building and the soil. As described by Vigsø et al., (2013), considerable deviations may occur if the system matrices of the building are used separately. Several eigenfrequencies can be estimated for the building and three have been selected for the parameter study in

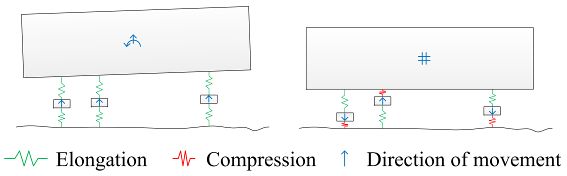

Figure 4: First and third eigenmode of the three axel vehicle.

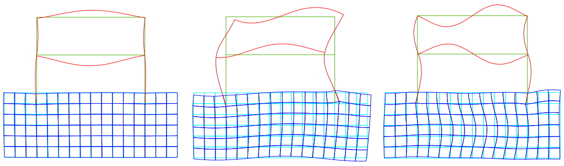

Figure 5: Eigenmodes 2, 4 and 6 of the building selected for parameter study.

Section 5, see Figure 5.

One exception is made compared to the setup described by Bach et al., (2013) regarding the damping properties of the vehicle. Simulations have shown that the assumption of stiffness proportional damping is unsuitable when surface irregularities in the form of cobblestone pavement is introduced. Stiffness proportional damping induces damping in the tyre which causes extensive forces when the surface elevation changes rapidly. According to Kim et al., (2006) the damping ratio of a vehicle tyre is in the range of 0.01 - 0.09. In this case a simplification is made assuming that the damping constant of the tyres is $c_1 = 0$. The damping constant of the suspension system, c_2, can then be calibrated to a given damping ratio of the first eigenmode ξ_1 using modal decoupling:

$$\Phi_1^T \mathbf{C} \Phi_1 = 2\xi_1 \omega_1 \Phi_1^T \mathbf{M} \Phi_1, \tag{1}$$

where Φ_1 and ω_1 are the eigenvector and the angular eigenfrequency for the first mode, respectively. In Table 2 corresponding values of c_2 and ξ_1 are given.

3 Evaluation of Vibrations

The vibration generated from the simulations in Sections 5 and 6 are evaluated according to the procedure in (ISO 2631, 1997). A reference point located at the floor division 2.5 meters from the left wall will be used for comparison. Eigenvibrations of the structure will be visible at the reference point according to the mode-shapes. Traffic-induced vibration occurs occasionally and the running r.m.s. method is used to determine the instantaneous frequency-weighted acceleration:

$$a_w(t_0) = \left\{ \frac{1}{\tau} \int_{t_0-\tau}^{t_0} \left[a_w(t)\right]^2 dt \right\}^{\frac{1}{2}}, \tag{2}$$

where t_0 is the observation time and τ is the integration time set to one second as recommended in (ISO 2631, 1997). The frequency-weighting is performed for one third octave bands using the weight functions illustrated in Figure 6.

Table 2: Corresponding values of ξ_1 and c_2 for $c_1 = 0$.

ξ_1	0.01	0.10	1.00
c_2	1.76e3 Ns	1.76e4 Ns	1.76e5 Ns

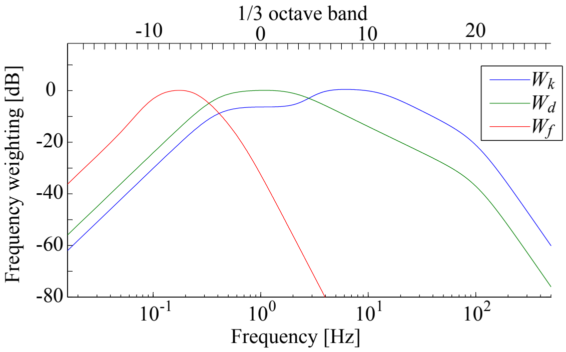

Figure 6: Weight-functions for evaluation of vibrations.

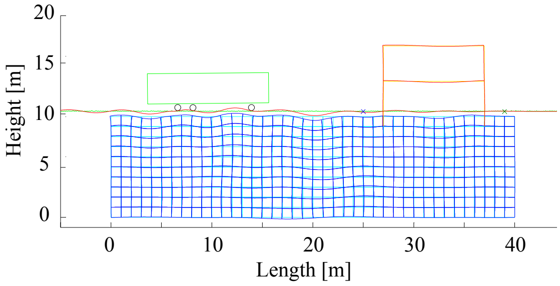

Figure 7: Snapshot from simulation of the reference case. The deformations are scaled by a factor of 5000. Total dof = 2911.

W_k and W_d will be used for vertical and horizontal vibration respectively. W_f is used to weight vibrations causing motion sickness. The instantaneous acceleration is calculated for both directions, whereafter the maximum transient vibration value (MTVV) is determined from:

$$\text{MTVV} = \max\left(a_v(t)\right), \qquad t \in [\tau; T], \tag{3}$$

$$a_v(t) = \sqrt{k_x^2\, a_{wx}^2(t) + k_y^2\, a_{wy}^2(t)}, \tag{4}$$

where k_x and k_y are multiplication factors set to 1.0 cf. (ISO 2631, 1997) and T is the simulation time. The following study focuses on the cobblestone pavement which is defined uniquely in each simulation due to the stochastic describtion. In order to account for the randomness at least three simulations will be conducted for each parameter combination and the mean value is presented. In order to determine a reference MTVV, a time series from the reference case is considered. The simulation is conducted using the properties listed in Table 3, where v_{veh} denotes the vehicle velocity while V_{brick} is the covariance of the brick length, see Section 4. A snapshot from the simulation can be found in Figure 7.

The vertical and horizontal acceleration of the node at the reference point is illustrated in Figure 8. As illustrated, the vertical accelerations are dominant compared to

Table 3: Parameters for reference case.

v_{veh}	V_{brick}	ξ_1	E
25 km/h	15%	1.00	300 MPa

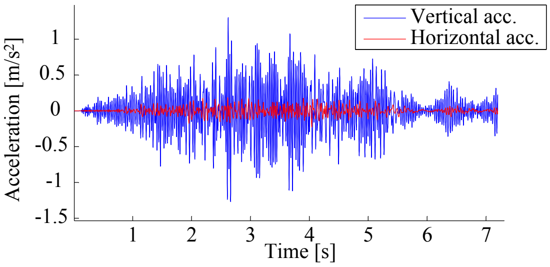

Figure 8: Acceleration time series at the reference node.

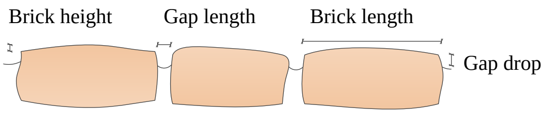

Figure 9: Parameters used for the description of a cobblestone pavement.

the horizontal. At the right side of the model, the road elements are supported by Kelvin supports, cf. Bach et al., (2013), and at these elements the surface force is not transmitted to the soil body. The first wheel enters the Kelvin part after 4.3 seconds, while the last wheel enters after 5.3 seconds at which time the accelerations tend to decrease.

The MTVV of the acceleration series in Figure 8 is 0.22 m/s^2, but due to stochastic variation of the cobblestone pavement additional simulations are conducted and the mean MTVV is calculated:

$$\mathrm{MTVV}_{ref} = 0.21\ \mathrm{m/s}^2. \tag{5}$$

4 Vehicle Analysis

The following study is conducted using only the vehicle and a non-movable surface profile. A brick pavement will be considered and it is assumed that the surface profile can be described by the parameters in Figure 9. The parameters are modelled as stochastic using the values given in Table 4. All parameters are assumed to be normally distributed.

It is unlikely that the tyre will be squeezed into the gap and the influence of the gap drop has therefore been eliminated. The surface profile is smoothened due to the tyre contact surface as described by Bach et al., (2013).

The vehicle velocity is an essential parameter when evaluating the reaction forces applied to the surface. Initially a simulation is conducted with a vehicle travelling at 25 km/h and the reaction force at the first tyre $f_1(t)$ is calculated using the relative compression of the tyre:

Parameter	Mean	Std. dev.	Lower limit
Brick length	20 cm	3 cm	10 cm
Brick height	1.0 cm	0.3 cm	0.0 cm
Gap length	2.5 cm	0.5 cm	1.0 cm
Gap drop	0.0 cm	0.0 cm	0.0 cm

Table 4: Stochastic parameters for brick pavement.

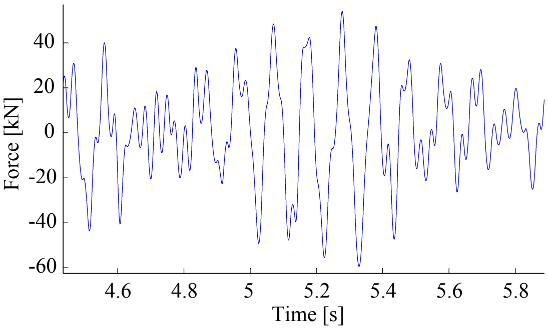

Figure 10: Excerpt of surface forces time series at the front tyre.

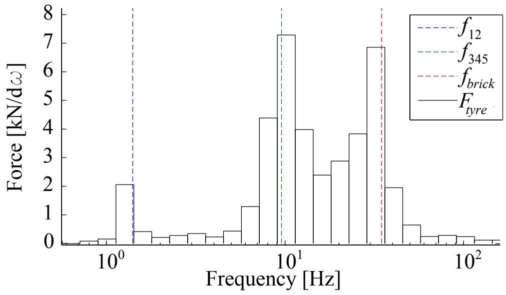

Figure 11: Frequency response for surface forces at the front tyre.

$$f_1(t) = k_1\left(x_1(t) - y_1(t)\right), \tag{6}$$

where $x_1(t)$ is the displacement of the first axel and $y_1(t)$ is the surface elevation at the first tyre. The vehicle is assumed to have a damping ratio of $\xi_1 = 0.01$ for the first eigenmode. An excerpt of the surface force time series is illustrated in Figure 10 and the frequency response of the reaction force is illustrated in Figure 11 using one third octave bands.

The reaction force response is plotted along with the eigenfrequencies of the vehicle and the mean frequency of the bricks, f_{brick}, which is calculated from:

$$f_{brick} = \frac{v_{veh}}{\mu_{brick} + \mu_{gap}} \approx 32\ \mathrm{Hz}, \tag{7}$$

where v_{veh} is the vehicle velocity. As illustrated the response contains peaks at both the eigenfrequencies and the brick frequency, and resonance may occur if the vehicle velocity is reduced. A parameter study is conducted to evaluate the influence of the vehicle velocity using the following procedure:

1. The vehicle is set to run across 200 bricks at a given velocity.

2. A zero down-crossing analysis is performed in which the wave heights in the surface force time series are identified.

3. The mean absolute surface force is determined as the average wave height.

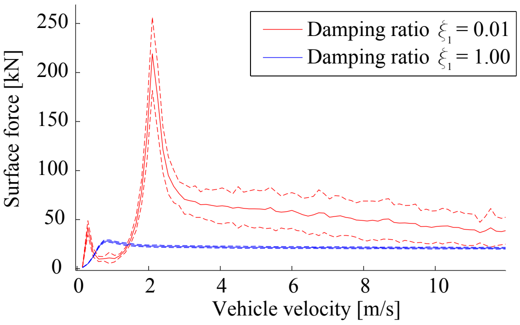

Figure 12: Variation in surface force due to vehicle velocity.

4. The procedure is repeated 100 times with a new surface generation.
5. Mean value, 5% and 95% quantiles are calculated.
6. Steps 1 – 5 are repeated with a new velocity.

An ideal vehicle can be assumed to have a damping ratio of 1.0 in the first eigenmode, while the damping ratio is likely decreased in a worn city bus. The procedure is therefore conducted using damping ratios of $\xi_1 = 1.0$ and $\xi_1 = 0.01$ and the results are illustrated in Figure 12.

The dashed lines above and below the curves indicates 95% and 5% quantiles, respectively. As illustrated the damping ratio of the first mode has a high influence when the vehicle travels at resonance velocities v_{12} and v_{345}:

$$v_{12} = (\mu_{brick} + \mu_{gap})\, f_{12} = 0.31 \text{ m/s} \tag{8}$$

$$v_{345} = (\mu_{brick} + \mu_{gap})\, f_{345} = 2.1 \text{ m/s} \tag{9}$$

Resonance velocities are hardly noticeable for the critically damped vehicle while the mean force is approximately ten times higher for the under critically damped vehicle at v_{345} and v_{12}. Both vehicles converge towards the same surface force of 20 - 22 kN at high velocities. The convergence value corresponds to complete compression of the tyre for the average elevation of the smoothened cobblestone surface profile μ_η of 0.69 cm:

$$F_{conv} = k_1\ \mu_\eta \approx 21 \text{ kN} \tag{10}$$

The average elevation of the smoothened surface profile can be calculated from wave counting. The possibility of dynamic amplification due to resonance is dependent on the variability of the pavement as well as the vehicle velocity. As illustrated in Figure 13 the individual bricks in a pavement can be almost identical or deviate significantly. In order to evaluate the effect of deviation a simulation is conducted for the under critically damped vehicle $\xi_1 = 0.01$ in which the covariance of the brick length, V_{brick}, is increased stepwise. The frequency velocity v_{345} is selected and the surface force is given in Figure 14.

Figure 13: Covarince of cobblestones, (left) high cov (right) low cov.

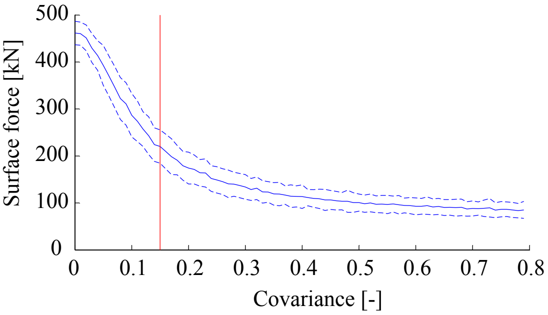

Figure 14: Variation in surface force due to covariance of brick length.

The dashed lines mark the 5% and 95% quantiles while the red line indicate the covariance based on data listed in Table 4. As illustrated, the deviation in brick length disturbs the resonance, whereby the surface force is reduced. The declination is mainly occurring in the interval $V_{brick} = 0 - 0.30$ in which the surface force decreases by 4% in average when the covariance is increased by 0.01.

All together it has been found that a vehicle travelling at resonance velocity with poor damping properties on a pavement with identically sized cobblestones can induce forces up to 20 times as high compared to the reference case. In reality, however, the situation mentioned is an extreme case and in Table 5 ratios are stated for more probable situations.

According to Dixon, (2007) passenger cars are usually designed to have a damping ratio between 0.2 and 0.8. A low damping ratio ensures a comfortable ride, whereas a high ratio improves the handling, which is preferred in sport and racing cars. Due to excessive damper wear or damage to the suspension system, the damping ratio may drop below 0.1 in which case the vehicle is considered unsafe. The paper by Dixon, (2007) does not provide any information regarding heavy vehicles but it seems fair to assume that transit busses are mainly designed for comfort. As demonstrated in Table 5, the surface force is highly dependent on the damping ratio while the covariance of the brick length is relatively insignificant especially for high damping ratios.

Table 5: Mean surface force ratios for combinations at resonance velocity $v_{veh} = 2.1$ m/s.

F/F_{conv}	$\xi_1 = 0.45$	$\xi_1 = 0.30$	$\xi_1 = 0.15$
$V_{brick} = 0.15$	1.15	1.28	1.81
$V_{brick} = 0.10$	1.17	1.31	1.89
$V_{brick} = 0.05$	1.16	1.31	1.93

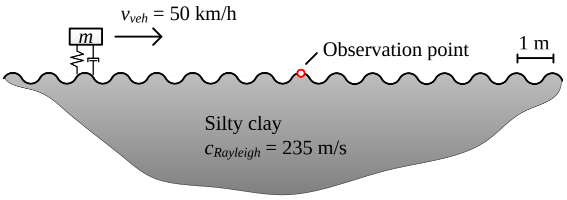

Figure 15: Setup for demonstration of Doppler effect.

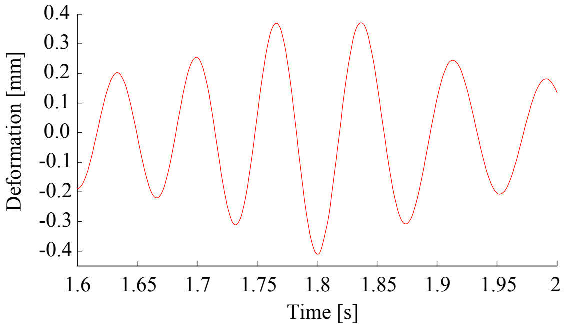

Figure 16: Compression and elongation of the wave period due to Doppler effect.

5 Resonance Effect

Using the results from Section 4 a series of critical cases are set up and compared to the reference case. Different resonance velocities are applied to match eigenfrequencies of the vehicle and the building. Some considerations have to be made regarding the Doppler effect when calibrating the frequency of the load from the moving vehicle to the eigenfrequency of the building. The influence of the Doppler effect can be demonstrated using the simulation in Figure 15. A single-degree-of-freedom vehicle is run across a sinusoidal-shaped road and, the deformations are measured in the observation point (O).

The vehicle is initiated at $x = 0$ and the observation point is located at $x = 25$. The vehicle passes the observation point at $t = 1.80$ s and the vertical deformations are plotted in Figure 16. The period of the waves is slightly different before and after the vehicle passes the observation point, which is evident when comparing the magnitude of deformation at $t = 1.6$ s and $t = 2.0$ s. Similarly, the frequencies before and after the vehicle has passed differ due to compression and elongation of the wave length. In Table 6 values of the response frequencies from the simulation are compared to theoretical values based on the vehicle velocity and the Rayleigh wave velocity.

The frequency in column one is the frequency perceived in the building. Heavy vehicles are likely to have a velocity between 5 – 40 km/h when crossing a cobblestone pavement; hence, the increase in load frequency will be between 0.5% and 4%. Taking account of the Doppler effect, simulations are conducted using variations of the following parameters:

Table 6: Changes in frequency due to Doppler effect.

	Before O	After O	Vehicle
Simulation	14.8 Hz	13.2 Hz	13.9 Hz
Theoretical	14.7 Hz	13.1 Hz	13.9 Hz

Table 7: MTVV ratios for critical combinations.

v_{veh} [m/s]	2.1 f_{345}	3.06 f_{b2}	3.63 f_{b4}	8.65 f_{b6}
$\xi = 1.00$ $V_{brick} = 0.15$	0.76	1.80	1.38	1.01
$\xi = 1.00$ $V_{brick} = 0.05$	0.76	2.82	2.09	0.95
$\xi = 0.10$ $V_{brick} = 0.15$	1.52	3.03	2.08	1.28
$\xi = 0.10$ $V_{brick} = 0.05$	1.62	4.47	2.15	1.43

- Vehicle velocity,
- Damping ratio of the first eigenmode of the vehicle,
- Covariance of the brick length.

The results of each simulation are evaluated according to Section 3, and the ratio of the weighted running r.m.s. acceleration compared to the reference case is stated in Table 7. The parameters and the MTVV of the reference case are stated in Table 3.

The simulations, in which the vehicle travels at its own resonance velocity with a damping ratio of 1.00, provide a lower MTVV compared to the reference case. As illustrated in Figure 12, resonance effects are eliminated due to the high damping ratio causing the magnitude of the surface forces to be similar. The vehicle travels at a lower velocity compared to the reference case whereby the damping in the building has a higher influence and ultimately the vibrations are reduced. When the damping ratio is reduced to 0.1, resonance in the vehicle becomes significant and the MTVV is approximately 50% higher compared to the reference case.

In columns 2 – 4 results are given for vehicle velocities causing resonance in the building. The MTVV ratios indicate that a velocity of 3.06 m/s is the most critical. As illustrated in Figure 5, the modeshape associated with f_{b1} causes the first floor to deform similar to the first mode of a double fixed beam while the deformations associated with f_{b2} and f_{b3} is comparable to the second mode of a double fixed beam. Consequently the deformations and hereby the vibrations are largest for the first mode. Similarly, larger rotations in the walls are required to generate the third mode compared to the second, whereby the MTVV-ratios are smaller in the third column.

Comparison of column 1 and columns 2 – 4 reveals that vehicle velocities causing resonance in the building are critical compared to velocities causing resonance in

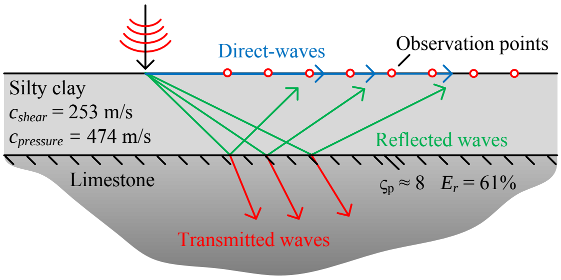

Figure 17: Setup for simulation of resonance reflection.

the vehicle. Additionally it has been found that resonance velocities of the vehicle are generally below 10 km/h given the assumed surface description even if vehicle parameters such as mass, stiffness and axel distance are varied by up to 50%. Despite the possibility of frequent stops the vehicle is likely to travel at higher velocity for most of the time whereby vehicle resonance is improbable.

It should be noticed that the conclusions made above are based solely on vibrations in the reference point at the first floor. Vibrations at other locations, e.g. at the walls or in the vehicle, may provide a different impression.

6 Soil Parameters

The following study examines the influence of the soil properties. The following two aspects are analysed:

- The influence of a rigid sub layer,
- The influence of soil stiffness in the top soil.

A rigid limestone layer is implemented at a depth d beneath the surface with the properties $E = 15$ GPa, $\nu = 0.3$ and $\gamma = 2000$ kg/m^3. Due to the impedance mismatch between the limestone layer and the silty clay layer, waves will be reflected at the stratum border. The implementation of a limestone layer has two contradicting effects:

- Deformations and hereby vibrations are reduced due to higher stiffness below the stratum border.
- Vibrations are contained in the system due to reflection at the stratum interface.

The reflection of waves can be estimated using wave progation equations, cf. Andersen, (2006). However, for the complex situation with a moving vibration source the calculations are comprehensive. To demonstrate the effect of a stratum interface, a simple simulation is conducted as illustrated in Figure 17. A sinusoidal load with a frequency of 100 Hz is applied to the surface for 5 milliseconds, corresponding to half a period. The response is recorded at observation points along the surface. In the figure, ς_p denotes the impedance mismatch related to pressure waves, and E_r is the energy reflection coefficient for pressure waves.

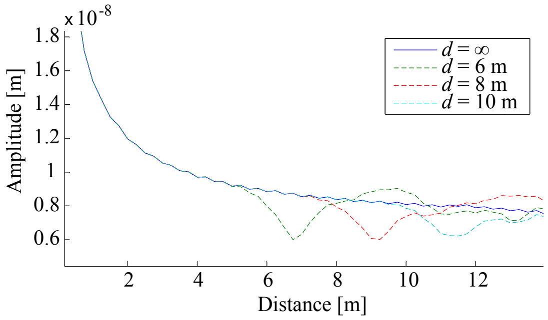

Figure 18: Wave amplitude for different stratum interfaces.

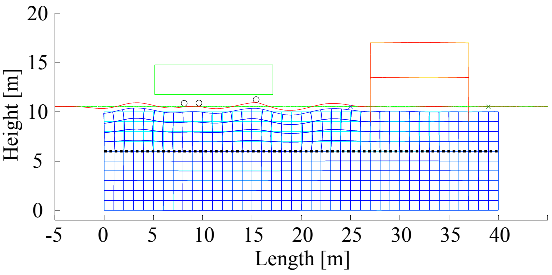

Figure 19: Snapshot from simulation with a limestone layer at depth $d = 4$ m. The deformations are scaled by a factor of 5000.

Three simulations are conducted for increasing values of d. The maximum amplitude at each simulation point is determined and plotted in Figure 18. A limit case is included as well in which the limestone layer is removed. As illustrated the simulations deviate from the limit case at different locations and as expected the deviation point is closer for small values of d. Deviating peaks in the response can be identified as reflected waves using wave velocities and analytical expressions for wave propagation in soil.

The deviation distance can be useful when evaluating whether direct Rayleigh waves will interfere with reflected pressure or shear waves. However, as illustrated, both negative and positive interference is occurring at the surface and it is therefore difficult to estimate, how a rigid sub layer will influence the magnitude of vibrations in a more complex situation.

In order to examine the effect of reflection for a vehicle crossing a cobblestone pavement, simulations are conducted in which a stratum interface is implemented in the reference case, cf. Section 2. A snapshot from a simulation with $d = 4$ m is presented in Figure 19. The dashed black line indicates the stratum interface and it is evident that deformations are occurring in the silty clay layer while the limestone layer is unaffected. The depth of the interface d is varied and the results are given in Table 8 in terms of the MTVV-ratio.

Table 8: MTVV-ratios for implementation of rigid sublayer.

Stratum interface	d = 4 m	d = 6 m	d = 8 m
MTVV-ratio	0.89	1.19	1.11

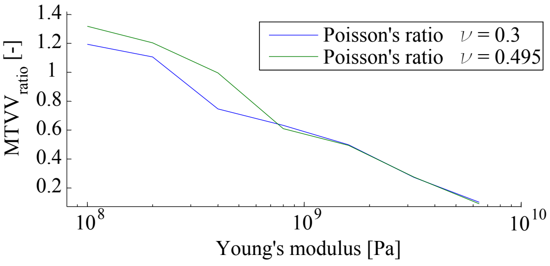

Figure 20: MTVV-ratios for variation in soil stiffness.

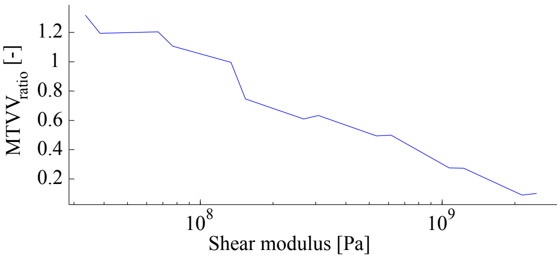

Figure 21: MTVV-ratios for variation in shear modulus.

As mentioned the influence of a rigid sub layer is difficult to estimate due to the complexity of the model and the moving vibration source. The results in Table 8 do not provide a distinct impression of the influence, though, the magnitudes of the MTVV-ratios indicate that the influence of the limestone layer is negligible compared to, e.g., the influence of the vehicle velocity and the vehicle damping ratio described in Section 5.

In order to evaluate the effect of soil stiffness, simulations are conducted in which Young's modulus is changed. Wave velocities are highly dependent on Poisson's ratio and two values 0.495 and 0.30 are applied representing saturated and unsaturated conditions respectively. The results in terms of MTVV-ratio are given in Figure 20.

The maximum transient vibrations appear to decrease approximately linear for exponentially increasing values of Young's modulus. The magnitude of vibration tends to be larger for $\nu = 0.495$ which is expectable, as Poisson's ratio influences the shear modulus,

$$G = \frac{E}{2(1+\nu)}. \tag{11}$$

In Figure 21 the MTVV-ratio is plotted as a function of the shear modulus. As illustrated the results form a relatively straight line which indicate that the vibration is more properly described in terms of the shear modulus.

7 Conclusion

A parameter study of traffic-induced vibrations in buildings has been presented in the article. The study is conducted using a two-dimensional finite-element model consisting of a moving vehicle, a road, a soil body and a building. In order to quantify the influence of different parameters, a reference case is set up in Section 2. The vibration is evaluated with respect to the perception of residents in the building using the procedure described in Section 3. In Section 4 the influence of vehicle velocity, vehicle damping ratio and surface variation is evaluated with respect to the reaction forces generated by the vehicle. A surface profile of cobblestones is considered and it is found that the reaction forces are increased significantly if the frequency of the cobblestones matches the eigenfrequency of the vehicle. However, the resonance effect is eliminated if the vehicle is critically damped. For a vehicle moving at resonance velocity, it has been found that the damping ratio of the vehicle has a higher influence compared to the covariance of the individual cobblestone lengths with respect to the reaction force.

In Section 5 simulations are conducted in which the soil body and the building are included. Critical cases are set up in which the vehicle travels at resonance velocities of either the building or the vehicle itself. Based on the simulations it has been found that the vibrations at the floor division are generally larger if the vehicle travels at velocities causing ressonance in the building. Furthermore, the simulations demonstrate that the amplification of vibrations due to resonance in the building is higher for the lower frequencies. Ultimately it has been found that the vibrations can be approximately 4.5 times higher if a poorly damped vehicle crosses a monotonous cobblestone pavement at resonance velocity compared to the reference case.

In Section 6 the influence of the soil body is investigated. A relatively stiff stratum is introduced causing part of the wave energy to reflect at the interface. Due to the moving vibration source it is difficult to predict the influence of the reflection. The simulations do not provide a distinct indication of the influence and the changes in vibration level are relatively small. Finally, the effect of the soil stiffness has been evaluated and it is found that the vibration decreases linearly when the stiffness is increased exponentially.

References

Andersen, **2006**. Lars V. Andersen. *Linear Elastodynamic Analysis*. 2006.

Bach, Vigsø, and Elmholt, **2013**. K. S. Bach, M. Vigsø, and M. Elmholt. *A fully coupled finite-element model for prediction of traffic-induced vibration in buildings*. 2013.

Cook, Malkus, Plesha, and Witt, **2002**. Robert D. Cook, David S. Malkus, Michael E. Plesha, and Robert J. Witt. *Concepts and Applications of Finite Element Analysis*. John Wiley and Sons, INC, fourth edition edition, 2002.

Dixon, **2007**. John C. Dixon. *The Shock Absorber Handbook*. Wiley, 2007.

Grønvald, 2013. Henrik Grønvald. *Tung trafik ødelægger gamle huse.* 2013.

Hunaidi, Guan, and Nicks, 2000. O. Hunaidi, W. Guan, and J. Nicks. *Building vibrations and dynamic pavement loads induced by transit buses.* 2000.

ISO 2631, 1997. International Standard ISO 2631. *Mechanical vibration and shock - Evaluation of human exposure to whole-body vibration*, 1997.

Kim, Chi, and Lee, 2006. B. S. Kim, C. H. Chi, and T. K. Lee. *A study on radial directional natural frequency and damping ratio in a vehicle tire*. 2006.

Kønigsfeldt, 2005. Steen Kønigsfeldt. *Rystelser fra trafikken.* 2005.

Lombaert, Degrande, and Clouteau, 2000. G. Lombaert, G. Degrande, and D. Clouteau. *Numerical modelling of free field traffic-induced vibrations.* 2000.

Lysmer and Kuhlmeyer, 1969. J. Lysmer and R.L. Kuhlmeyer. *Finite Dynamic Model for Infinite Media*. 1969.

Mhanna, Sadek, and Shahrour, 2011. Mohannad Mhanna, Marwan Sadek, and Isam Shahrour. *Numerical modeling of traffic-induced ground vibration*. 2011.

Sønderup, 2008. Anders Sønderup. *Asfalt på Boulevarden.* 2008.

Vigsø, Elmholt, and Bach, 2013. M. Vigsø, M. Elmholt, and K. S. Bach. *Considerations concerning finite-element modelling of traffic-induced vibration*. 2013.

Considerations concerning finite-element modelling of traffic-induced vibration

Michael Vigsø   Morten M. Elmholt   Kristian S. Bach
Lars V. Andersen
Department of Civil Engineering, Aalborg University, Aalborg, Denmark

Abstract

Ground-borne vibration due to heavy traffic has in many cases shown to cause discomfort for nearby residents. Vibrations can be caused by vehicles passing uneven pavements or road humps. However, the prediction of vibration levels prior to road design is, if any, based on experience and rule of thumb and the need for improved estimation models is obvious. This paper deals with dynamic response of a two story frame building due to passing of a three-axle bus on uneven pavement. The model accounts for interaction effects at the interface between the moving vehicle and the soil, and between the building and soil. A fully coupled three dimensional finite-element model requires a comprehensive amount of computer power and it is examined in which cases simplification to a plane model and neglecting of dynamic interaction can be advantageous.

1 Introduction

Traffic-induced vibration has frequently been reported for causing discomfort for residents of surrounding buildings (Sønderup, 2008). Vibration from traffic can be generated from heavy vehicles passing uneven pavements or speed bumps. In rare cases vibrations from vehicles has even shown to cause damage of neighboring buildings (Lombaert and Degrande, 2001). Several studies indicate that vibration due to traffic is of high importance and precautions must be taken during design.

In the work by Fiala et al., (2006) building vibration generated by a high speed train is modelled using numerical computation. A weak coupling between the incident wave field and the structure is assumed, meaning that the structure has no influence on the load generated from the train. The receiving model is a multi-storey office building resting on a soil body in which the structural response is examined for different coupling of the two parts.

Studies regarding dynamic response of buildings due to traffic-induced wave fields are described by François et al., (2007). The paper shows that neglecting of the interaction effects between structure and soil can have important consequences for vibration induced damage to buildings. The effect of interaction depends on the rigidity of the foundation compared to the stiffness of the underlying soil body. The model does not account for interaction between soil and vehicle, since it is assessed that the effect is minimal.

In the two papers by Bach et al., (2013) and Elmholt et al., (2013) a plane finite-element (FE) model is constructed in which a moving vehicle, a soil body and a structure are included and interact. The vehicle, a Scania City bus, is modelled as a multi-degree-of-freedom system that generates vibrations as it passes uneven pavements such as speed bumps and cobblestones. In the article by Bach et al., (2013) methods for constructing a fully coupled finite-element model for prediction of traffic-induced vibration in buildings are described. The article presents three different approaches for modelling the moving vehicle, in which two account for the dynamic interaction effects. Elmholt et al., (2013) used the same FE model to conduct a parameter study to identify sensitive parameters for vibration issues. The difference between a coupled and a decoupled model is not quantified in the studies. The scope of the following study is to analyse and quantify the methods and assumptions used by Bach et al., (2013). Interaction at the interface between the soil and vehicle will be analysed in Section 4 while the soil-structure interaction will be examined in Section 5. Considerations regarding the building model are presented in Section 5.1, in which issues regarding eigenfrequencies of coupled and decoupled models are described. One of the most pervasive assumptions made in the model is that the vibration problem sketched in Figure 1 can be simplified into a plane problem. In Section 6 the deviations between a two-dimensional (2D) and a three-dimensional (3D) model are quantified by constructing a full 3D model for comparison.

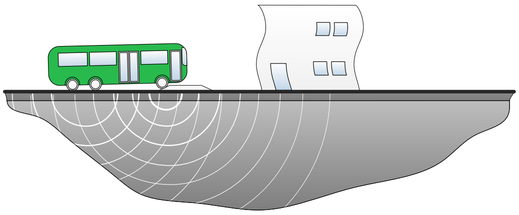

Figure 1: Illustration of problem with traffic-induced vibration.

The FE model is made using a mix of beam and continuum finite-elements with an overall geometry similar to the model used by Bach et al., (2013). A comparison is made regarding the consequence of simplification and computational cost.

2 Model Description

The 2D finite-element model used by Bach et al., (2013) and Elmholt et al., (2013) will be described in the following section. The same model composition will be reused in Sections 4 to 6 with minor deviations.

The finite-element model is illustrated in Figure 2 and can be divided into sub parts. The external forces are generated by a five-degree-of-freedom vehicle model with three axels. The vehicle travels with constant velocity across an irregular surface profile. The vehicle model is illustrated in Figure 3.

The vehicle is supported by Mindlin beam elements cf. Cook et al., (2002) which are connected to the soil body through interface elements. Outside the soil body and beneath the building, the road is supported by a Kelvin foundation. The Kelvin foundation is calibrated to approximate the properties of the soil body. This is done by adding stiffness and mass to the road corresponding to a soil column with half the height as seen in Figure 2. It was proven by Bach et al., (2013) that the inaccuracy of the simplification is insignificant in connection to the vibration in the building. The soil body is modelled using quadrilateral eight noded continuum elements and transmitting boundary conditions are applied at the submerged boundaries to simulate the infinite half space, cf. Lysmer and Kuhlmeyer, (1969).

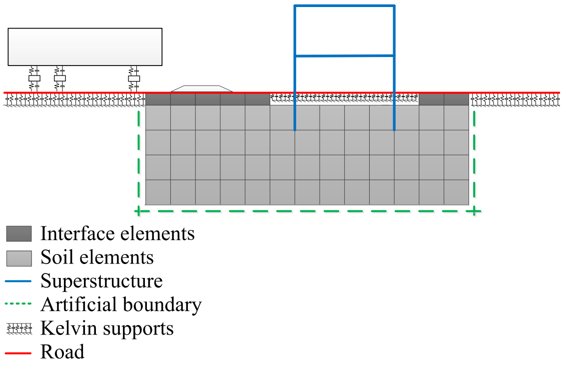

Figure 2: FE model of the problem sketched in Figure 1.

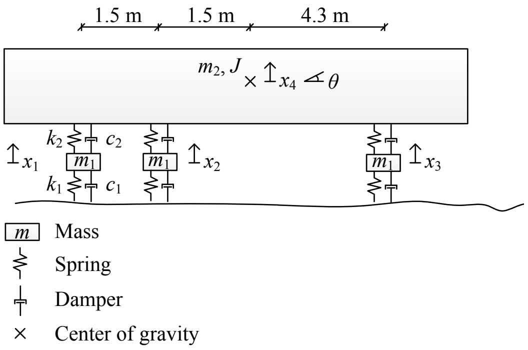

Figure 3: Dynamic model of three-axel vehicle.

Table 1: Parameters for reference case.

Parameter	Symbol	Unit	Value
Vehicle			
Length	l_{veh}	m	12
Height	h_{veh}	m	3
Total mass	M_{veh}	t	20
Tyre stiffness	k_1	kN/m	3000
Suspension stiffness	k_2	kN/m	600
Tyre damping	c_1	kNs/m	0
Suspension damping	c_2	kNs/m	176
Eigenfreq. 1, 2	f_{12}	Hz	≈ 1.4
Eigenfreq. 3, 4, 5	f_{345}	Hz	≈ 9.6
Road			
Height	h_{road}	m	0.30
Density	ρ	kg/m^3	2400
Young's modulus	E	GPa	5.0
Soil and interface			
Density	ρ	kg/m^3	1800
Poisson's ratio	ν	-	0.3
Young's modulus	E	MPa	300
Material damping	none	-	-
Mesh size	-	1×1	m
Building			
Height	h_{build}	m	7.5
Width	w_{build}	m	10.0
Beam height	h_{beam}	m	0.25
Density	ρ	kg/m^3	2500
Young's modulus	E	GPa	30
Damping ratio	ξ_1	-	0.01

The building consists of Bernoulli beam elements and all connections are rigid. For most of the following study, the properties presented by Elmholt et al., (2013) will be used. The complete amount of variables is comprehensive but the most descriptive parameters are presented in Table 1.

Only two eigenfrequencies are stated for the five-degree-of-freedom vehicle as eigenfrequency 1 and 2 and eigenfrequency 3, 4 and 5 are coinciding. The eigenfrequencies of the building are described in details in Section 5.1.

3 Model Interaction

The interaction between soil body and building is simply implemented by connecting the continuum elements in the soil with the beam elements of the building. However, the interaction between the vehicle and the deforming road is more complex as the vehicle moves during the simulation. Three different methods are considered by Bach et al., (2013) and are summarized below.

3.1 Separate Approach

The simplest option is to neglect the interaction effects and consider the vehicle and the road as two decoupled systems. Initially the five-degree-of-freedom vehicle is run across a fixed surface profile. The vehicle-road interaction forces (surface forces), f_i, from each axel can be calculated from the relative compression and rate of compression of the tyres:

$$f_i = k_1 \left(x_i - y_i \right) + c_1 \left(\dot{x}_i - \dot{y}_i \right), \quad i = 1,2,3, \tag{1}$$

where, y_i, as a function of time, contains the surface elevation at each axel. Next, a simulation is conducted in which the surface forces are applied to the stationary part of the model (the soil body, the road and the building).

3.2 Explicit Time Scheme

In the explicit time scheme the, two parts are still considered separately, but information is exchanged between the two models in every time step. In each time step, initially the response is calculated for the vehicle model. Next, the surface force is applied to the stationary model and an updated surface profile is generated from the deformation of the road. The updated surface profile is used in the second time step for the vehicle and so forth. The surface forces are calculated using,

$$f_i = k_1 \left(x_i - y_i - z_i \right) + c_1 \left(\dot{x}_i - \dot{y}_i - \dot{z}_i \right), \quad i = 1,2,3, \tag{2}$$

where, z_i contains the deformation of the road for each axel. Consequently a small time shift is created between the two parts depending on the time step Δt. In general, it has been found that the explicit time scheme becomes unstable if the value of Δt is too high which occurs particularly in cases of very soft soil or very stiff tyres.

3.3 Implicit Time Scheme

In the implicit time scheme the two parts are coupled into a single system matrix. In order to account for the movement of the vehicle, the system matrices are updated in every time step based on the position of the vehicle axels. Since the mass of the vehicle is lumped and located separately from the stationary part, the complete mass matrix becomes,

$$\mathbf{M} = \begin{bmatrix} \mathbf{M}_s & \mathbf{0} \\ \mathbf{0} & \mathbf{M}_v \end{bmatrix}, \tag{3}$$

where the subscripts s and v refer to the stationary part and the vehicle model, respectively. The complete stiffness matrix can be separated in a contribution from the decoupled models and a contribution from the interaction between the vehicle axels and the road,

$$\mathbf{K} = \begin{bmatrix} \mathbf{K}_s & \mathbf{0} \\ \mathbf{0} & \mathbf{K}_v \end{bmatrix} + \begin{bmatrix} \mathbf{N}^T k_1 \mathbf{N} & -\mathbf{N}^T k_1 \\ -\mathbf{N} k_1 & \mathbf{0} \end{bmatrix}, \tag{4}$$

where $\mathbf{N}$ is the shape function matrix for the beam elements used in the road. The damping matrix can be assembled in a similar manner. In general, the implicit time scheme has proved to be more stable and reliable compared to the explicit scheme. However, the computation time is significantly higher for large system matrices.

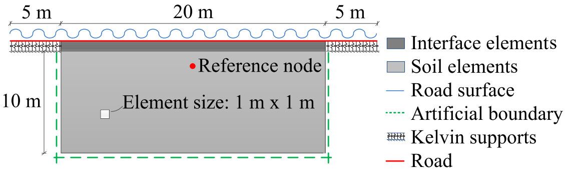

Figure 4: Reference case for evaluation of vehicle-road interaction.

4 Evaluation of Vehicle–Road Interaction

In general, the interaction between the vehicle and the soil body is expected to be more important for soft soil types compared to stiff soil types, e.g. limestone. The interaction effect can be quantified by comparing the response of the explicit and separate approaches to the response of the implicit method for different soil types. A reference case is set up with the geometry illustrated in Figure 4.

It should be noticed that the building has been removed for simplification. The vehicle is set to cross a sinusoidal road surface with an amplitude of 1 cm and a wavelength of 1 m at a velocity of 25 km/h. The response of the soil in the reference node is compared for variations of Young's modulus in the soil body for the different solvers. Except for Young's modulus, the properties presented in Section 2 are used. The reference node is located midway at a depth of 2 m as illustrated in Figure 4.

Figure 5 shows the resulting response for the three different approaches for two cases with widely different stiffness. The response is illustrated on a logarithmic scale to emphasize the deviation between the different approaches for very soft and stiff soil types. As initially expected, the deviation is larger for small values of Young's modulus, while it is difficult to see the difference between the three approaches for high values of the stiffness.

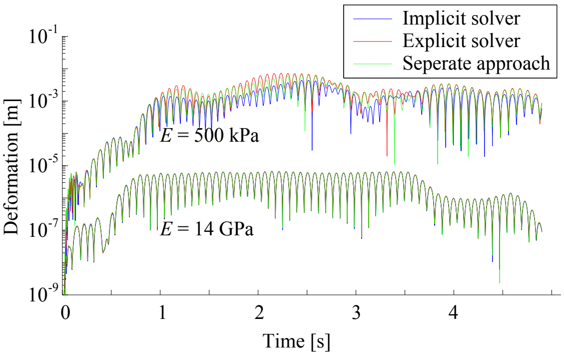

Figure 5: Deformation time series for very soft and stiff soil using different solvers. Note the logarithmic scale.

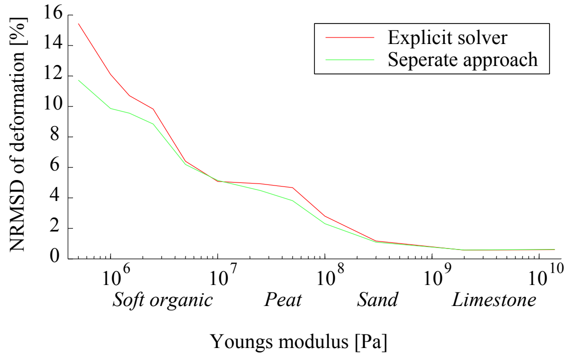

Figure 6: NRMSD of deformation in reference node as function of soil stiffness.

The normalized root-mean-square deviation,

$$\text{NRMSD} = \frac{1}{\hat{Y}_{\max} - \hat{Y}_{\min}} \cdot \sqrt{\frac{1}{n} \sum_{i=1}^{n} \left(\hat{Y}_i - Y_i\right)^2} \tag{5}$$

is used to quantify the difference between the three approaches for varying Young's modulus. The explicit and separate responses, $\hat{Y}$, are compared to the implicit approach, Y, by the NRMSD, see Figure 6.

For the reference case and for normal soil types as sand and clay the NRMSD is around 1%, when using either the explicit solver or applying the vehicle response separatly without accounting for interaction. The explicit scheme is in general seen to deviate more from the implicit scheme compared to the separate approach. This is in particular distinct for soft soil types due to time step shifting in the explicit approach, which to some extent can be reduced by lowering the time step.

5 Evaluation of Building-Soil Interaction

In the model presented in Section 2 the building and the soil body are coupled. In other studies, such as (Fiala et al., 2006), a decoupled model is used, in which the interaction is neglected. In the following study, the effects of the interaction is evaluated by comparing the response from a coupled and a decoupled model. A reference case is set up with the geometry illustrated in Figure 7. The properties presented in Section 2 are used. The vehicle is set to cross a sinus bump at a nominal speed of 25 km/h. The effects of interaction between the soil body and the building are first evaluated for the response in the soil body behind the building and then for the response at the floor division of the building. The two reference points are illustrated in Figure 7. A dominating parameter for the building-soil interaction is the kinematics of the building. Hence a more detailed analysis the natural frequencies of the building is enforced.

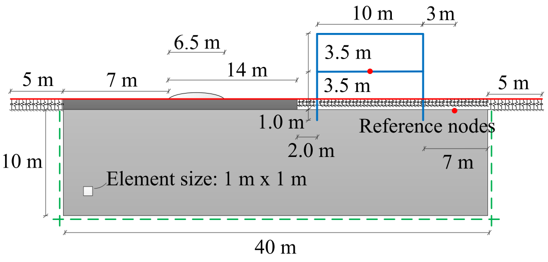

Figure 7: Reference case where building interaction is evaluated.

5.1 Building Eigenfrequencies

The natural frequencies of the building depend on the mass and the stiffness of both the structure and the soil body. The soil stiffness determines the degree of clamping of the building foundation. In the reference case from Section 2, the building is supported by a one meter deep foundation, which is connected to the continuum soil body elements. The material and geometric properties of the building, see Table 1, are calibrated to fit a typical two-storey concrete structure, in which the stiffness is adjusted to fit the range of typical eigenfrequencies according to Andersen (2006). The undamped eigenfrequencies f_i and eigenvectors $\mathbf{\Phi}_i$ of the model are determined by solving the general eigenvalue problem:

$$\left(\mathbf{K} - \omega^2\,\mathbf{M}\right)\,\mathbf{\Phi} = 0 \tag{6}$$

The degrees of freedom in the soil elements allow a number of eigenvalues, in which all the energy is located in the soil body. Due to transparent boundary conditions employed in terms of viscous dashpots rigid-body modes appear as well. In order to identify eigenfrequencies of the building, eigenmodes of the complete model are compared to the two simplified models of the building in Figure 8.

The part of the eigenvector corresponding to the house in model (a) are compared with model (b) by the Modal Assurance Criterion cf. Allemang, (2003):

$$\text{MAC}(\mathbf{\Phi}_1, \mathbf{\Phi}_2) = \frac{\left|\mathbf{\Phi}_1^T \mathbf{\Phi}_2\right|^2}{\left|\mathbf{\Phi}_1^T \mathbf{\Phi}_1\right| \left|\mathbf{\Phi}_2^T \mathbf{\Phi}_2\right|} \tag{7}$$

The MAC value will go to unity if the two eigenvectors $\mathbf{\Phi}_1$ and $\mathbf{\Phi}_2$ are identical. To sort out the modes of interest a threshold for the MAC value is set to 0.80, when comparing the modes of model (a) with model (b). Figure 9 shows the graphical representation of the MAC-values for the first six eigenmodes of the building compared with all the eigenmodes of the original model. Note that mode three is included with a threshold of only 0.45.

Figure 9 shows that for most of the eigenmodes multiple modes exist in the original model (a), which match

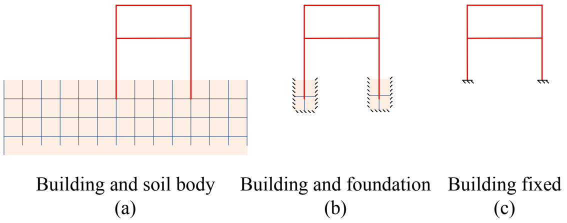

Figure 8: Modelling of building supports.

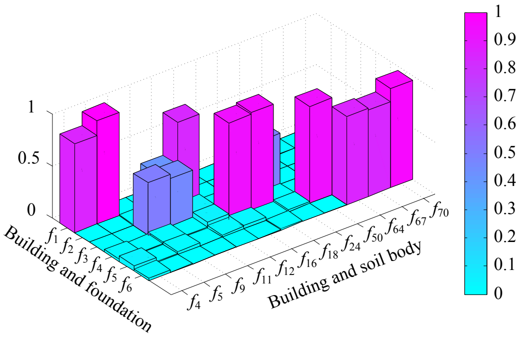

Figure 9: MAC between building and soil body and building and foundation.

the eigenmodes of the building. The explanation is that several possible modes can occur in the soil body simultaneously with movement of the same mode in the building. For mode three, it is necessary to lower the threshold of the MAC to 0.45 to find an estimate of the mode. In Figure 10 the third mode of model (b) is compared with the first two corresponding modes in the building for model (a). f_{11} is assessed to be the best estimate of the third mode based on Figure 10 even though the MAC is slightly higher for f_9.

In Table 2, the eigenfrequencies of the building are listed for the first six eigenmodes for model (a), (b) and (c). The chosen frequencies are based on the highest MAC values in Figure 9, while the frequency for mode three is based on engineering judgment. The mode shapes of the first six eigenmodes are illustrated in Figure 11. It is seen that the natural frequency of the building increases with the level of clamping of the foundation corresponding to changing the model from (a) to (b) and (c). For the sixth mode a drop in frequency is observed in Table 2 when going from model (a) to (b). This is due to the movement of the soil with little variation in modal shape of the building. As seen in Figure 9 three candidates appear for the sixth mode with the frequencies of 38.5, 39.2 and 40.1 Hz respectively. When using the simplified models for determining the eigenfrequencies a risk of changing the order of modes is present. This issue is seen in the case of mode two and three.

In the procedure above the material and geometric properties of the building are calibrated so the distribution of mass and stiffness result in reasonable eigenfrequencies and modes of the building. The connections between the walls and the floor divisions are assumed to be rigid, which is a simplification. A more realistic model with adjustable clamping of the floor divisions could be included in a further work.

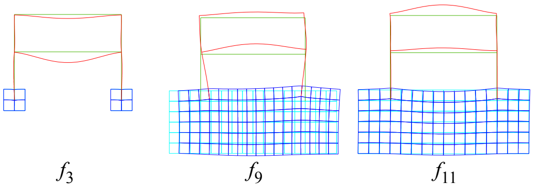

Figure 10: Comparison of eigenmode three of building.

Table 2: Eigenfrequencies for building.

	Model (a)	Model (b)	Model (c)
f_1	4.1 Hz	4.5 Hz	5.7 Hz
f_2	13.3 Hz	13.6 Hz	13.8 Hz
f_3	12.7 Hz	15.4 Hz	16.0 Hz
f_4	16.7 Hz	17.3 Hz	20.7 Hz
f_5	33.6 Hz	37.2 Hz	40.5 Hz
f_6	40.1 Hz	39.6 Hz	44.5 Hz

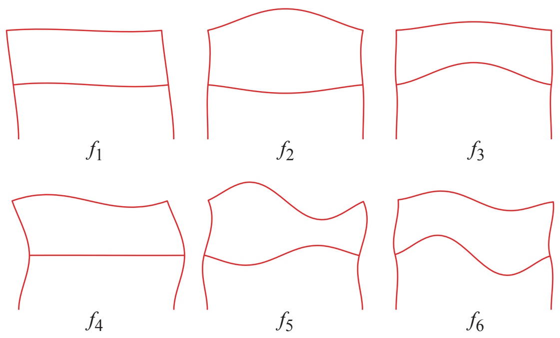

Figure 11: First six eigenmodes of building.

5.2 Effects of Interaction in the Soil Body

The effects of interaction between the building and the soil body are investigated for two cases, one with the reference case illustrated in Figure 7, and one without the building. The corresponding responses are shown in Figure 12 in the reference point at ground surface with and without the building. Only the horizontal response is presented in the following as a similar response is obtained in the vertical direction.

The deviation between the two simulations is evident at the end of the time series. As indicated, the soil continues to vibrate in the simulation in which the building is applied. This is due to eigenvibrations in the build-

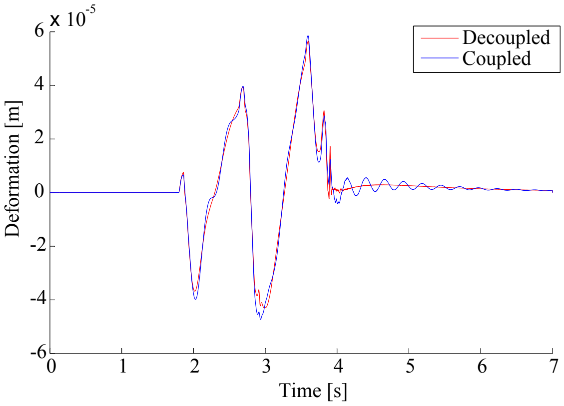

Figure 12: Horizontal deformation at the surface 3 metres behind building.

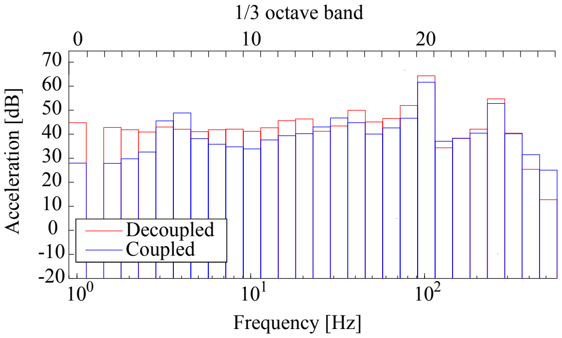

Figure 13: Horizontal acceleration at surface 3 m behind building.

ing transmitting forces to the ground. The frequency responses for the two simulations are plotted in one-third octave bands in Figure 13. As seen in Figure 13, the energy of the acceleration time series for the lower frequencies are reduced when the building is added to the model thus, the building serves as a damper or barrier regarding vibration behind it. However, the presence of eigenvibration in mode one at the frequency shown in model (a) in Table 2 is seen in band no. five and six for the coupled model.

5.3 Effects of Interaction on the Building

In contrast to the coupled model (a) in Figure 8, another common approach to model vibrations of buildings caused by either traffic-induced ground motion or earthquakes is to monitor the response from either real life measurements on the building foundation or to simulate similar response of the ground motions in a FE model. The response of the ground motions is then applied to a FE model of the building alone, model (c), modelled with movable supports as described by Nielsen, (2004). The quasi-static response $\mathbf{x}^{(0)}(t)$ of the building is given by:

$$\mathbf{x}^{(0)}(t) = \mathbf{U}\mathbf{y}(t) \tag{8}$$

where $\mathbf{y}(t)$ is the deformation time series of the movable supports and $\mathbf{U}$ is the influence matrix that links the response of the movable supports to the quasi-static movement of the remaining degrees of freedom. $\mathbf{y}(t)$ has six rows, the first three correspond to the first building support, while the last three correspond to the second support. By introducing a coordinate system $\mathbf{z}(t)$ relative to the moving supports, where $\mathbf{x}(t)$ is the total displacement of the building,

$$\mathbf{z}(t) = \mathbf{x}(t) - \mathbf{x}^{(0)}(t), \tag{9}$$

it is possible to rewrite the equation of motion of the building according to Nielsen, (2004):

$$\mathbf{M}\ddot{\mathbf{z}}(t) + \mathbf{C}\dot{\mathbf{z}}(t) + \mathbf{K}\mathbf{z}(t) = -\mathbf{M}\ddot{\mathbf{x}}^{(0)}(t). \tag{10}$$

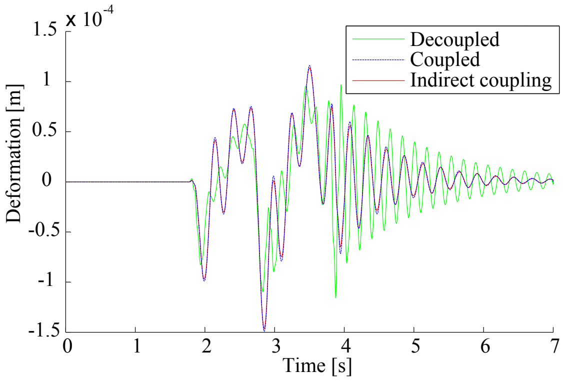

Figure 14: Horizontal deformation at the middle of the 1st floor for silty clay.

After solving equation (10) by applying the external forces from the right-hand side, the response in global coordinates is achieved by adding the ground motions from equation (8). Figure 14 shows the time series of the horizontal deflection at the middle of the 1st floor in the building for the coupled and the decoupled models. In the decoupled model, the two rotation degrees of freedom are obtained by linearization between two nodes in the foundation. The third curve, denoted ”indirect coupling”, shows the results of a simulation made for validation of the procedure. Here the ground motion at the foundations is firstly obtained with a model that includes the building. This ground motion is subsequently used as input in a model of the building but without the soil. Thus the difference from the decoupled model lies in the ground motion used as input for the building.

The simulation made for validation of the procedure indicates that the method of obtaining rotations from adjacent nodes is adequate. Hence the difference in response between the coupled and decoupled model must be assessed genuine. The response seems to damp out more rapidly in the coupled model even though the peak deflection in the floor is higher for the coupled model. Figure 15 shows the horizontal acceleration plotted in one third octave bands for the two models (a) and (c).

It is seen that the acceleration response is reduced for most of the octave bands. The first eigenmode is clearly seen to move up in frequencies from band 5-6 to 7-8 due to the stiffer fixed supports in model (c) compared

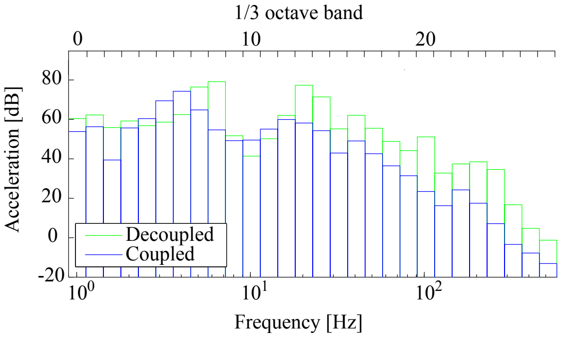

Figure 15: Horizontal acceleration at the middle of the 1st floor for silty clay.

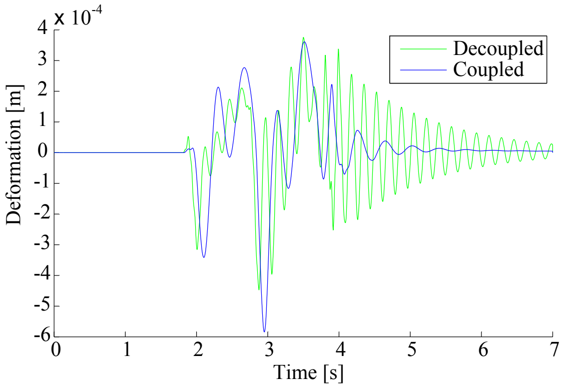

Figure 16: Horizontal deformation at the middle of the 1st floor for peat.

Table 3: Acceleration rms ratio between decoupled and coupled model.

	Peat	Silty Clay	Limestone
a_{rms} ratio	4.7	3.4	1.2

to model (a), which is in agreement with the previously calculated eigenfrequencies listed in Table 2. The effect of interaction for soft soil is illustrated in Figure 16, in which the response in the reference nodes are plotted for peat. As seen in the response, the building frequency for the coupled model (a) is lowered compared to Figure 14. The soil-structure interaction dependency on soil types are quantified in Table 3, in which the root-mean-square (r.m.s.) acceleration is listed as a ratio between the decoupled and coupled model. In general the interaction between the soil body and the building is seen to be significant, especially for soft soil types.

6 Effects of Spatial Dimension

The vibration problem shown in Figure 1 has so far been considered as a plane problem as illustrated in Figure 17. The purpose of the following study is to estimate the effect of the simplification. In order to do so, a 3D model of the problem is constructed. As illustrated in Figure 18 the 3D model can account for distance between the road and the building. In order to compare results from the 2D and the 3D model, a common reference case is set up. The 2D model is constructed according to the description in Section 2 with the properties given in Table 1 and the geometry defined in Figure 17.

6.1 Construction of 3D FE model.

In the 3D model the soil body is discretized using 26-noded isoparametric hexahedrons. As for the 2D model, transmitting boundary conditions are applied at the submerged boundaries to simulate the properties of an infinite half space as described by Lysmer and Kuhlmeyer, (1969). The system matrices for the elements are derived using full Gauss quadrature to avoid spurius modes. The

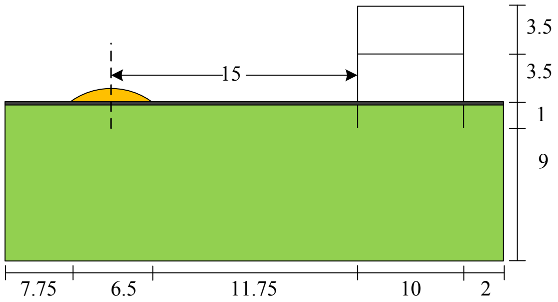

Figure 17: Plane view of the reference case.

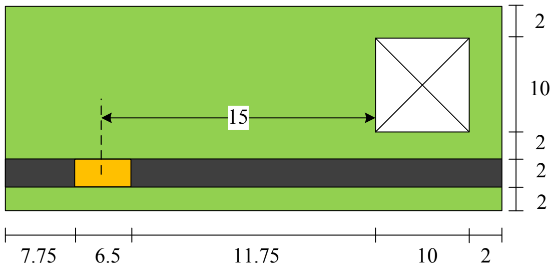

Figure 18: Top view of reference case.

building is constructed using 3D Bernoulli beam elements. The geometry and the static system of the building is illustrated in Figure 19. In the walls spanning in zy-plane, a cross has been implemented to add additional stiffness. Same principle is applied at the floor and roof of the building. An increase of stiffness in the given directions will lead to dynamic behavior more similar to the 2D building presented in Section 5.1. The element stiffness and mass of the building are calibrated to approximate the lower eigenfrequencies of the 2D building.

The road is modelled using Mindlin elements cf. Cook et al., (2002). The Mindlin elements are derived assuming quadratic shape functions and are therefore well suited to connect on top of the brick elements. The elements are aligned in a grid as shown in Figure 20 to provide bending stiffness in two directions. The bending stiffness of the road in the 2D model is defined as stiff-

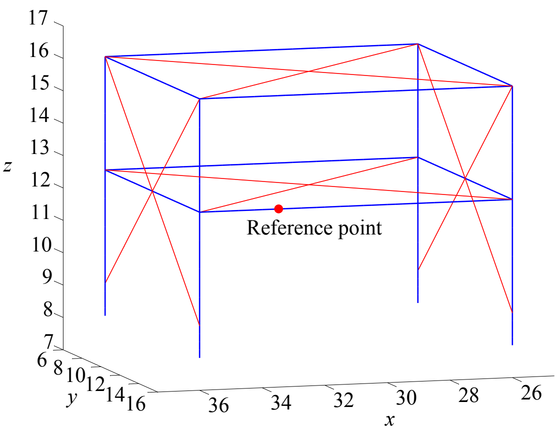

Figure 19: Model of house, total dof = 456.

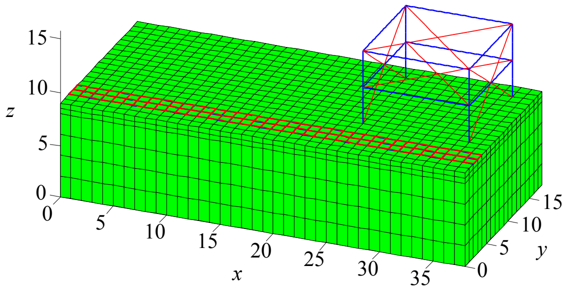

Figure 20: 3D FE model, total dofs = 14436.

ness per meter. In the 3D model the road is two metres wide and the road is calibrated to have a bending stiffness corresponding to a one meter wide road in the 2D model. Material and cross-section properties of the road and the building in the 3D FE model are given in Table 1. The vehicle and the soil parameters are the same as for the 2D model.

Due to extent of the computational effort the mesh refinement is less delicate for the 3D model compared to the 2D model presented in Section 2. When evaluating the inverse system matrices used for the time integration scheme, large matrices induce a comprehensive computation time and requires a large amount of memory. The soil body is meshed with element sizes increasing with depth. The top row of elements has the size of $x \times y \times z = 2\text{ m} \times 2\text{ m} \times 1\text{ m}$ in order to satisfy the geometry of the building. The underlying elements are larger in size to add more distance to the artificial boundary without increasing the size of the computational problem.

Based on the soil properties and the expected wave frequency in the following analysis the wave length for the Rayleigh wave is approximately 10 metres. The energy in the Rayleigh wave decreases exponentially from the surface and approximately two wave length below the surface the relative amplitude of the Rayleigh wave is below one percent. The depth of the model is nine metres whereby some of the energy will be absorbed at the boundaries. However, the geometry is similar to the geometry of the 2D model, whereby the error is comparable for the two models. In general, it is recommendable to use four elements per wave length, but due to computational limits the recommendation is only fulfilled in the x- and y-direction.

The mesh is illustrated in Figure 20. The eigenfrequencies of the building are calculated using the reduced system matrices as illustrated in Figure 8 (b). The first six modes are sketched in Figure 21 and the associated frequencies are listed in Table 4. The first eigenmode is identical to the 2D model with oscillation in the zx-plane while mode 3 for the 2D model can be seen as mode 4 in the 3D model.

Table 4: Eigenfrequencies.

f_1	f_2	f_3	f_4	f_5	f_6
4.55	9.01	11.04	12.87	15.07	19.41

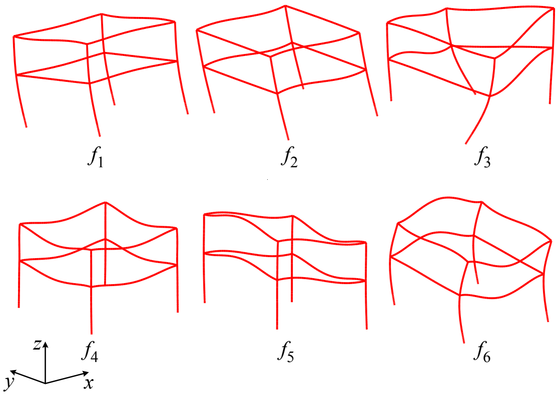

Figure 21: The first six eigenmodes of the three-dimensional building. Notice that crosses have been removed for visual purposes.

6.2 Load

The load is generated from the same three-axel bus with five degrees of freedom as described in Section 4. The load from each axel is applied on the road uniformly distributed in the y-direction as illustrated in Figure 22 and afterwards extrapolated to the nodes using shape functions. The vehicle and the rest of the model are modelled as two decoupled systems. In Section 4 it was demonstrated that a decoupling causes negligible deviations for stiff soils, like the soil presented in Table 1 while the computational effort is highly reduced. Simulations are conducted with load generated from a vehicle passing a speed bump and a cobblestone pavement. The bump used for simulation is a circle bump designed according to Vejdirektoratet, (2009) for heavy vehicles moving at a velocity of 25 km/h.

6.3 Wave Propagation

The main difference between the 2D model and the 3D model is related to the wave propagation in the soil. The amplitude of the vibration in the 3D model will be diminished compared to the 2D model due to out of plane dissipation of energy. A simple illustration of the issue is given in Figure 23. Assuming that the amplitude of deformation will decay proportional to the geometric expansion of the surface for the hemisphere and semicircle, respectively.

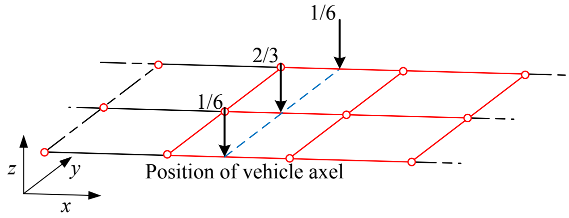

Figure 22: Load distribution on road.

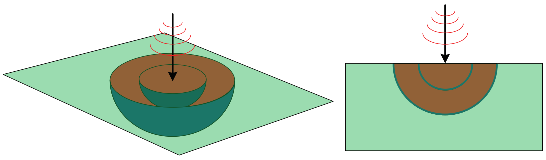

Figure 23: Wave propagation in 2D and 3D.

$$A_2 = A_1 \frac{R_1^2}{R_2^2}, \quad \text{for the hemisphere,} \qquad (11)$$

$$A_2 = A_1 \frac{R_1}{R_2}, \quad \text{for the semicircle,} \qquad (12)$$

where A is the amplitude and R is the distance from the source. For the simulation with the two models, it is more complex to predict the deviation due to geometric damping as the induced wave field does not propagate from a perfectly well defined point. Furthermore the geometric dissipation depends on the type of waves. However, the order of magnitude can still roughly be estimated for the illustration in Figure 18. It is assumed that the source of vibration is the center of the speed bump and that the energy transmitted into the building is proportional to percentage area of the foundation compared to the surface of the hemisphere and semicircle. Hereby, the acceleration in the 3D model should be in the order of 1 – 10% of the 2D model.

6.4 Results

Simulations are conducted for different cases for the 2D model as well as the 3D model. In order to quantify the difference between the models, the vibration at the first quarter point of the floor division is considered. For the 3D model the vibration in the beam at first floor facing the road is chosen for comparison. Since the object is to evaluate the human exposure to vibration, the accelerations are weighted according to the procedure described in (ISO 2631, 1997). The vibrations generated from traffic are mainly occasional shocks and in such case it is recommended to use the running root mean square method:

$$a_w(t_0) = \left\{ \frac{1}{\tau} \int_{t_0-\tau}^{t_0} [a_w(t)]^2 \, dt \right\}^{\frac{1}{2}}, \qquad (13)$$

where $a_w(t_0)$ is the instantaneous frequency-weighted acceleration for the observation time t_0. τ is the integration time for running averaging and is set to one second. The frequency weighting is performed based on one-third octave bands. The weighting functions and a guide for principal weightings are stated in (ISO 2631, 1997) as well. The results for the two models are given in terms of vertical acceleration and plotted in one-third octave bands in Figures 24 and 25 for the circle bump and in Figure 26 and Figure 27 for cobblestones.

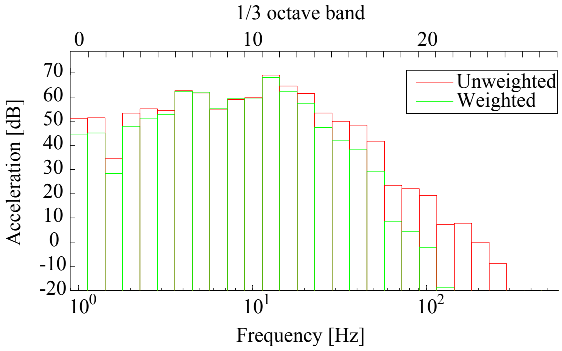

Figure 24: Vertical acceleration at the reference point at the first floor in the 2D model. Simulation for circle bump with a vehicle velocity of 25 km/h.

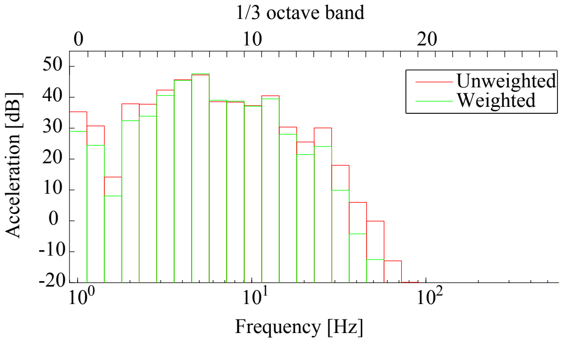

Figure 25: Vertical acceleration at the reference point at the first floor in the 3D model. Simulation for circle bump with a vehicle velocity of 25 km/h.

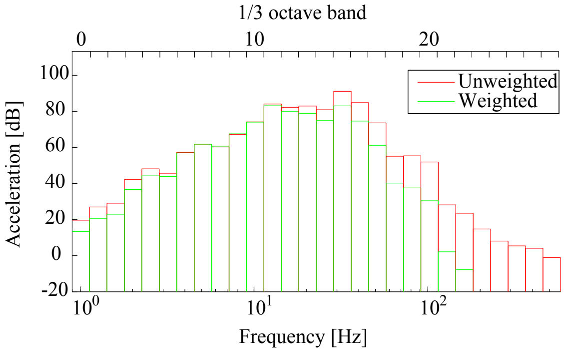

Figure 26: Vertical acceleration at the reference point at the first floor in the 2D model. Simulation for cobblestone pavement with a vehicle velocity of 25 km/h.

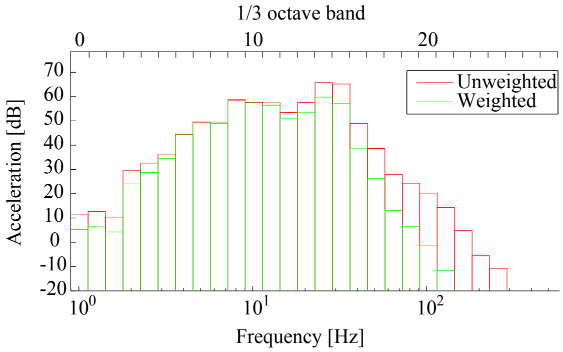

Figure 27: Vertical acceleration at the reference point at the first floor in the 3D model. Simulation for cobblestone pavement with a vehicle velocity of 25 km/h.

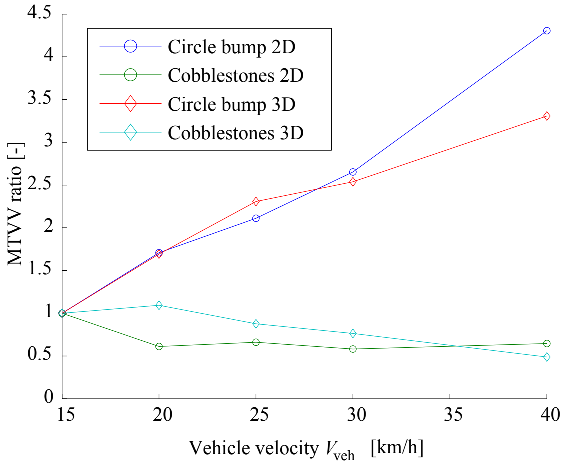

Figure 28: MTVV ratio at the reference point at the first floor in the 3D model.

As seen in Figures 24 – 27 the acceleration amplitude is highly reduced for the 3D model. The overall spectrum shows similarities with a peak in acceleration in the bands containing the building's eigenfreqencies. The spectrum of the 3D model shows lack in description of the higher frequencies. This may be due the fact that the mesh description is less fine for the 3D model compared to the plane model.

More simulations are performed in order to estimate if variation in parameters done in the 2D model can be used to identify critical cases prevalent for the full 3D model. The comparison for the analysis is given in terms of the maximum transient vibration value, MTVV, obtained from (ISO 2631, 1997).

$$\text{MTVV} = \max\left(a_v(t)\right) \quad t \in [\tau; T], \tag{14}$$

$$a_v(t) = \sqrt{k_x^2\, a_{wx}^2(t) + k_y^2\, a_{wy}^2(t) + k_z^2\, a_{wz}^2(t)}, \tag{15}$$

where, k_x, k_y and k_z are multiplication factors and set to 1.0 cf. (ISO 2631, 1997) and T is the total simulation time. The vehicle is run across the uneven pavement by shape of a circle bump and cobblestones, respectively, for different velocities. The cobblestone pavement used for the above analysis is generated using a stochastic description given by the parameters listed in Table 5. The results in terms of MTVV are normalized with respect to a reference velocity of $V_{veh} = 15$ km/h and plotted in Figure 28. Figure 28 indicates that the 2D model to some extent can be used for assessing the impact of choosing different speed reduction measures as bumps or cobblestones. However, only the ratios in changes can be used for assessing different designs while it must be kept in mind that the absolute values of accelerations are incomparable.

Table 5: Stochastic parameters for cobblestone pavement.

Parameter	Mean	Std. dev.	Lower limit
Brick length	20 cm	3 cm	10 cm
Brick height	1.0 cm	0.3 cm	0.0 cm
Gap length	2.5 cm	0.5 cm	1.0 cm

Table 6: Parameters for pavement description.

Cobblestones				
	Length		Height	
Parameter	μ_L	σ_L	μ_H	σ_H
Case 1	0.20	0.03	0.01	0.003
Case 2	0.20	0.03	0.015	0.003
Case 3	0.20	0.05	0.01	0.003
Case 4	0.30	0.03	0.01	0.003
Speed bump				
Parameter	Type		Distance	
Case 5	Circle		15 m	
Case 6	Sinus		15 m	
Case 7	Trapeze		15 m	
Case 8	Circle		10 m	

More simulations are conducted to conclude if the 2D model is suitable for a parameter study. Different types of cobblestones and speed bumps are used, all with a vehicle velocity of 30 km/h. The cobblestones are varying in brick height and the standard variation are varied leading to 4 pavement cases constructed from the stochastic parameters given in Table 6. The gab length between the cobblestones is the same as presented in Table 5. Results from the analysis are presented in Figure 29 and normalized with respect to Case 1.

Similar simulations are conducted for three types of speed bumps. The three speed bumps used for simulation are initially located with the same centre distance to the building as shown in Figure 18, all designed according to Vejdirektoratet, (2009). The results for the speed bumps are given in Figure 30 and normalized with respect to Case 5. Note that one simulation is conducted for the circle bump at a distance closer to the building.

In general a good coherence is observed between the models in the normalized domain. A change in the 2D model leading to an increased level of vibration is recip-

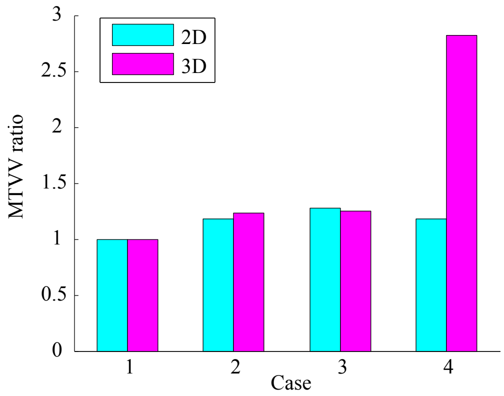

Figure 29: Comparison for different cobblestone pavement.

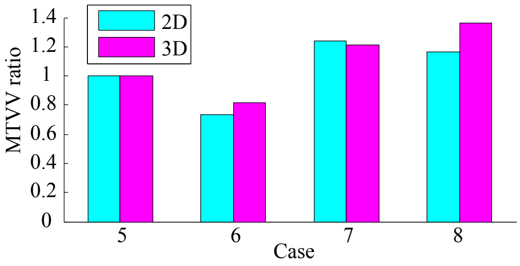

Figure 30: Bump types and position.

rocal in the 3D model. Only in Case 4, a high deviation between the models is observed. The cobblestones in this case have an increased mean value of the length forming a mean load frequency of

$$\overline{f} = \frac{V_{veh}}{\mu_L + \mu_{Gab}} = 25.64 \text{ Hz}. \qquad (16)$$

According to Section 5.1, no eigenmodes near this frequency was found for the 2D model. When evaluating the eigenmodes for the 3D model at higher order, the 11th mode is found at a frequency of 25.23 Hz. The eigenmode is illustrated in Figure 31. This example illustrates the importance of the kinematics of the building. The 3D model has a higher modal density than the plane model. Hence, the chance of resonance is higher when forming the cobblestone pavement.

7 Conclusion

A study of the dynamic response of a two-storey frame building exposed to gound-borne vibrations caused from passing of heavy vehicles has been conducted. The response has been analysed under consideration of different assumptions and levels of interaction between the systems. The observations has lead to the following conclusions:

- The influence of interaction effects at the interface between the moving vehicle and the soil can be neglected for common occurring soil types. The magnitude of deviation depends on the stiffness of the soil and the properties of the vehicle. The analysis presented in this paper is carried out for one reference vehicle and shows that the deviation is at a magnitude less than 2% for soil types commonly found in Denmark. The decoupling of systems reduces the computational cost markedly.
- When constructing a FE model to predict the level of traffic-induced vibrations at neighbouring buildings, an essential parameter is the dynamic modelling of the building. The dynamic response of the building is sensitive to assumptions regarding clamping of the foundations, and a decoupling from the soil may lead to major deviations in response. The presence of a heavy building has shown to give a coupling back to the soil body in terms of both amplitude and frequency. Hence, ground measurements at bare fields cannot be directly applied in a model without considerations regarding interaction effects from the structure back to the soil.
- A 3D FE model has been constructed to estimate the deviation between the 2D and the 3D model. In general the 3D model requires a vast amount of computational power compared to the 2D-model and it is therefore unsuitable for parameter studies. Hence it was examined if the plane model is applicable for this purpose. Simulations were conducted in which different sets of cobblestones and speed bumps were included. In general it was seen that a change in the 2D model was recognized in the 3D model.
- When comparing the two models, a highly dominant parameter is kinematics of the building. In Section 6.4 it was demonstrated how crucial effect a change in parameter can cause if only one of the models is experiencing resonance. Based on the analysis conducted during this study it seems that the 2D model to some extent is applicable for a parameter study. However, it should be kept in mind that some 3D effects are neglected when evaluating the eigenmodes for the building and that the amplitudes of vibration deviate significantly.

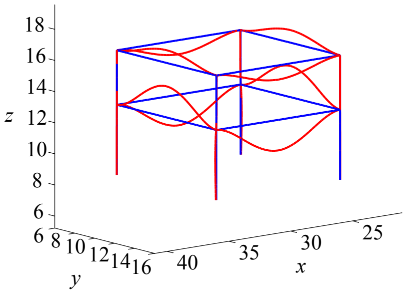

Figure 31: Mode 11 at 25.23 Hz.

In Section 5 it was seen how the presence of a building can influence the vibrations in the soil. A natural field of study is to examine how the change grows with increased number of building. In the same section when interaction effects are examined, only one type of foundation is considered and an interesting point of view would be to examine the influence of e.g., a basement. It was found that a dominating parameter is the kinematics of the building. Since the house used in this study is a very crude simplification, a more detailed modelling of the building would be an obvious choice of further work.

References

Allemang, **2003**. Randall J. Allemang. *The Modal Assurance Criterion – Twenty Years of Use and Abuse*. 2003.

Andersen, **2006**. Lars V. Andersen. *Linear Elastodynamic Analysis*. 2006.

Bach, Vigsø, and Elmholt, **2013**. K. S. Bach, M. Vigsø, and M. Elmholt. *A fully coupled finite-element model for prediction of traffic-induced vibration in buildings.* 2013.

Cook, Malkus, Plesha, and Witt, **2002**. Robert D. Cook, David S. Malkus, Michael E. Plesha, and Robert J. Witt. *Concepts and Applications of Finite Element Analysis*. John Wiley and Sons, INC, fourth edition edition, 2002.

Elmholt, Bach, and Vigsø, **2013**. M. Elmholt, K. S. Bach, and M. Vigsø. *Parameter studies of traffic-induced vibration using a finite-element model.* 2013.

Fiala, Degrande, and Augusztinovicz, **2006**. P. Fiala, G. Degrande, and F. Augusztinovicz. *Numerical modelling of ground-borne noise and vibration in buildings due to surface rail traffic*. 2006.

François, Pyl, Masoumi, and Degrande, **2007**. S. François, L. Pyl, H.R. Masoumi, and G. Degrande. *The influence of dynamic soil and structure interaction on traffic induced vibrations in buildings*. 2007.

ISO 2631, **1997**. International Standard ISO 2631. *Mechanical vibration and shock - Evaluation of human exposure to whole-body vibration*, 1997.

Lombaert and Degrande, **2001**. Geert Lombaert and Geert Degrande. *Study of Determining Factors for Traffic Induced Vibrations in Buildings*. 2001.

Lysmer and Kuhlmeyer, **1969**. J. Lysmer and R.L. Kuhlmeyer. *Finite Dynamic Model for Infinite Media*. 1969.

Nielsen, **2004**. Søren R. K. Nielsen. *Vibration Theory, Vol. 1*. 2004.

Sønderup, **2008**. Anders Sønderup. *Asfalt på Boulevarden.* 2008.

Vejdirektoratet, **2009**. Vejdirektoratet. *Byens trafikarealer - Hæfte 7. Fartdæmpere*, 2009.

Program Review

Program Review

A main part of the master project consists of constructing a total finite-element (FE) model for modelling traffic-induced vibration. The model includes a moving vehicle, a continuum soil body and a building. All parts are connected and interact with different interfaces. The main model is two-dimensional (2D), while a simplified comparable three-dimensional (3D) model is made for comparison. Along with the main 2D program several additional programs are developed in order to evaluate and validate methods, assumptions and results.

All the programs are made in MATLAB (Matrix Laboratory), which is a numerical computing environment developed by MathWorks. In the following sections, the structure of the main program and some selected additional programs are presented. For technical description of the program refers to the background report and Article # 1. Variables and symbols will not be explained in the review, but are explained in the background report and in the articles. The different programs can be found on the attached DVD.

Main Program

The general structure of a FE model consists of three parts; preprocessing, processing and post processing. The first part defines the material, geometry, topology, load and boundary conditions. The second part assembles the finite-elements in a total model and solves the selected problem. The third part is processing of results from e.g. nodal displacements to Gauss points or displacements to strains and stresses. The overall structure of the 2D FE model is illustrated in Figure 7.

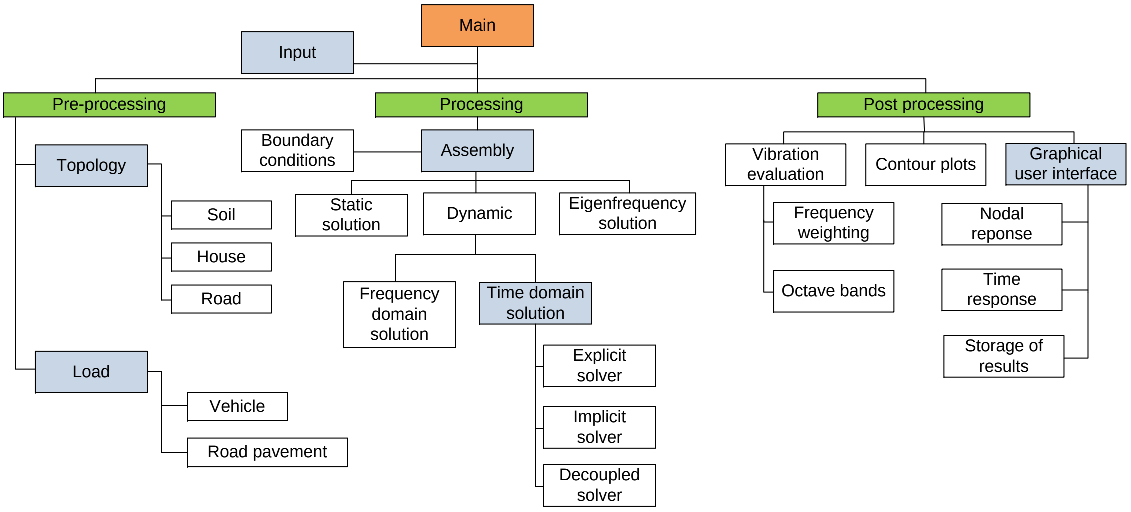

Figure 7. Overall structure of 2D FE model for modelling traffic-induced vibration.

The program is run through the *main.m* file, in which a current setup is loaded by the *input.m* file as illustrated in Figure 7. In the following, the highlighted (blue) boxes are elaborated.

Input

The *input.m* file assembles almost all information of the model in the two global structs listed in Table 1. All other parts of the FE model use the two structs to access the necessary information for the further computation.

Output	Description
Info	Geometry, materials, model parts and solution type
Input	Load and boundary conditions

Table 1. Variables in *input.m*.

Topology

Defines the topology and discretizes the mesh of the total model with the selected model parts (vehicle, road and building) based on the information in the *info* struct. The output variables contain subvariables for the different model parts.

Input	Description
Info	Geometry, materials, model parts and solution type
Output	Description
NodeCoor	Nodal coordinates
NodeDof	Nodal degree of freedom numbering
ElemNode	Node numbers in elements
ElemDof	Element degree of freedom
ElemMat	Element material
Info	Updating info with information of mesh

Table 2. Input and output variables in *Topology.m*.

Load

The *load.m* file is chosen by the *input* struct, and can in principle define a variety of different loads cases as e.g. static or dynamic loads.

Input	Description
m_1, m_2, k_1, k_2, c_1, c_2	Vehicle properties, e.g. mass, stiffness and damping
r_1, r_2, r_3, h_v, b_v	Vehicle geometry
v_{veh}, dt, T	Time description
Surface type	Surface description (cobblestone or speed bumps)
Output	**Description**
$\mathbf{M}_v$, $\mathbf{C}_v$, $\mathbf{K}_v$, $\mathbf{U}$	Vehicle system matrices
s, y, dy	Road description vectors

Table 3. Input and output variables in *Load_Vehicle.m.*

The standard *load.m* file, however, contains the vehicle passing different road surface types. The *load.m* file is an input file as the one denoted *input.m*, with the difference that the *load.m* file defines and computes the vehicle and road properties.

Assembly

The *assemble.m* file is evaluated in the *main.m* file under the processing part, as illustrated in Figure 7. The assemble script is divided into the following four parts.

Assemblence of:

- Soil body elements
- Building elements
- Interface elements
- Road elements

where, the subvariable *info.modelpart* determines which parts that have to be evaluated. Each part contains a loop over the different element types, where the variable *ElemDof* determines the position in the global matrices, where the local element matrix is inserted.

Output	Description
$\mathbf{M}_s$, $\mathbf{C}_s$, $\mathbf{K}_s$	Global matrices for stationary part

Table 4. Output variables in *assemble.m.*

The *assemble* file is not written as a function, but as a script. In this way all the global variables needed for assembling the global system matrices are accessible. This is e.g. the topology variables, material and geometry of elements, model- and element parts. If the transparent boundary conditions are applied in a dynamic analysis, they will be executed as a contribution to the global damping matrix.

Time Domain Solution

The dynamic time domain options are evaluated in the processing part of the *main.m* file based on the subvariable *info.SolType*. Three different solvers are available, all based on the Newmark time integration algorithm, in which the difference is the method of coupling the moving vehicle to the stationary part of the FE model. The output of the solvers are in general the time series for the deformation, velocity and acceleration for all degrees of freedom in the model.

Input coupled solver	Description
NodeCoor, *ElemNode* and *ElemDof*	Topology
$\mathbf{M}_s$, $\mathbf{C}_s$, $\mathbf{K}_s$	System matrices for stationary part
$\mathbf{M}_v$, $\mathbf{C}_v$, $\mathbf{K}_v$	System matrices for vehicle
t, s, y and dy	Road surface
Info	Everything else
Input decoupled solver	Description
$\mathbf{M}_s$, $\mathbf{C}_s$, $\mathbf{K}_s$	System matrices for stationary part
$\mathbf{F}$	Vehicle reaction forces (from *Load_Vehicle.m*)
t, dt	Time description
Output	Description
u, v and a	Response time series

Table 5. Input and output variables in *Time_domain_solution*

Graphical User Interface

The graphical user interface (GUI) collects a range of different plots and visualisation functions for evaluating the computed results. The GUI allows visualisation of time domain response of vehicle wheels and chassis, road, soil body and building as illustrated in Figure 8. In addition to this, the nodal response of the different parts, vehicle, road, soil body and building can be plotted in terms of deformation, velocity or acceleration as illustrated in Figure 9 for a deformation time series at the first floor in the building.

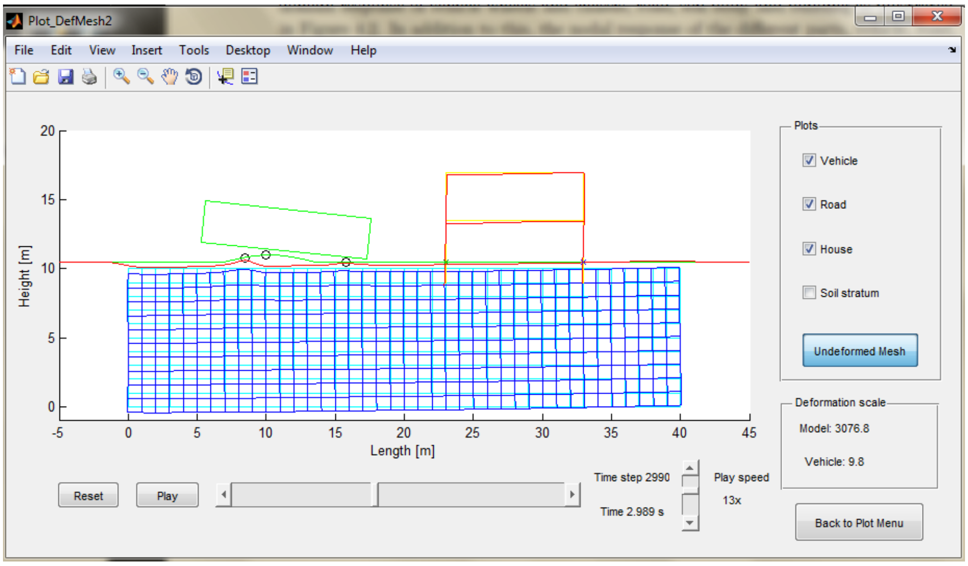

Model: 3076.8

Vehicle: 9.8

Time step 2990

Time 2.989 s

Play speed 13x

Figure 8. Example of time domain response in GUI.

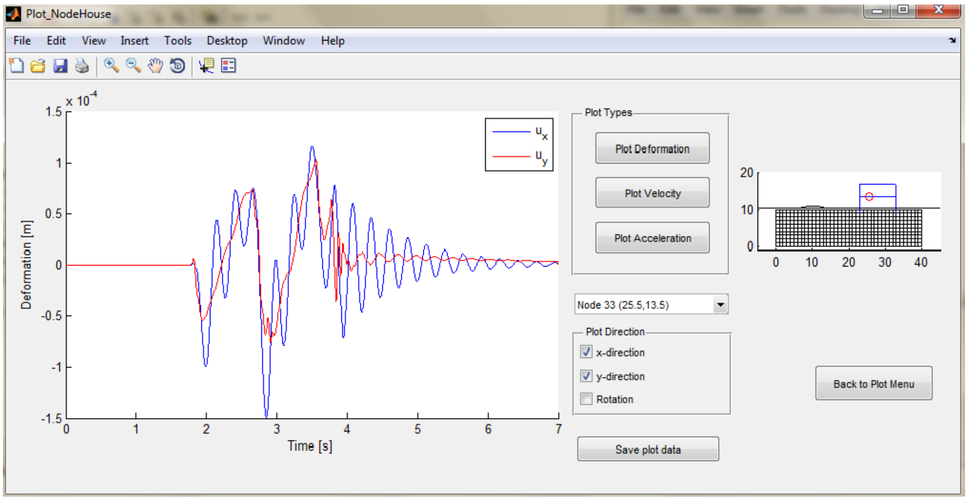

Node 33 (25.5,13.5)

Plot Direction

☑ x-direction

☑ y-direction

☐ Rotation

Figure 9. Example of nodal response evaluation in GUI.

Additional Programs

Along with the main 2D model, several additional programs are developed. The most comprehensive is a 3D model equivalent to the main 2D program, while the other additional programs are minor programs used in the validation process of the main 2D program or to analyse the results from the 2D and 3D program for the articles. The additional programs are listed in the following, while some selected programs are elaborated afterwards.

- 3D FE program
- 2D FE program of building
- Acceleration evaluation
- Frequency domain solution
- Kelvin model
- Mindlin elements
- Spurious mode
- Vehicle model

3D FE Program

The structure of the 3D program is in general similar to the main 2D program as shown in Figure 7. However, some simplifications are made in the 3D program. The inputs for a simulation are made directly in the *main3D.m* file, while the vehicle load is computed in the same way as for the 2D program. It is possible to analyse the static and dynamic response or examine the eigenmodes. A set of new post processing plot functions are added to evaluate the time response of the soil body and the building in three dimensions.

2D FE Program of Building

The purpose of the program is to evaluate the response of the building due to ground vibrations applied on movable supports. The structure of the program follows the general FE program structure illustrated in Figure 7. The model setup is made in the *main_building.m* file such as geometry, material, load and boundary conditions. Time series of ground motions from the main

2D program can be applied as loads on the supports of the building using an influence matrix, in which the response of the movable supports are linked to the quasi-static movement of the building.

Vehicle Model

The program is developed to construct and test the vehicle model separately and to develop the interaction algorithms for the vehicle passing a simply supported beam. Besides the necessary input parameters for the vehicle and beam, different functions for speed bumps are used to construct time series for the road surface elevation. The response of the vehicle chassis and suspension system or the interpolated response of the beam surface are visualised using different plot functions.

After testing and validation of the program, it has been incorporated in the main 2D FE model. The vehicle model is build in as the *Load_Vehicle.m* file, while the speed bumps are incorporated as road-input functions. The different interaction algorithms are incorporated in the main 2D program under the processing part to account for interaction between the vehicle and the soil body. The vehicle plot functions are refined and incorporated in the GUI under the post processing part of the main 2D program.

Discussion

Discussion

The master thesis project outlined in the previous chapters includes the construction and utilisation of a two-dimensional finite-element model to simulate traffic-induced vibrations. The construction of the model, a parameter study and considerations regarding the essential assumptions are described in three articles intended for publication. The usability of the model and considerations regarding improvements and further work are discussed in the following.

The main thesis in the project is inspired by an episode in Aalborg at Boulevarden in which the municipality had to remove an expensive cobblestone pavement due to vibration in nearby buildings. The episode may have been avoided if a dynamic analysis had been performed in the design phase. The finite-element model proposed in Article 1 can be used to perform such analysis. However, as described in Article 3 the two-dimensional simplification fails to provide reliable estimates regarding the magnitude of vibration, mainly due to the issue of three-dimensional wave propagation. Instead the model is applicable to clarify the differences between different designs, e.g. by conducting a parameter study such as the study in Article 2. As demonstrated in Article 3, the changes in response achieved by a two-dimensional model due to a modification of the design are comparable to the changes, predicted by a three-dimensional model.

In connection to further developments of the model it would be reasonable to conduct a field study. Several assumptions and simplifications are made in both the three-dimensional and the two-dimensional models, and measurements from a suitable experiment could help clarify, whether these assumptions are comparable to reality. For example, an experiment could be conducted in which the vibration in a building is monitored as a bus passes a nearby speed bump. Initial examinations could be used to determine the dynamic properties of the vehicle and the building. Comparisons could then be made between the experimental results and results from a simulation conducted using the two-dimensional finite-element model.

Another obvious way to improve the two-dimensional model is to expand it into a three-dimensional model as described in Article 3. However, due to the capacity of today's computers three-dimensional models are highly time consuming and inapplicable in parameter studies. In a design situation a recommendable procedure would therefore be to estimate a reasonable design from a parameter study using the two-dimensional model, where after the expected magnitude of vibration can be calculated using a three-dimensional model.

Bibliography

Grand, 2013. Hans Grand. *Absolut dB-skala*, 2013. URL `http://hansgrand.dk/content/om-stoj/absolut-db-skala/`.

NBC, 2012. News NBC. *Earthquake in the Filipines*, 2012. URL `http://photoblog.nbcnews.com/_news/2012/02/07/10340040-filipinos-grieve-as-earthquake-death-toll-rises?lite`.

NDT, 2013. Nondestructive Testing NDT. *Ultrasonic pipeline test*, 2013. URL `http://www.ndt-ed.org/EducationResources/CommunityCollege/Ultrasonics/SelectedApps/weldments.htm`.

Nordjyske, 2012. Nordjyske. *Asfalt på Boulevarden*, 2012. URL `http://nordjyske.dk/nyheder/asfalt-paa-boulevarden/91ba547a-9a8d-4d16-b83d-e747b2751bab/4/1513`.

UPMC, 2013. University of Pittsburgh Medical Center UPMC. *Obstetric Ultrasound*, 2013. URL `http://www.upmc.com/services/imaging/services/women/services/ultrasound/pages/obgyn-ultrasound.aspx`.

US, 2013. Department of Defense US. *Fighter jet breaking the sound barrier*, 2013. URL `http://www.defense.gov/WeekInPhotos/WeekInPhotosSlideShow.aspx?Date=06/21/2009`.

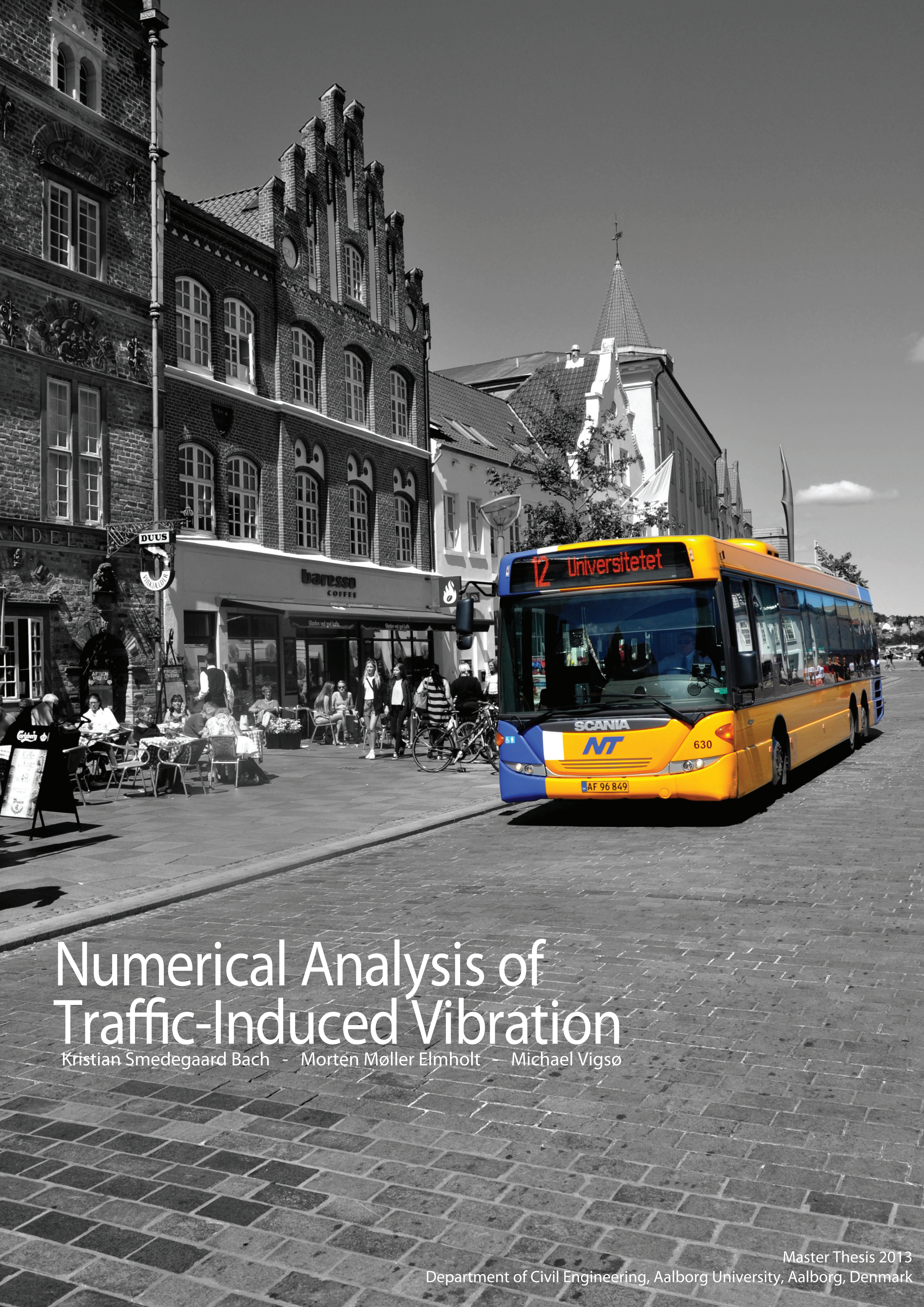

Numerical Analysis of Traffic-Induced Vibration

Kristian Smedegaard Bach - Morten Møller Elmholt - Michael Vigsø

Master Thesis 2013
Department of Civil Engineering, Aalborg University, Aalborg, Denmark

Prologue

The following paper serves as a background report for the models and theories that are utilised in the project. The aim is to elaborate methods and assumptions and to validate the individual parts of the finite-element model. The background report shall mainly be considered as an appendix and it may be difficult to identify the common thread throughout the report. The individual chapters are arranged in a more or less chronological order but some exceptions must be expected.

.

"Mama always said life was like a box of chocolates.
You never know what you're gonna get."

\- Forrest Gump

Contents

Prologue **iii**

1 Vehicle model **1**
- 1.1 System Model 1
- 1.2 System Matrices 2
- 1.3 Vehicle Vibrations 4
- 1.4 Simulation 5

2 Vehicle-Soil Interaction **7**
- 2.1 Road Surface model 7
- 2.2 Bernoulli Euler Beam 8
- 2.3 Vehicle-Beam Interaction 13
- 2.4 Vehicle-Soil Interaction 17

3 Soil-Building Interaction **21**
- 3.1 Natural Frequencies of the Building 21
- 3.2 Vibrations due to Movable Supports 24
- 3.3 Example of Soil-Building interaction 25

4 2D elements **29**
- 4.1 Element Testing 29
- 4.2 Static deformation 30
- 4.3 Eigenfrequencies 30
- 4.4 Comparison with Plaxis 32

5 Transmitting Boundary Conditions **37**
- 5.1 Impedance Boundary Conditions 37
- 5.2 Implementation in FEM 38
- 5.3 Verification 40
- 5.4 Soil layering 42

6 Frequency Domain Solution **45**
- 6.1 Simply supported beam 45
- 6.2 Plane elements 47

7 Road Elements **49**
- 7.1 The Kelvin Model 49
- 7.2 Numerical Kelvin model 51
- 7.3 Model validation 52
- 7.4 Interface elements 54
- 7.5 Element validation 55

7.6 Mindlin elements 57
7.7 Element validation 58

8 3D model **61**
8.1 Three-dimensional continuum elements 61
8.2 Path test 62
8.3 Convergence 63
8.4 Construction of Global 3D FE model 66
8.5 Transmitting Boundary Conditions 68

9 Evaluation of Vibrations **69**
9.1 Frequency Weighting 69
9.2 Frequency Bands 71
9.3 Maximum Transient Vibration Value 72

Bibliography **75**

CHAPTER 1

Vehicle model

A key aspect of the project is to set up a model for the vehicle which due to track irregularities will induce dynamic loads to the soil beneath. The following chapter describes how the vehicle is modelled as a multi-degree-of-freedom (MDOF) system and contains explanations of relevant theory and assumptions.

1.1 System Model

Vehicles causing problems due to vibrations are usually heavy vehicles such as a bus illustrated in Figure 1.1.

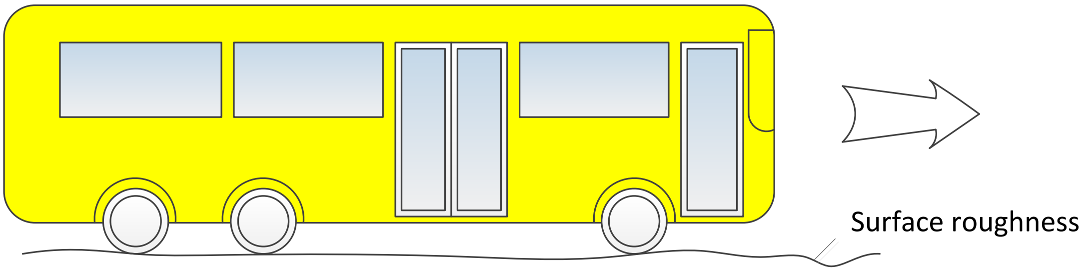

Figure 1.1. Illustration of a typical city bus.

The vehicle is modelled as a MDOF system with inspiration from [Henchi et al., 1997] and [Kima et al., 2005]. The load from the vehicle shell including interior and passengers is supported by sets of springs and dampers (suspension systems) connected to the axels. Due to compressibility of the air inflated tyres the wheels are modelled with a set of springs and dampers as well, see Figure 1.2.

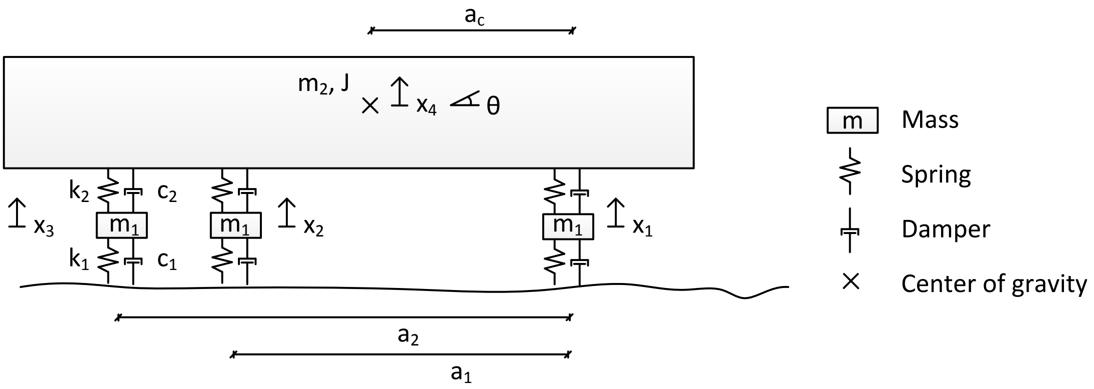

Figure 1.2. Dynamic model of the city bus.

Some assumptions are made when establishing the dynamic model:

- The problem is simplified to a two dimensional problem.
- The shell of the vehicle is assumed to be rigid.
- Horizontal effects are neglected.
- The stiffness and damping is the same for all tyres and for all suspension systems.
- Dampers and springs are assumed to behave linearly.

In the following sections the three axel system above will be used as a case study, however, the program is configurated to work for more than three axels. In addition to the geometrical values presented in Figure 1.2 the following are used:

$$\mathbf{a} = \begin{bmatrix} 0 \\ a_1 \\ a_2 \end{bmatrix} \qquad \mathbf{b} = \begin{bmatrix} a(2) - a(1) \\ a(3) - a(2) \end{bmatrix} \qquad \mathbf{c} = a_c - \mathbf{a} \tag{1.1}$$

1.2 System Matrices

The system in Figure 1.2 have five degrees of freedom, one for each axel and two for vertical movement and rotation of the vehicle shell. The mass matrix is given as:

$$\mathbf{M} = \begin{bmatrix} m_1 & 0 & 0 & 0 & 0 \\ 0 & m_1 & 0 & 0 & 0 \\ 0 & 0 & m_1 & 0 & 0 \\ 0 & 0 & 0 & m_2 & 0 \\ 0 & 0 & 0 & 0 & J \end{bmatrix} \tag{1.2}$$

The stiffness matrix is derived by applying a unit displacement in each degree of freedom and calculate the force response. The procedure is illustrated in Figure 1.3 for a unit displacement in the first degree of freedom.

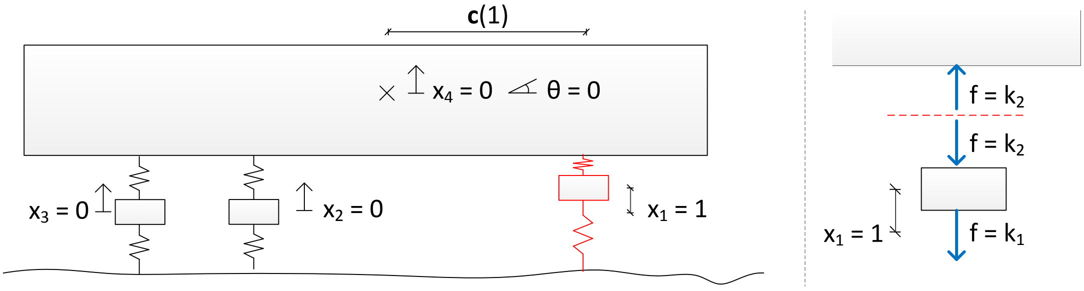

Figure 1.3. Method to derive the stiffness matrix.

The stiffness matrix is given as:

$$\mathbf{K} = \begin{bmatrix} k_1 + k_2 & 0 & 0 & -k_2 & k_2 \cdot \mathbf{c}(1) \\ 0 & k_1 + k_2 & 0 & -k_2 & k_2 \cdot \mathbf{c}(2) \\ 0 & 0 & k_1 + k_2 & -k_2 & k_2 \cdot \mathbf{c}(3) \\ -k_2 & -k_2 & -k_2 & 3 \cdot k_2 & \sum_{i=1}^{3} -k_2 \cdot \mathbf{c}(i) \\ k_2 \cdot \mathbf{c}(1) & k_2 \cdot \mathbf{c}(2) & k_2 \cdot \mathbf{c}(3) & \sum_{i=1}^{3} -k_2 \cdot \mathbf{c}(i) & \sum_{i=1}^{3} \mathbf{c}(i) \cdot k_2 \cdot \mathbf{c}(i) \end{bmatrix} \tag{1.3}$$

Notice that the matrix is symmetric and it can be shown, that it is positive definite as well. The stiffness matrix above reveals a certain pattern and it is quite simple to set up a general description that is valid for any number of axels. The eigenmodes of the system is calculated based on **M** and **K** and if realistic values of stiffness, mass and axel distance is used the first three modes will typically look as illustrated in Figure 1.4.

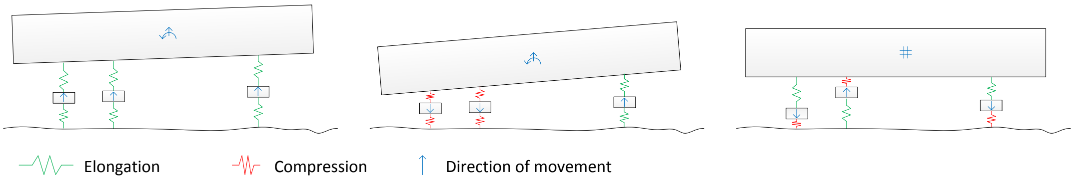

Figure 1.4. Typical mode shapes for mode 1, 2 and 3.

The vehicle is assumed to be critically damped in the first mode based on experience. Stiffness proportional damping is assumed and the damping matrix can hereby by expressed as:

$$\mathbf{C} = a_1 \ \mathbf{K} \tag{1.4}$$

The coefficient a_1 above should not be confused with the geometrical value from Figure 1.2. According to [Nielsen, 2004] the coefficient a_1 can be related to the modal damping ratio of the first mode ξ_1 using:

$$a_1 = \frac{2 \cdot \xi_1}{\omega_1} \tag{1.5}$$

1.3 Vehicle Vibrations

Vibrations of the vehicle are induced by the rough surface which will cause the surface of the tyre to move vertically as the vehicle crosses. It is assumed that the bottom of the tyre will always be connected to the road surface, corresponding to a vertical movement at the bottom of the lower springs in Figure 1.2. The problem is treated in [Nielsen, 2004] where the following equation of motion is derived:

$$\mathbf{M}\ddot{\mathbf{x}} + \mathbf{C}\dot{\mathbf{x}} + \mathbf{K}\mathbf{x} = \mathbf{C}\dot{\mathbf{x}}^{(0)}(t) + \mathbf{K}\mathbf{x}^{(0)}(t) \tag{1.6}$$

The expression on the right of the equation denotes the force induced by movable supports. $\mathbf{x}^{(0)}(t)$ refer to the quasi static deformation due to the movable support and can be expressed as:

$$\mathbf{x}^{(0)}(t) = \mathbf{U}\mathbf{y}(t) \tag{1.7}$$

$\mathbf{y}(t)$ describes the movement of a given support in time and $\mathbf{U}$ is a vector indicating the quasi-static motion from a unit deformation of the associated support. $\mathbf{U}$ is set up by applying a unit deformation at the relevant support whereafter the response is derived using vertical force and moment equilibrium and geometrical conditions. The procedure is illustrated in T Figure 1.5 for a unit deformation of the first support.

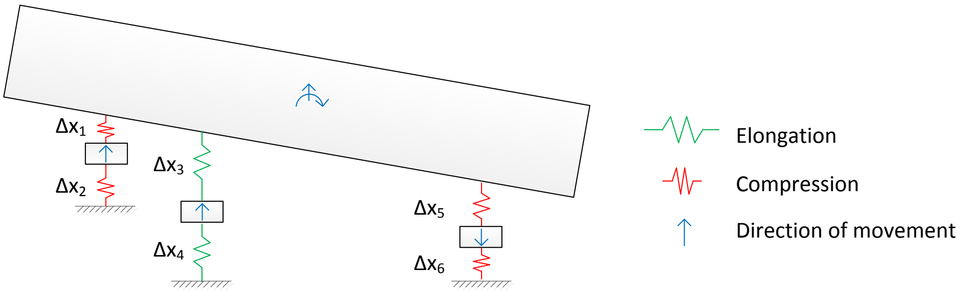

Figure 1.5. Procedure for derivation of the **U**-matrix.

The derivation is found to be easier if the compression of the spring Δx_i is considered. The following equations are set up:

$$\Delta x_{i\cdot 2} \cdot k_1 - \Delta x_{i\cdot 2-1} \cdot k_2 = 0 \qquad \text{for} \qquad i = 1,2,3 \tag{1.8}$$

$$\sum_{i=1}^{3} \Delta x_{i\cdot 2-1} \cdot k_2 = 0 \tag{1.9}$$

$$\sum_{i=1}^{3} \Delta x_{i\cdot 2-1} \cdot k_2 \cdot \mathbf{c}(i) = 0 \tag{1.10}$$

$$\frac{(1 - \Delta x_1 - \Delta x_2) - (-\Delta x_3 - \Delta x_3)}{\mathbf{b}(1)} = \frac{(-\Delta x_3 - \Delta x_4) - (-\Delta x_5 - \Delta x_6)}{\mathbf{b}(2)} \tag{1.11}$$

The last equation is a geometrical condition from the rigid rotation of the bus shell. This condition is the only one that changes when a unit displacement of the second support is applied. By studying the equations above, general expressions can be derived for an arbitrary number of axels. In practical the equations are set up on matrix form and solved by row-reduction. The values of Δx_i are used to calculate the **U**-matrix.

1.4 Simulation

The vehicle is assumed to cross a rough surface described by the curve $y(s)$. In this example the curve is assumed to be sinusoidal with the following values:

$$y(s) = A \ \sin\left(2 \ \pi \ \frac{s}{L}\right) \tag{1.12}$$

A	Road amplitude
L	Sinusoidal wave period
s	Position

The position s can be calculated from the vehicle speed v and the time t. The vibrations of the vehicle are calculated by subjecting the surface displacement $y(t)$ to each axel with a time difference determined from the internal axel distance, **b**. In Figure 1.6 the results for movement of the first degree of freedom is given along with the surface profile.

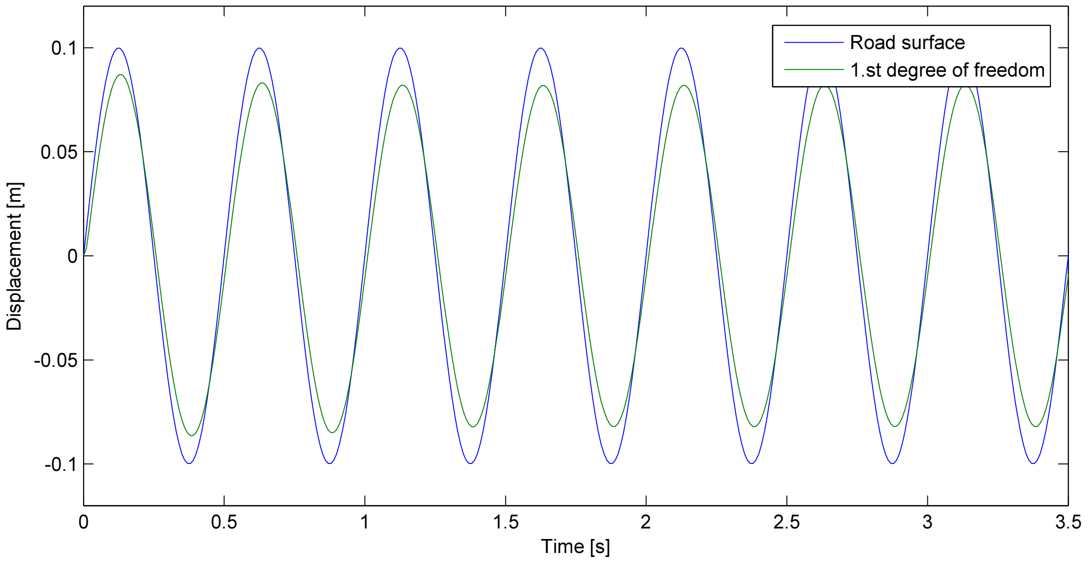

Figure 1.6. Results from simulation on sinusoidal road.

As illustrated the movement of the axel is closely related to the shape of the surface with a minor phase shift. The difference between the surface shape and the movement of the axel is used to calculate the compression of the lower spring (the tyre) and from the compression and the rate of compressibility the force on the track due to surface roughness can be calculated.

Chapter 2

Vehicle-Soil Interaction

In this chapter the vehicle model from Chapter 1 on page 1 is set to interact with the road and surface irregularities. Initially a simple method for modelling the contact surface between tyre and road is presented. Next two integration schemes for modelling the interaction between vehicle and road is explained. Finally the effect of interaction is evaluated using simulations.

2.1 Road Surface model

The surface profile described in Equation (1.12) is unlikely in reality. In the three articles, cobblestone pavements and speed bumps are constructed according to Sterner [2009]. Three different types of speed bumps, a circle bump, a sinus bump and a trapeze bump are set up. Common for all the surface profiles is that they are described at discrete points with steps of ds in order to fit the velocity of the vehicle:

$$ds = v_{veh}\ dt \tag{2.1}$$

In order to account for the contact surface w between the wheel and the road, a moving average filter is applied to the initial discrete surface irregularities or speed bump elevation as illustrated in Figure 2.1.

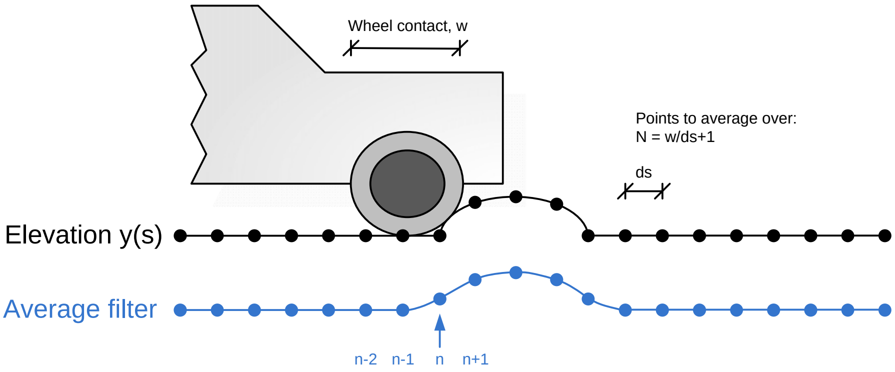

Figure 2.1. Moving average filter to account for wheel contact on speed bumps.

The initial time series for the surface elevation is averaged as illustrated in Figure 2.1

using the moving average filter in Equation (2.2).

$$y(n) = \frac{1}{N}x(n+1) + \frac{1}{N}x(n) + \frac{1}{N}x(n-1) + \frac{1}{N}x(n-2) \tag{2.2}$$

The effect of the average filter is illustrated in Figure 2.2 where a two-wheeled car crosses a circle speed bump at rated speed of 40 km/h. In this case, the vertical acceleration felt by the car should be in the order of 0.65-0.75 g. It is seen that it is possible to adjust the vertical acceleration felt by the car by passing the speed bump to the expected range by increasing w.

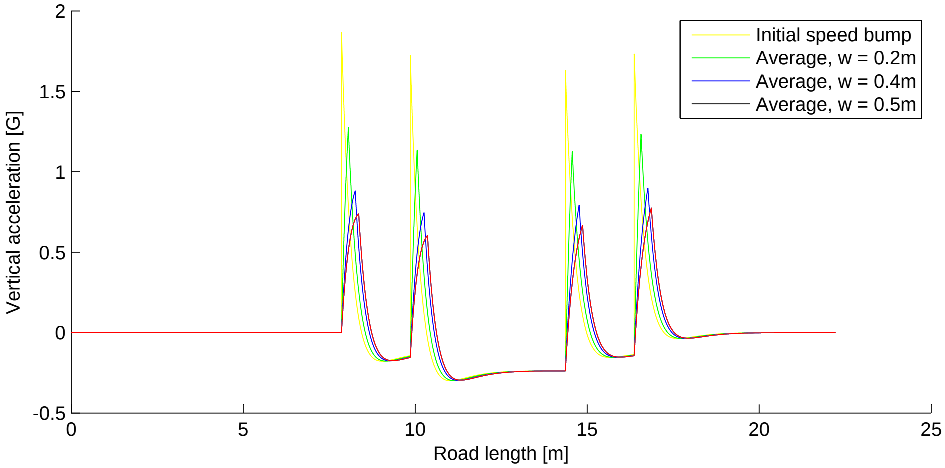

Figure 2.2. Two-wheeled car passage of circle speed bump at rated speed of 40 km/h.

It should be noticed that w is another parameter that should be chosen along with realistic mass, spring stiffness and damping of tyre and suspension in order to get realistic results.

2.2 Bernoulli Euler Beam

The step length ds will typically be relatively small due to the size of the time step dt. The computational cost will be comprehensive if beams are applied for every step. Instead, interpolation is used to estimate nodal forces and nodal displacements for forces applied between nodes. The procedure will be described for the Bernoulli Euler beam element. The element has two nodes, with one rotational degree-of-freedom (dof) and one translational dof in each node as illustrated in Figure 2.3.

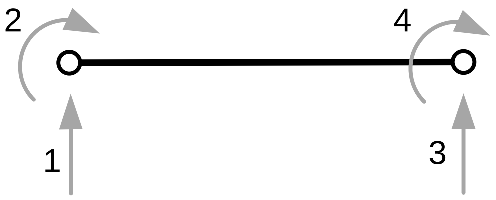

Figure 2.3. Bernoulli Euler beam element with 4 dof.

The Bernoulli Euler beam element uses the following cubic shape functions to interpolate nodal displacement according to Cook et al. [2002].

$$\mathbf{N} = \begin{bmatrix} 1 - \frac{3x^2}{L^2} + \frac{2x^3}{L^3} & x - \frac{2x^2}{L} + \frac{x^3}{L^2} & \frac{3x^2}{L^2} - \frac{2x^3}{L^3} & -\frac{x^2}{L} + \frac{x^3}{L^2} \end{bmatrix} \tag{2.3}$$

The strain interpolation matrix **B** is found as the second derivative of the shape functions **N**:

$$\mathbf{B} = \frac{d^2}{dx^2}\mathbf{N} \begin{bmatrix} -\frac{6}{L^2} + \frac{12}{L^3} & -\frac{4}{L} + \frac{6}{L^2} & \frac{6}{L^2} - \frac{12}{L^3} & -\frac{2}{L} + \frac{6}{L^2} \end{bmatrix} \tag{2.4}$$

2.2.1 System matrices

The system matrices for the beam element are given in the following based on Cook et al. [2002].

The stiffness matrix is given as:

$$\mathbf{K} = \int_0^L \mathbf{B}^T EI\mathbf{B}\, dx = EI \begin{bmatrix} \frac{12}{L^3} & \frac{6}{L^2} & -\frac{12}{L^3} & \frac{6}{L^2} \\ \frac{6}{L^2} & \frac{4}{L} & -\frac{6}{L^2} & \frac{2}{L} \\ -\frac{12}{L^3} & -\frac{6}{L^2} & \frac{12}{L^3} & -\frac{6}{L^2} \\ \frac{6}{L^2} & \frac{2}{L} & -\frac{6}{L^2} & \frac{4}{L} \end{bmatrix} \tag{2.5}$$

The mass matrix is given as:

$$\mathbf{M} = \int_0^L \mathbf{N}^T \rho A\mathbf{N}\, dx = \frac{\rho AL}{420} \begin{bmatrix} 156 & 22L & 54 & -13L \\ 22L & 4L^2 & 13L & -3L^2 \\ 54 & 13L & 156 & -22L \\ -13L & -3L^2 & -22L & 4L^2 \end{bmatrix} \tag{2.6}$$

The damping matrix can be calculated from the stiffness and mass matrix using a Rayleigh damping model as given in formula 2.7.

$$\mathbf{C} = \alpha\mathbf{M} + \beta\mathbf{K} \tag{2.7}$$

The coefficients α and β in Equation (2.7) are linked to the damping ratio ξ by Equation (2.8).

$$\alpha + \beta\omega_i^2 = 2\omega_i\xi_i \tag{2.8}$$

It is possible to adjust the coefficients α and β to fit two specific modes of interest exactly, or just to fit the damping ratio ξ for a single mode as done in Equation (1.5).

2.2.2 Interpolation

In order to demonstrate the principle of interpolation, an example with a simply supported beam with two elements is conducted. The situation is illustrated in Figure 2.4.

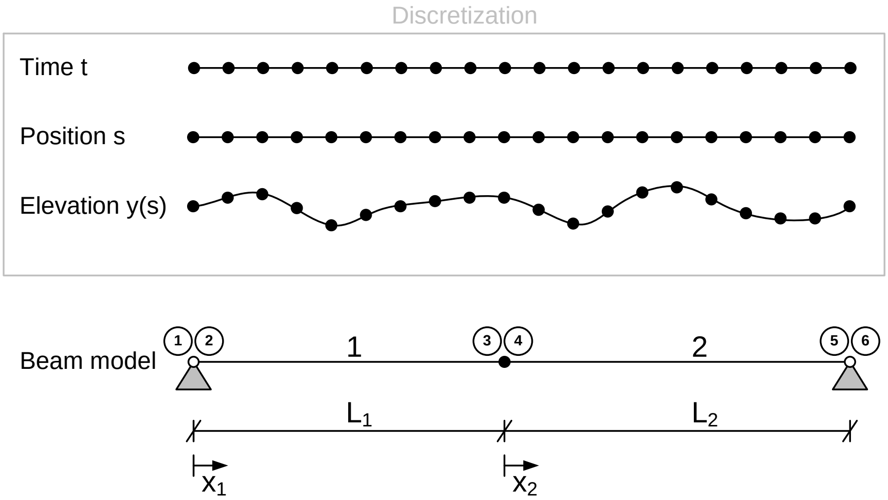

Figure 2.4. Discretisation of time and surface roughness for vehicle and for beam model.

The geometric and material properties for the current example are listed below:

- Load at mid point, p = -1 kN
- Beam length, $L = 1$ m
- Beam height, $h = 0.1$ m
- Beam width, $b = 0.1$ m
- Young's Modulus, $E = 210$ GPa

The static system response $\mathbf{u}$ for the example with 2 elements and a point force at the mid node is given by:

$$\mathbf{u}^T = \begin{bmatrix} 0 & -0.0036 & -0.0119 & 0 & 0 & 0.0036 \end{bmatrix} \tag{2.9}$$

The interpolated response at global discretisation s_i for the current example is given by Equation (2.10) and is shown on the blue curve in Figure 2.5.

$$\mathbf{u}(s_i) = \begin{cases} \mathbf{N}_{x1(s_i),L_1} \cdot \mathbf{u}([1\ 2\ 3\ 4]) & \text{for element 1} \\ \mathbf{N}_{x2(s_i),L_2} \cdot \mathbf{u}([3\ 4\ 5\ 6]) & \text{for element 2} \end{cases} \tag{2.10}$$

It is also possible to interpolate the point load p at discretisation s_i, to the corresponding beam nodes. This is done for the same beam with just one beam element by Equation (2.11) and the results is shown with the red curve in Figure 2.5.

$$\mathbf{f}([1\ 2\ 3\ 4]) = \mathbf{N}_{x1(s_i),L_1} \cdot p(s_i) \quad \text{for element 1} \tag{2.11}$$

The results for the static interpolated deflection from Formula (2.10) is shown in Figure 2.5 with the blue curve and it gives the exact results compared with the analytical solution for a simply supported Bernoulli Euler beam with a point load at the middle. The red curve shows the deflection for only one beam element, where the point load at the middle is interpolated to the end nodes. This gives the exact deflection/rotation at the end nodes, but underestimates the maximum deflection at the middle of the beam when the deflection **u** is interpolated within the beam.

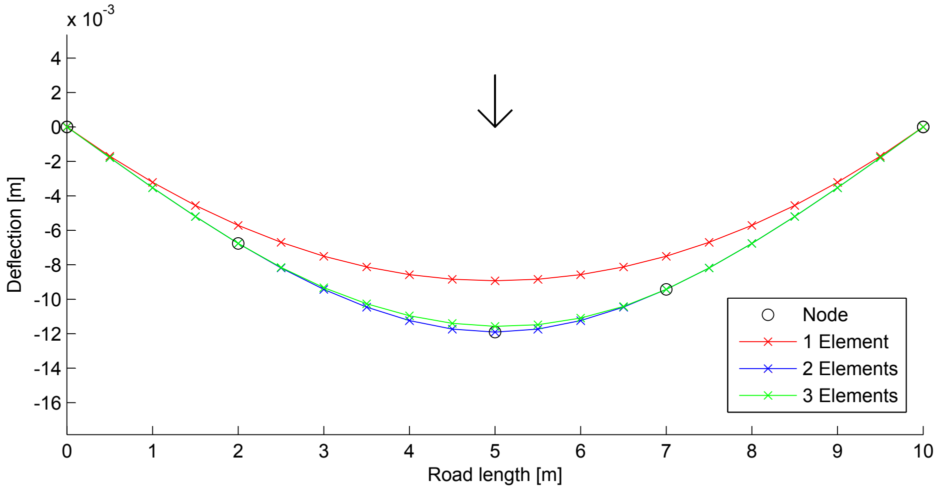

Figure 2.5. Static interpolated deflection.

The green curve shows the deflection, when three beam elements are used with nodes at 0, 2, 7 and 10 m. The point load at the middle is again interpolated to corresponding nodes, and it is seen that the deflection/rotation is exact in the nodes. The interpolated deflection is also exact in the first and third beam element, but the maximum deflection at the middle of the beam is again underestimated. The above examples in Figure 2.5 shows that in order to get the right results of the deformation in a given point of interest, a node should be placed, in the point of interest or a node should be placed where the force is applied.

2.2.3 Eigenfrequency Evaluation

The eigenfrequencies from the FE beam model are calculated by solving the eigenvalue problem given by formula (2.12). The system matrices SysK and SysM are the reduced system matrices, where the fixed dof at the boundaries have been removed.

$$\left(\mathbf{K} - \omega^2\,\mathbf{M}\right)\ \Phi = 0 \tag{2.12}$$

For a simply supported beam with two elements, this gives four dof, which makes it possible to find four eigenfrequencies and four related eigenmodes. In Figure 2.6 the four modeshapes are plotted using shape functions.

The eigenfrequencies for different numbers of elements for the simply supported beam are shown in Table 2.1 along with the analytical results for the first five eigenfrequencies. As expected, it is seen that the first half of the frequencies corresponds well to the analytical results.

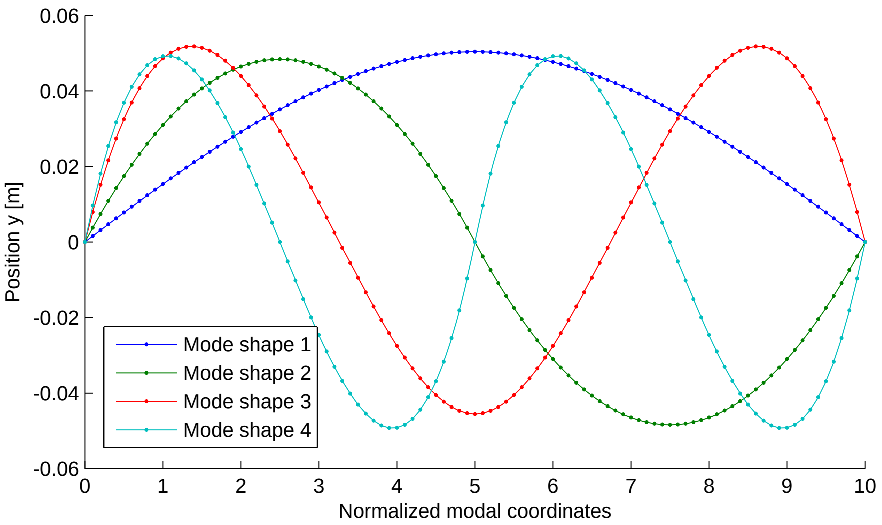

Figure 2.6. Beam modeshapes for simply supported beam with two elements.

Elements	1	2	3	4	5	Analytic
f_1 [Hz]	2.58	2.34	2.33	2.32	2.32	2.32
f_2 [Hz]	11.82	10.48	9.36	9.33	9.32	9.30
f_3 [Hz]		25.18	23.50	21.29	21.14	20.93
f_4 [Hz]		47.26	42.77	41.26	39.39	37.19
f_5 [Hz]			110.93	65.58	62.31	58.14

Table 2.1. Eigenfrequencies for simply supported beam for different element numbers.

Another way to illustrate the effect of the number of beam elements is to let the simply supported beam vibrate freely. The problem is solved in the time domain by time integration using the Newmark algorithm. A Fourier transformation of the results shows the power spectrum density in Figure 2.7. The shape functions are again used to interpolate both loads and the response used for the Fourier transformation.

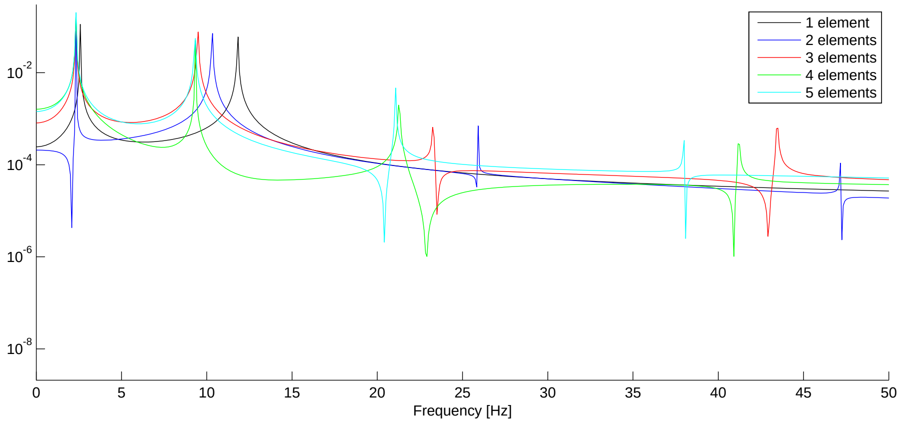

Figure 2.7. Frequency spectrum for different number of elements.

It is evident, as shown in Table 2.1, that by using two elements instead of one, it is possible to find all four eigenfrequencies in the frequency range plotted in Figure 2.7. Adding even more elements moves the peaks in the frequency spectrum closer to the right results, that can be obtained from the analytical solution.

2.3 Vehicle-Beam Interaction

The vehicle model from Chapter 1 is now set to interact with the beam model. Two methods for modelling vehicle-beam interaction are presented in the following section.

2.3.1 Explicit Time Integration

The interaction between the two models (vehicle and beam) is solved in the time domain using the Newmark integration scheme with a time shift of dt between the response of the two models, as illustrated in Figure 2.8.

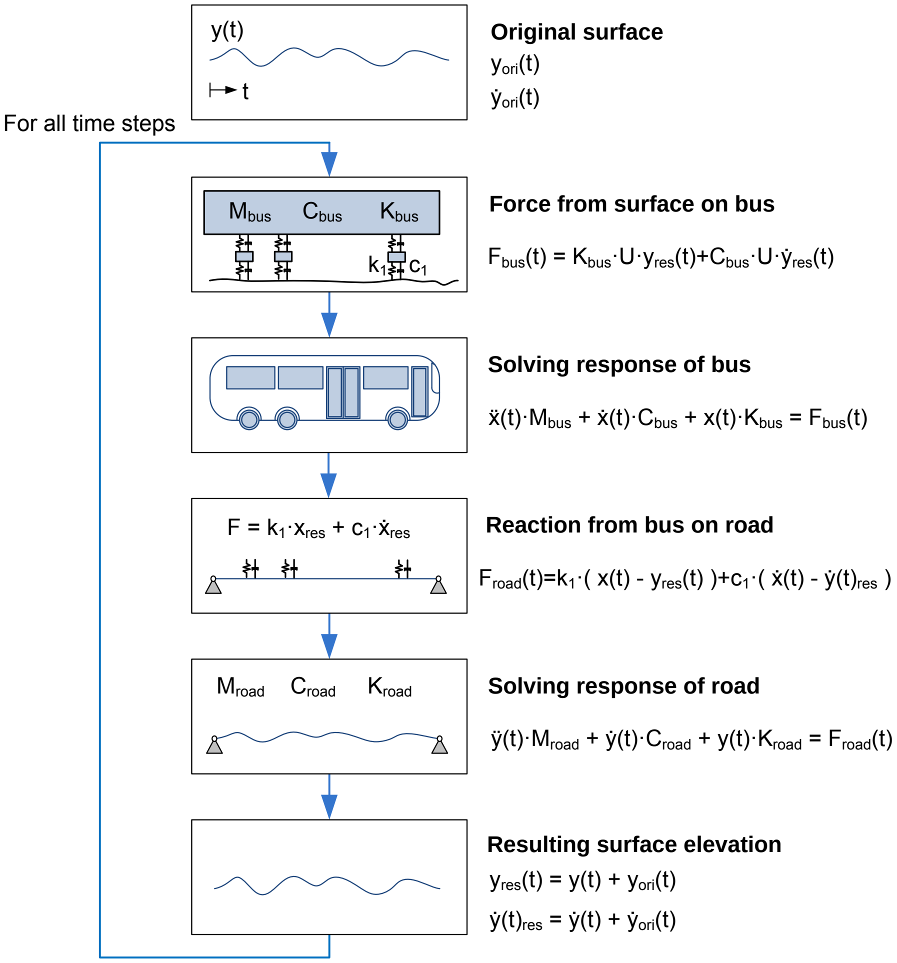

Figure 2.8. Principle for modelling the interaction using an explicit time integration scheme.

The force from the surface irregularities and speed bumps acting on the vehicle can be expressed by Equation (2.13) according to the illustration in Figure 2.8.

$$\mathbf{F}_{bus}(t) = \mathbf{K}_{bus}\ \mathbf{u} \cdot (y_{ori}(t) + y(t - dt)) + \mathbf{C}_{bus}\ \mathbf{u} \cdot (\dot{y}_{ori}(t) + \dot{y}(t - dt)) \tag{2.13}$$

By applying the loads to the vehicle system it is possible to solve the response $x(t)$ for the vehicle for the current time step. The reaction force acting on the beam can now be calculated by Equation (2.14) according to the illustration in Figure 2.8.

$$\mathbf{F}_{road}(t) = k_1 \cdot (x(t) - y_{ori}(t) - y(t - dt)) + c_1 \cdot (\dot{x}(t) - \dot{y}_{ori}(t) - \dot{y}(t - dt)) \tag{2.14}$$

The reaction force $\mathbf{F}_{road}(t)$ is now applied on the beam system and the response $y(t)$ is found. This procedure is continued for all time steps. The procedure described above for solving the interaction between the vehicle and the beam has a time shift of dt between the response of the beam and the vehicle. If the time step is to large or if the stiffness of the beam is to soft, the solution will be inaccurate.

2.3.2 Implicit Time Integration

Another way to solve the interaction problem in the time domain is to use an implicit time integration scheme. In this approach the two systems (vehicle and beam) are collected in a single global system and the interaction forces between the vehicle and the beam are equalized as added stiffness and damping in the global system. In short form the global system is described by:

$$\mathbf{M}\ddot{\mathbf{u}} + (\mathbf{C} + \Delta\mathbf{C})\dot{\mathbf{u}} + (\mathbf{K} + \Delta\mathbf{K})\mathbf{u} = \mathbf{F}(t) \tag{2.15}$$

For a SDOF vehicle system with mass m_1, damping c_1 and stiffness k_1 interacting at a single beam element with shape functions $\mathbf{N}$, the global system matrices can be reduced to:

For the global mass matrix:

$$\mathbf{M} = \begin{bmatrix} \begin{bmatrix} \mathbf{M}_b \end{bmatrix} & \mathbf{0} \\ \mathbf{0} & m_1 \end{bmatrix} \tag{2.16}$$

For the global damping matrix:

$$\mathbf{C} = \begin{bmatrix} \begin{bmatrix} \mathbf{C}_b \end{bmatrix} & \mathbf{0} \\ \mathbf{0} & c_1 \end{bmatrix} + \begin{bmatrix} \mathbf{N}^T c_1 \mathbf{N} & -\mathbf{N}^T c_1 \\ -\mathbf{N} c_1 & \mathbf{0} \end{bmatrix} \tag{2.17}$$

For the global stiffness matrix:

$$\mathbf{K} = \begin{bmatrix} \begin{bmatrix} \mathbf{K}_b \end{bmatrix} & \mathbf{0} \\ \mathbf{0} & k_1 \end{bmatrix} + \begin{bmatrix} \mathbf{N}^T k_1 \mathbf{N} & -\mathbf{N}^T k_1 \\ -\mathbf{N} k_1 & \mathbf{0} \end{bmatrix} \tag{2.18}$$

The corresponding force vector:

$$\mathbf{F}(t) = \begin{bmatrix} -\mathbf{N}^T \left(k_1 \cdot y(t) + c_1 \cdot \dot{y}(t)\right) \\ k_1 \cdot y(t) + c_1 \cdot \dot{y}(t) \end{bmatrix} \tag{2.19}$$

In the general case with i beam elements and a vehicle model as described in Chapter 1 with j axels it is more complicated, but the overall structure is the same. The stiffness matrix will in general be:

$$\mathbf{K} = \begin{bmatrix} \begin{bmatrix} \mathbf{K}_b \end{bmatrix} & \mathbf{0} \\ \mathbf{0} & \begin{bmatrix} \mathbf{K}_v \end{bmatrix} \end{bmatrix} + \begin{bmatrix} \mathbf{N}^T k_1 \mathbf{N} & -\mathbf{N}^T k_1 \\ -\mathbf{N} k_1 & \mathbf{0} \end{bmatrix} \tag{2.20}$$

The additional stiffness have to be added for every axel with different shape functions corresponding to the actual position of the wheels in the beam element. The structure of the damping matrix is the same as for the stiffness in Equation (2.20), while the force vector becomes:

$$\mathbf{F}(t) = \begin{bmatrix} -\mathbf{N}^T \left(k_1 \cdot y(t) + c_1 \cdot \dot{y}(t)\right) \\ \mathbf{K}_v \mathbf{u} \mathbf{y}(t) + \mathbf{C}_v \mathbf{u} \dot{\mathbf{y}}(t) \end{bmatrix} \tag{2.21}$$

2.3.3 Test of Vehicle-Beam Interaction

In order to test the two methods for solving the interaction between the vehicle and the beam in the time domain, the following setup is considered. The vehicle is modelled with three axels (0 m, 2 m, 3 m) and is driving with a velocity of 10 m/s across a simply supported beam with a length of 10 m. The surface of the beam consists of a sinus bump designed for nominal speed of approximately 5 m/s. The material properties of the vehicle and the beam are chosen in order to make the response of the beam in the same order as the elevation of the speed bump. In this way the interaction effects between the vehicle and the beam should be significant.

In Figure 2.9 the response of the beam and the vehicle wheels are shown for both integration methods, without interaction, meaning that the vehicle affects the beam, but the resulting response of the beam is not affecting the vehicle. In this way it is only the original surface elevation, in this case the sinus bump, that affects the vehicle.

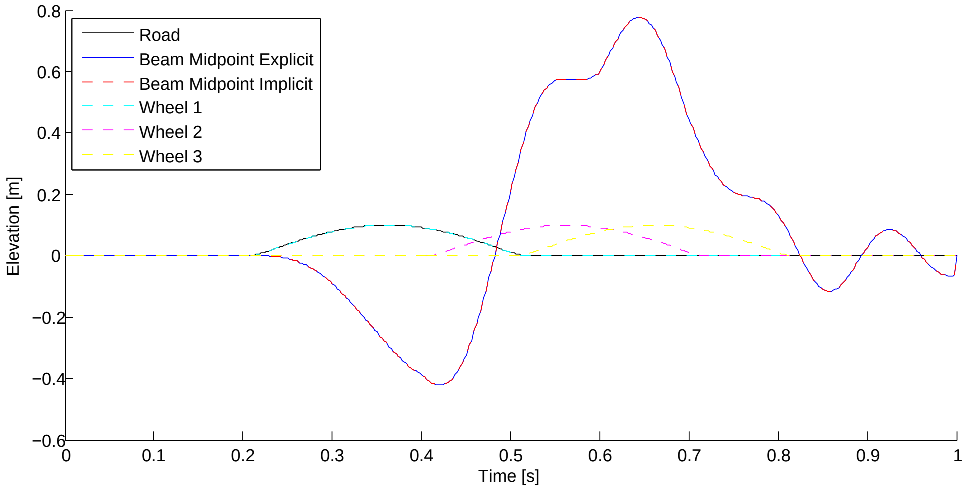

Figure 2.9. Three-wheeled vehicle passing speed bump without interaction.

It is seen in Figure 2.9, that the two methods for solving the problem give exactly the same results, when interactions effects are not considered. It is also clear that only the original surface elevation affect the response of the vehicle wheels.

In Figure 2.10 the same situation is shown where interaction effects are taken into account. The results are only shown for the implicit integration method, because in this case, the explicit method explodes due to either to large time step or to soft material properties of the beam.

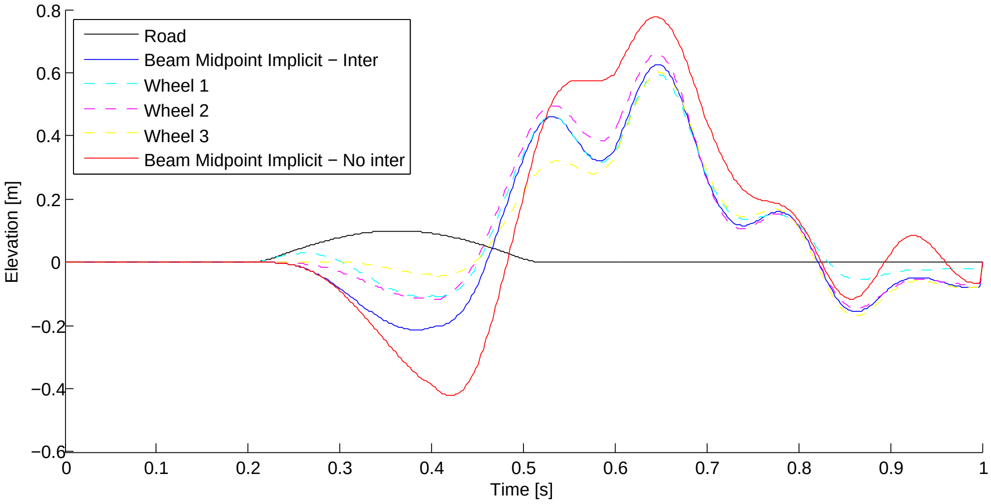

Figure 2.10. Three-wheeled vehicle passing speed bump with interaction.

The response of the beam at the midpoint (blue) is compared with the similar response without interaction (red) and it is seen that the vehicle acts as a kind of damper on the beam, when interaction is taken into account, which in this case makes the maximum deflection slightly smaller. The response of the beam along with the original surface elevation correspond also well to the first wheel for the first half of the time series and to the second and third wheels for the second half of the time series, as expected because the beam response is evaluated at the midpoint.

2.4 Vehicle-Soil Interaction

After validating the different interaction algorithms, the beam elements in the above section are now replaced with road elements supported by a soil body. The scope of the following study is to investigate the influence of interaction effects for a road supported by soil. A reference case, illustrated in Figure 2.11, is used with a three-axle bus passing a sinusoidal surface elevation with wavelength of 1 m. The surface roughness height is initially set to 0.1 m corresponding to the road hump height, and afterwards to 0.01 m corresponding to the approximate height of the cobblestone pavement.

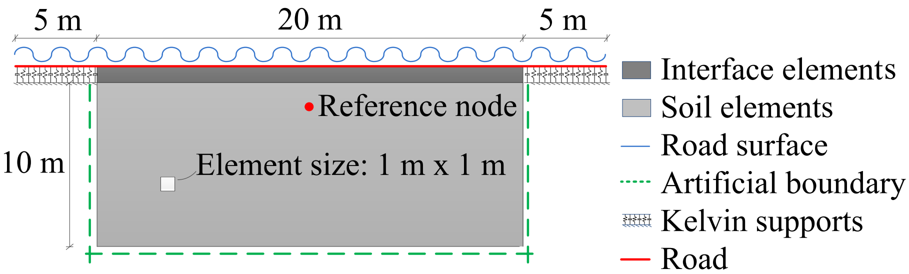

Figure 2.11. Reference case for evaluation of vehicle-soil interaction.

The two different integration schemes in Section 2.3 are compared for different soil types with and without interaction effects included. The results are compared with a simplified model in which the vehicle loads are calculated and applied separately as external forces for the whole time series.

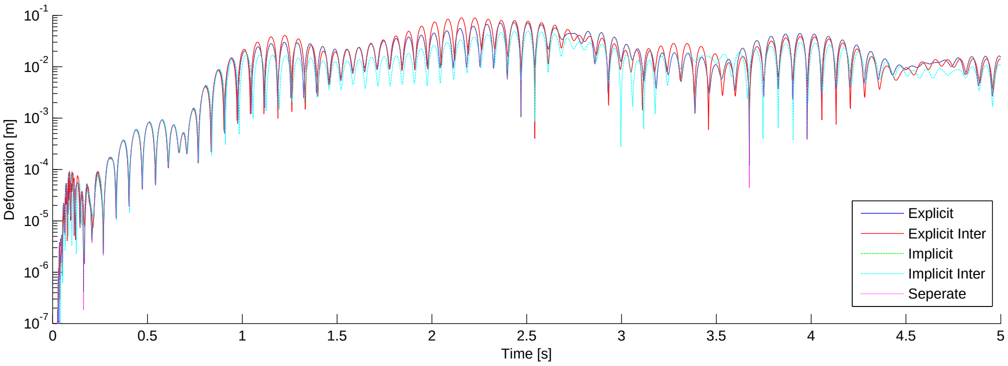

Figure 2.12. Vehicle interaction for soft peat with surface roughness of 0.1m. Note log scale.

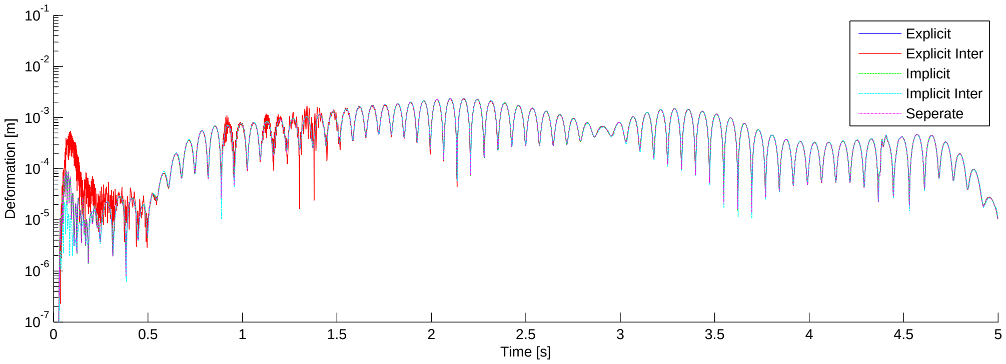

Figure 2.13. Vehicle interaction on clay with surface roughness of 0.1m. Note log scale.

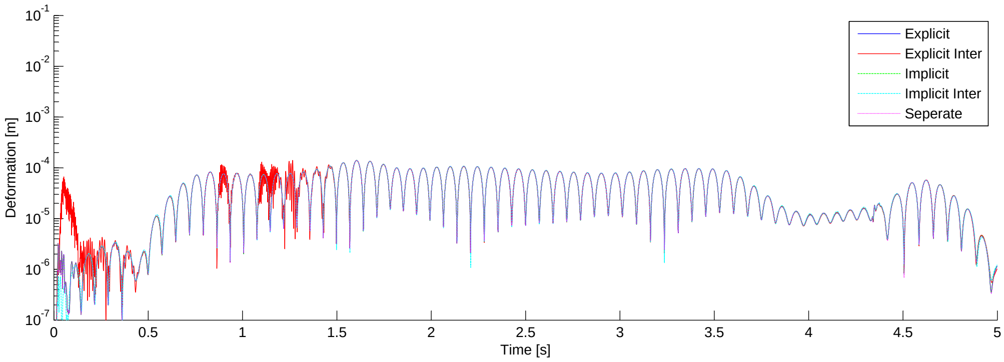

Figure 2.14. Vehicle interaction on limestone with surface roughness of 0.1m. Note log scale.

Figure 2.12 to 2.14 show the displacement on a log scale 2 m below the soil surface at the middle of the model, as function of time for soft peat, clay and limestone, respectively. It is seen in the figures that the explicit and implicit integration schemes give the same response as if the vehicle loads are applied separately. It should also be noted that the response looks very similar for clay and limestone, while some deviation is seen for the soft peat. This indicates that the interaction effects only are important for very soft soil, where the displacement of the soil is relatively large. The deviation in the explicit response with interaction at the beginning is caused by the vehicle wheels when they are passing from the road element into the continuum soil body elements. Figure 2.15 show the coherence between the stiffness of the soil (Young's Modulus) and the normalized root-mean-square error (NRMSE, see Equation (2.22)) of the displacement for the explicit and the separate method compared to the implicit method. Figure 2.16 shows the coefficient of variation of the RMSE which is calculated from Equation (2.23).

$$\mathrm{NRMSE} = \frac{\mathrm{RMSE}}{Y_{\max} - Y_{\min}} = \frac{1}{Y_{\max} - Y_{\min}} \cdot \sqrt{\frac{1}{n} \sum \left(\hat{Y}_i - Y_i \right)^2} \tag{2.22}$$

$$\mathrm{CV(NRMSE)} = \frac{\mathrm{RMSE}}{\bar{Y}} \tag{2.23}$$

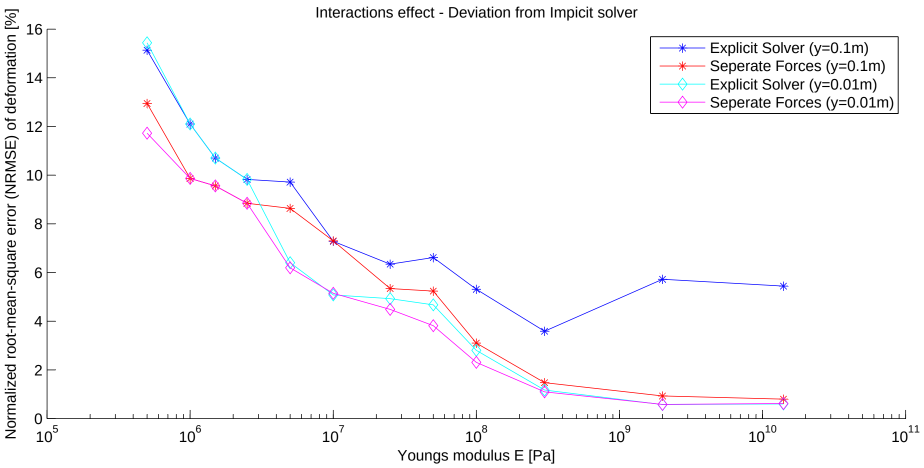

Figure 2.15. NRMSE compared with implicit integration scheme for different roughness.

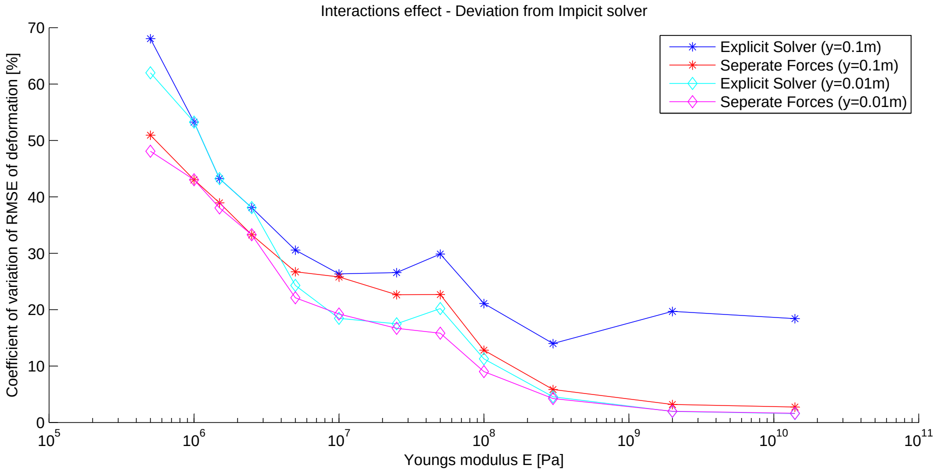

Figure 2.16. Coefficient of variation of the RMSE in Figure 2.15.

Figure 2.15 and 2.16 show the trend that the error decreases with increasing stiffness of the soil, which was also indicated in the Figures 2.12 to 2.14. The NRMSE for dynamic values of Young's Modulus corresponding to real soil types is around 5–7% for soft soil types as peat, while it is around 1–3% for sand and clay and below 1% for limestone and rocky soils. The increase of NRMSE for the explicit solver with roughness of 0.1 m for the stiffer soil is probably due to the fact, that the explicit solver for every time step is alternating around the implicit solution.

It can be concluded that for the reference case with sandy clay and in most other cases with real soil types, and with surface roughness in the order of 1–10 cm, it is valid to use the separate method of applying the vehicle loads to the soil, because the NRMSE is around or below 1%. This is also recommended because of the saving in computational cost, by using the separate method compared with the implicit method.

CHAPTER 3

Soil-Building Interaction

In the total FE model of vehicle, soil body and building, it is possible to model a building with several possible options for both geometry and material properties. The foundation is modelled to follow the surrounding soil body, and in this way transfer the response from the soil to the structure. Another common approach to model vibrations of buildings caused by either traffic induced ground motions or earthquakes is to monitor the displacement and rotation components from either real life measurements on the foundation of a building or to simulate similar response of the ground motions in a FE model. The response of the ground motions is then applied to a FE model of the structure alone, modelled with movable supports as in [Nielsen, 2004].

3.1 Natural Frequencies of the Building

The natural frequency of the building depends on the location of mass and stiffness in the model of the structure. The building in the reference case is supported by a one meter deep foundation, which is connected to the continuum soil body elements. Hereby, the natural response of the building depends on the stiffness of the soil body as well, because the soil stiffness determines the degree of clamping in the foundation of the building.

The material properties of the soil are calibrated according to real values of weight and to fit approximate speeds of P- and S-waves in clay and sandy soil. The material properties for the building is calibrated to fit a typically two storey concrete structure, where the stiffness is adjusted to fit the range of typical eigenfrequencies illustrated in Figure 3.1 by [Andersen, 2006].

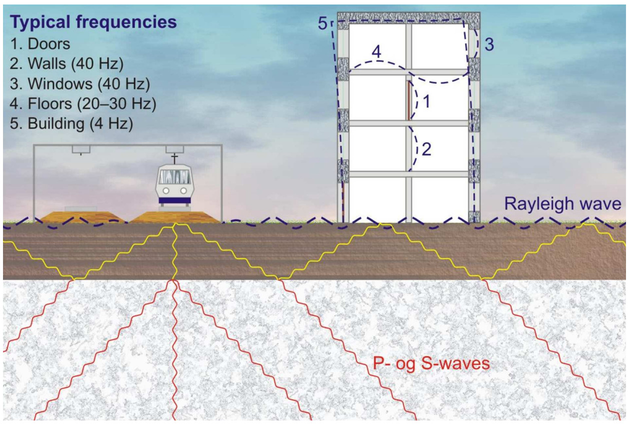

Figure 3.1. Typical eigenfrequencies and eigenmodes for buildings. Andersen [2006]

The eigenmodes and eigenfrequencies are found by solving the general eigenvalue problem as described in (4.8 on page 30), using the system matrices in the FE model. Because of the complexity of the total FE model, three cases are set up with different assumptions for the supports of the building as illustrated in Figure 3.2. The eigenfrequencies of the total model is then chosen based on a comparison with the model of only the building and foundation. The corresponding first four eigenmodes for the three different models are shown in Figures 3.3 to 3.6.

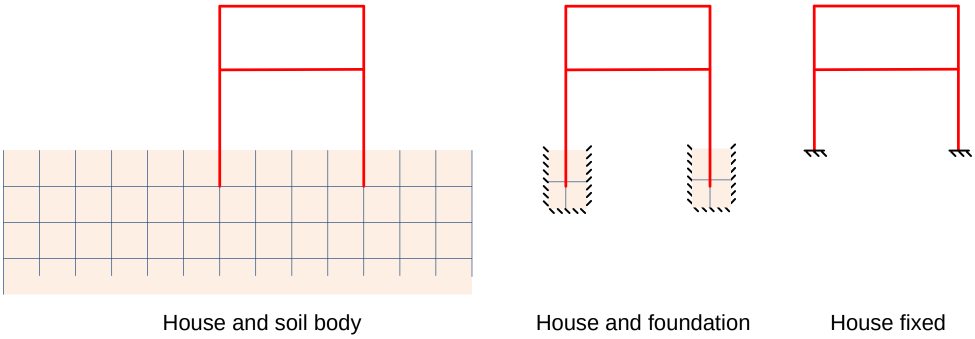

Figure 3.2. Support cases for building, when calculating eigenfrequencies.

The corresponding eigenfrequencies for the first six modes of the building are listed in Table 3.1, and it is seen that the eigenfrequencies fit well with the typical values illustrated in Figure 3.1 for the first modes.

	Mode	House and soil body	House and foundation	House fixed supports
f_1	Building 1	4.1 Hz	4.5 Hz	5.7 Hz
f_2	Roof 1	13.3 Hz	13.6 Hz	13.8 Hz
f_3	Floor 1	12.7 Hz	15.4 Hz	16.0 Hz
f_4	Building 2	16.7 Hz	17.3 Hz	20.7 Hz
f_5	Roof-floor 2	33.6 Hz	37.2 Hz	40.5 Hz
f_6	Roof-floor 2	40.1 Hz	39.5 Hz	44.5 Hz

Table 3.1. Eigenfrequencies for building for different types of supports.

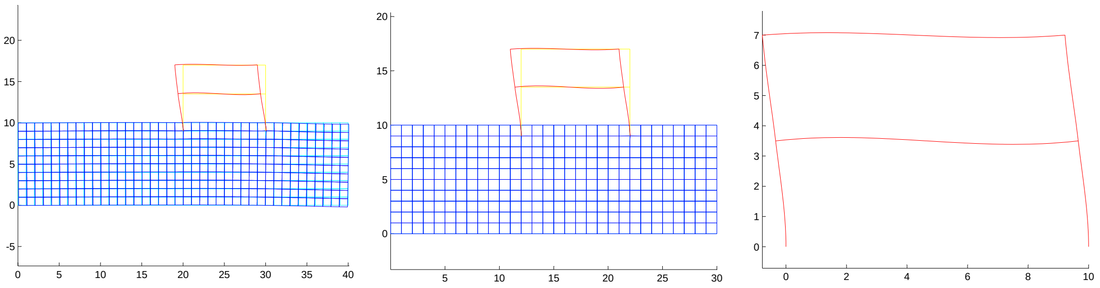

Figure 3.3. First eigenmode of building for different types of supports.

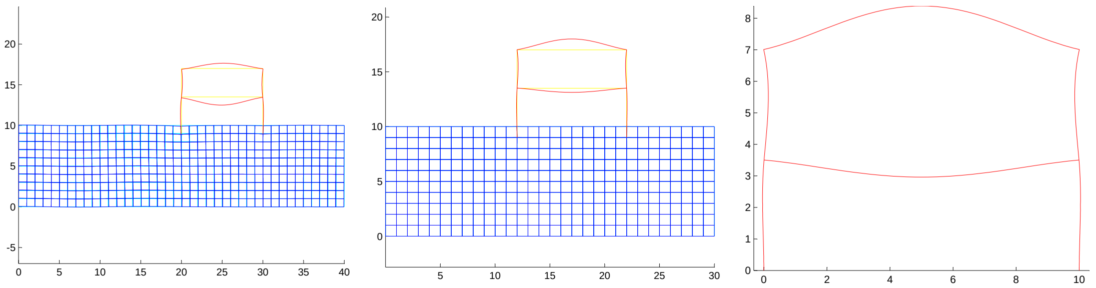

Figure 3.4. Second eigenmode of building for different types of supports.

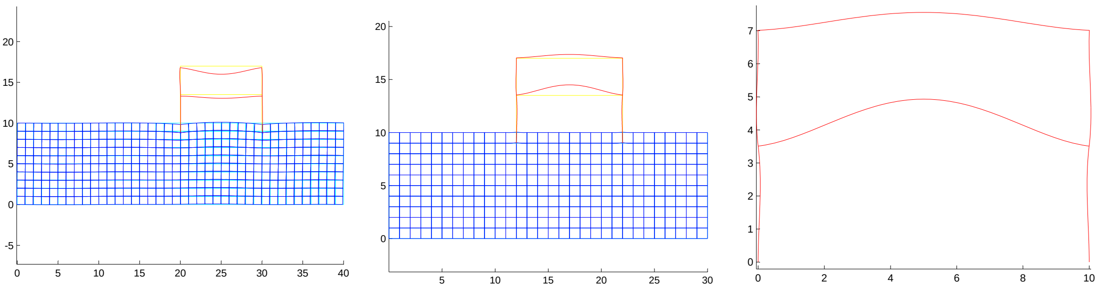

Figure 3.5. Third eigenmode of building for different types of supports.

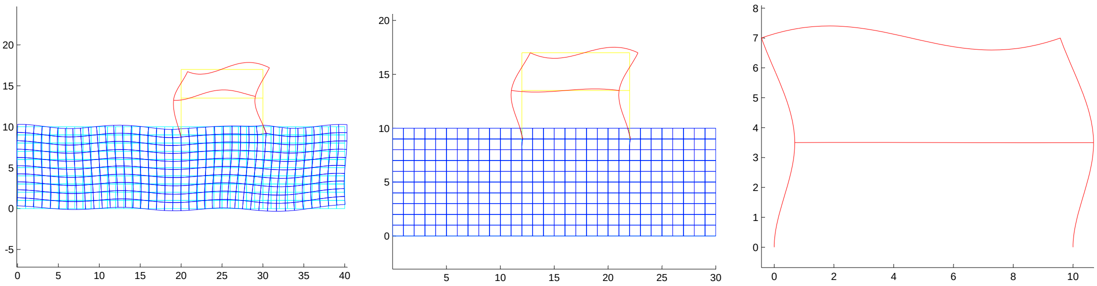

Figure 3.6. Fourth eigenmode of building for different types of supports.

Mode three on Figure 3.1 can be compared with the analytical solution for a fixed beam which has the eigenfrequencies of 18.4 Hz. Due to the fact that mode three of the building with the moving floor is a little more flexible compared to the fixed beam, the eigenfrequency of mode three in the building is smaller compared to the beam.

The results in this section demonstrate that the eigenfrequencies depend on the degree of clamping in the foundation of the building. When the interaction effects are investigated on a building alone with movable supports and compared with the building and soil body it is important to have in mind that the eigenfrequencies will be a little different in the two cases.

3.2 Vibrations due to Movable Supports

An easy and very practical way to model vibration of buildings caused by the dynamic motion of the foundation is to model the building with movable supports according to [Nielsen, 2004]. This approach presupposes that a known time series of the ground motion of the movable foundations of the building exist for either real life measurement of accelerations or similar. The response of the movable foundation is collected in the vector $y(t)$ or $\ddot{y}(t)$ of dimension six (Three dof at each foundation).

The quasi-static response $x^{(0)}(t)$ of the movable supports is calculated by Equation (3.1) and it is seen that the quasi-static response ignores the inertial and damping forces.

$$x^{(0)}(t) = \boldsymbol{U} y(t) \tag{3.1}$$

The matrix $\boldsymbol{U}$ is called the influence matrix of dimension $n \times m$ and it gives the quasi-static response of the building for each of the $m = 6$ dof in the movable supports when they are exposed to a unit deformation independent of each other. Figure 3.2 shows the quasi-static motion from unit deformation of the left support.

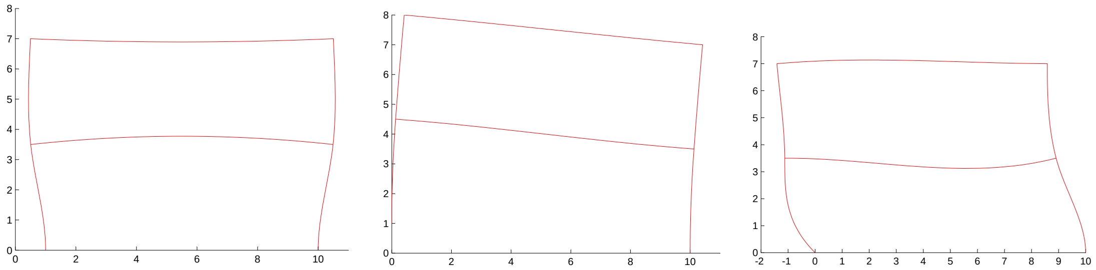

Figure 3.7. Quasi-static motion from unit deformation of left support of building.

The equation of motion for the structure with movable supports can then be written in the following form according to [Nielsen, 2004]:

$$\boldsymbol{M}\ddot{x}(t)+\boldsymbol{C}\dot{x}(t)+\boldsymbol{K}x(t)=\boldsymbol{C}\dot{x}^{(0)}(t)+\boldsymbol{K}x^{(0)}(t)=\boldsymbol{C}\boldsymbol{U}\dot{y}(t)+\boldsymbol{K}\boldsymbol{U}y(t) \tag{3.2}$$

Or if the relative coordinates $z(t)$ are introduced as:

$$z(t)=x(t)-x^{(0)}(t) \tag{3.3}$$

The equation of motion is then written on the form:

$$\boldsymbol{M}\ddot{z}(t)+\boldsymbol{C}\dot{z}(t)+\boldsymbol{K}z(t)=-\boldsymbol{M}\ddot{x}^{(0)}(t)=-\boldsymbol{M}\boldsymbol{U}\ddot{y}(t) \tag{3.4}$$

Equation (3.2) and (3.4) can be solved in the time domain using a standard time integration scheme as e.g. Newmark, with the external dynamic load represented on the right hand side of the equations based on the ground motions $y(t)$.

3.3 Example of Soil-Building interaction

The soil-building interaction is evaluated for the reference case shown in Figure 3.8, where a three-axel Scania bus is crossing a speed bump with 25 km/h. The soil properties correspond to silty clay.

The response for the reference case with the total model, along with the response for two simulations of the building using movable supports are shown in Figure 3.9 and 3.10. The green curves show the results of the ground motion of the foundation points in a model corresponding to Figure 3.8 without the building applied to a fixed model, modelled with movable supports. The rotational degrees-of-freedom are obtained by linearization between the two points in the foundation. The red curve, shows the effect of linearization compared to using the original rotation in the foundation of the reference case illustrated in Figure 3.8.

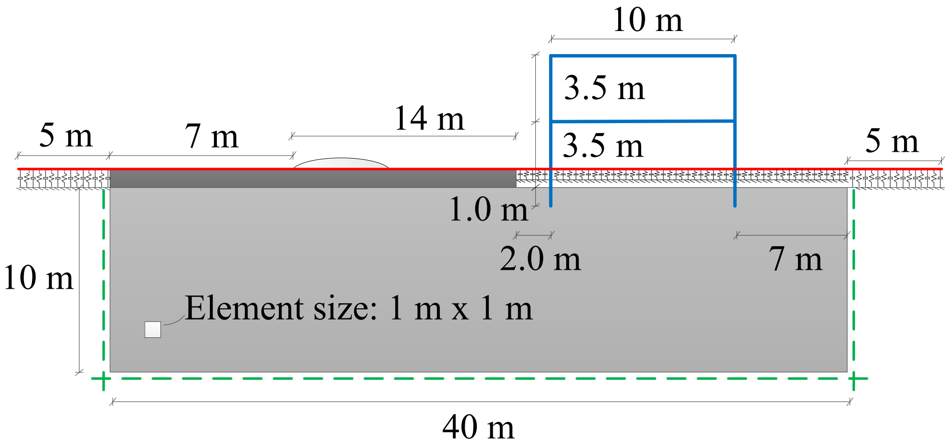

Figure 3.8. Reference case for evaluating soil-building interaction.

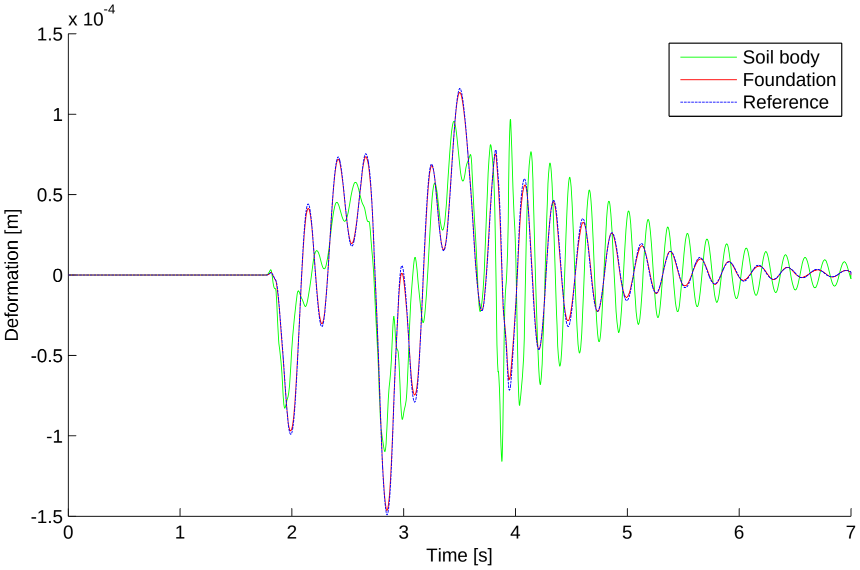

Figure 3.9. Horizontal deformation at the middle of 1st floor of the building.

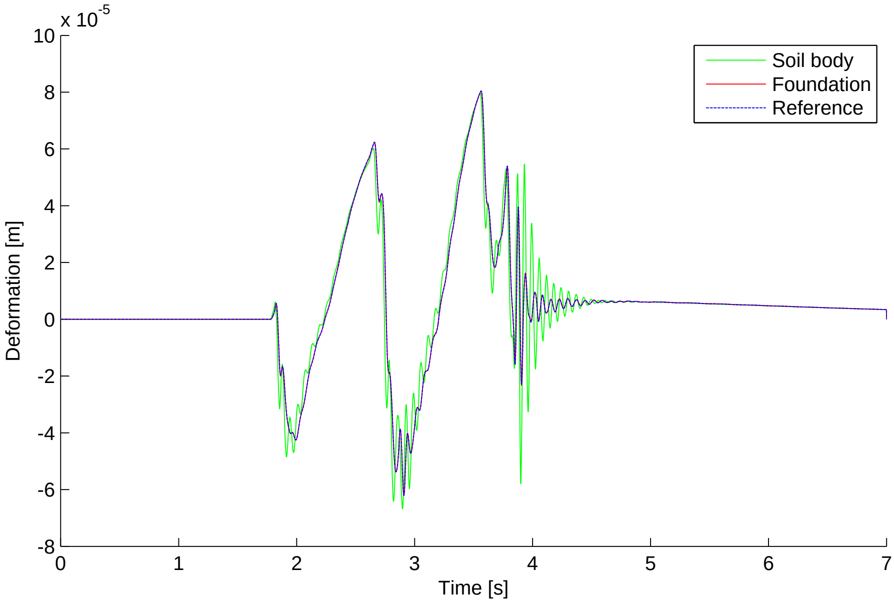

Figure 3.10. Vertical deformation at the middle of 1st floor of the building.

The two Figures 3.9 and 3.10 show that the computed response changes significantly when the ground motion of a soil body without a building is applied to a fixed model of the building, modelled with movable supports, compared to the response of the total FE model. The change in the period between the two cases corresponds well to the difference in eigenfreqency for the first eigenmode of the two cases, as seen in Table 3.1. In general it can be concluded that the interaction between the soil body and the building is important for soft soils.

Chapter 4

2D elements

The elements used for the soil body are plane continuum elements. Isoparametric eight-noded elements are used for this purpose. Shape functions can be found in [Cook et al., 2002]. The element stiffness matrix is derived by evaluating following expression by use of Gauss integration:

$$\mathbf{K} = \int_A \mathbf{B}(x,y)^T \, \mathbf{D} \, \mathbf{B}(x,y) \; t \, dA \tag{4.1}$$

The integration over the area of a distorted element can be difficult. Hence, an isoparametric formulation is used.

$$\mathbf{B} = \mathbf{H} \, \mathbf{J}_{exp}^{-1} \mathbf{D}_{N,exp} \tag{4.2}$$

The inverse expanded Jacobian $\mathbf{J}_{exp}^{-1}$ relates the displacement derivatives in the two coordinate systems.

$$\frac{\partial u_x}{\partial \xi} \rightarrow \frac{\partial u_x}{\partial x} \tag{4.3}$$

For further explanation refer to [Cook et al., 2002] or Section 8.1.

4.1 Element Testing

To verify the element stiffness matrix **K** and mass matrix **M** a simple bar system is made as shown in Figure 4.1. The geometry of the model is: $L = 4$ m and $h = 0.01$ m. The bar is modelled by use of 40 Q8 elements distributed in one column as shown on Figure 4.1 leading 406 degees-of-freedom (dof) in the system. The material properties are given in Table 4.1. Beams are usually treated with plane stress assumptions and the model created by 2D elements are also calculated using plane stress. Note that all calculations in the following are done per meter depth.

E	ν	ρ
210e9 Pa	0.3	8000 kg/m^3

Table 4.1. Material properties for beam model.

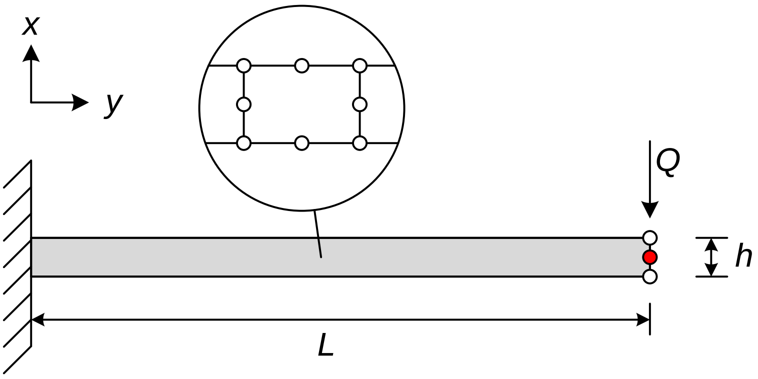

Figure 4.1. Cantilever beam model

The static boundary conditions are as follows: all the dof associated with the nodes at $y = 0$ are fixed in both vertical and horizontal direction.

4.2 Static deformation

The cantilever beam is subjected to a point load of $Q = 100$ N in the top mid node. The analytical Bernoulli-Euler deflection for a cantilever beam with a point load can be found as

$$\begin{aligned} u &= \frac{1}{3}\frac{Q\,h^3}{E\,I} \\ &= 0.1219 \text{ m} \end{aligned} \tag{4.4}$$

In the FE model the deformation measured in the x-direction for the top middle node is

$$u_{\text{num}} = 0.1217 \text{ m} \tag{4.5}$$

4.3 Eigenfrequencies

The circular eigenfrequencies can for a beam with linear elastic material and constant cross section be found as

$$\omega_n = \frac{K}{l^2}\sqrt{\frac{E\,I}{\mu}} \qquad n = 1{,}2{,}3... \tag{4.6}$$

Here μ is the distributed mass. Using the tables in Teknisk Ståbi [Jensen, 2012] for the values of K following values for the eigenfrequencies associated with the first 4 eigenmodes are (in Hz)

$$f_0 = [\,0.52 \quad 3.30 \quad 9.08 \quad 17.80\,] \tag{4.7}$$

The eigenfrequencies from the FEM model are obtained by solving the eigenvalue problem

$$\left(\mathbf{K} - \omega^2\,\mathbf{M}\right)\;\Phi = 0 \tag{4.8}$$

Here, $\mathbf{M}$ and $\mathbf{K}$ are the reduced global matrices only containing values from the free degrees of freedom. The four lowest values of the eigenfrequencies are given as

$$f_{0,\text{num}} = [\, 0.52 \quad 3.25 \quad 9.09 \quad 17.81 \,] \tag{4.9}$$

On Figure 4.2 the modeshapes for the first four eigenfrequencies are shown.

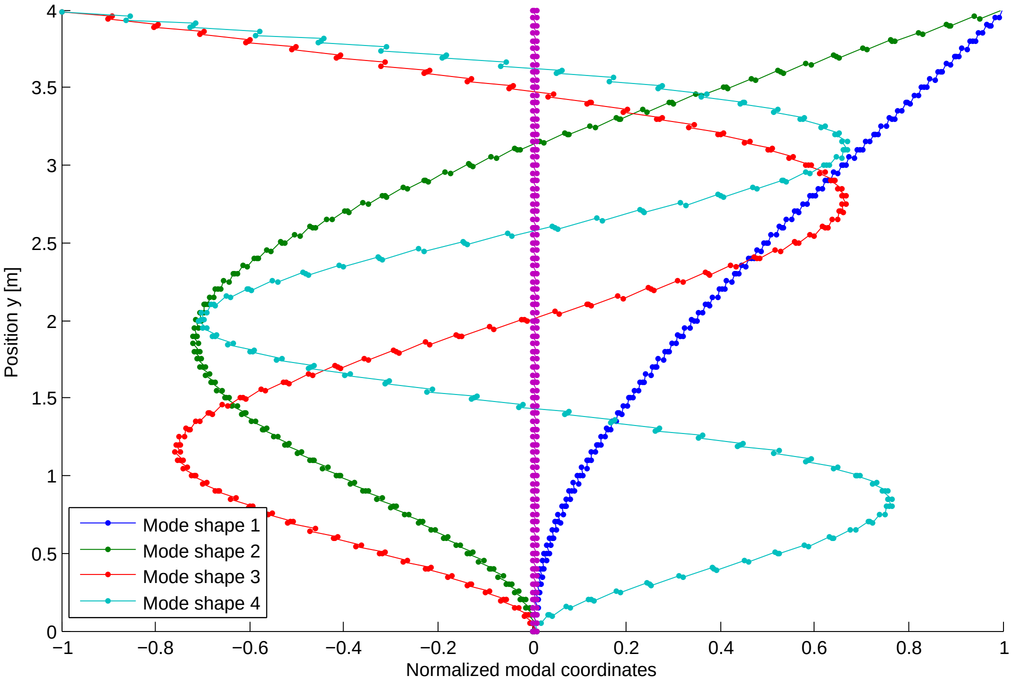

Figure 4.2. Modeshapes for the cantilever beam.

To verify that the response from the time integration scheme is correct, an impulse load is applied at the same node as shown on Figure 4.1. The beam is then left to vibrate freely without any damping of the system. The nodal displacement in the x direction is extracted from the displacement matrix $\mathbf{U}$ at the same node and a Fourier transformation is performed. The frequency spectrum is plotted in Figure 4.3 along with the four analytical values of the eigenfrequencies.

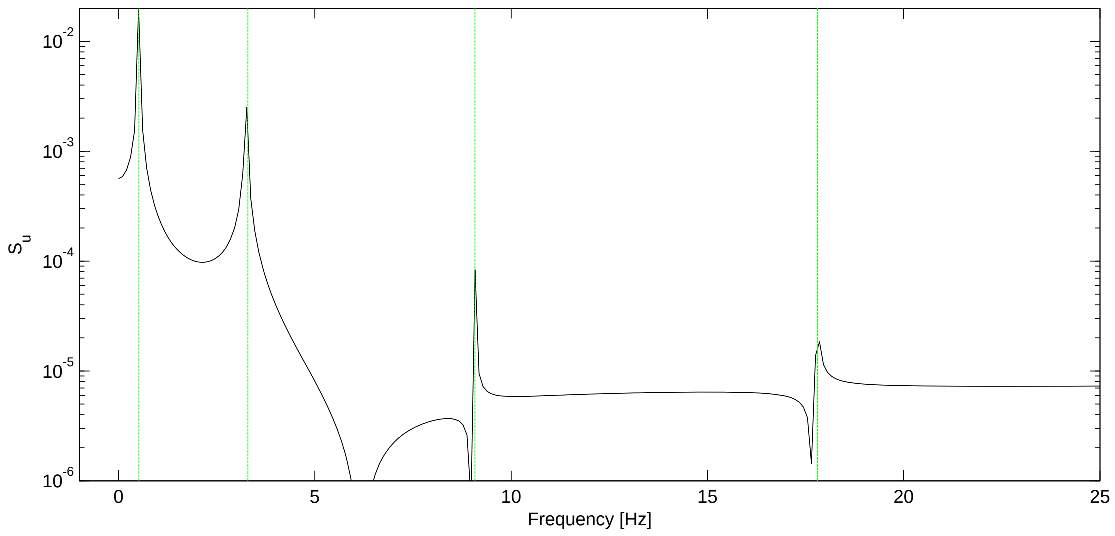

Figure 4.3. Absolute values of the frequency spectrum.

4.4 Comparison with Plaxis

In order to verify the behaviour of the dynamic FE model, a comparison study is made where a simple rectangular model is compared with Plaxis. The geometry and discretisation for the FE model are shown in Figure 4.4 along with the placement of the dynamic load. The upper boundary is free, while the rest are fixed perpendicular to the boundary. The geometry for Plaxis is the same, with standard fixities, while the elements in Plaxis are 15 noded isoparametric triangles instead of 8-noded isoparametric quadrilateral elements in the Matlab model.

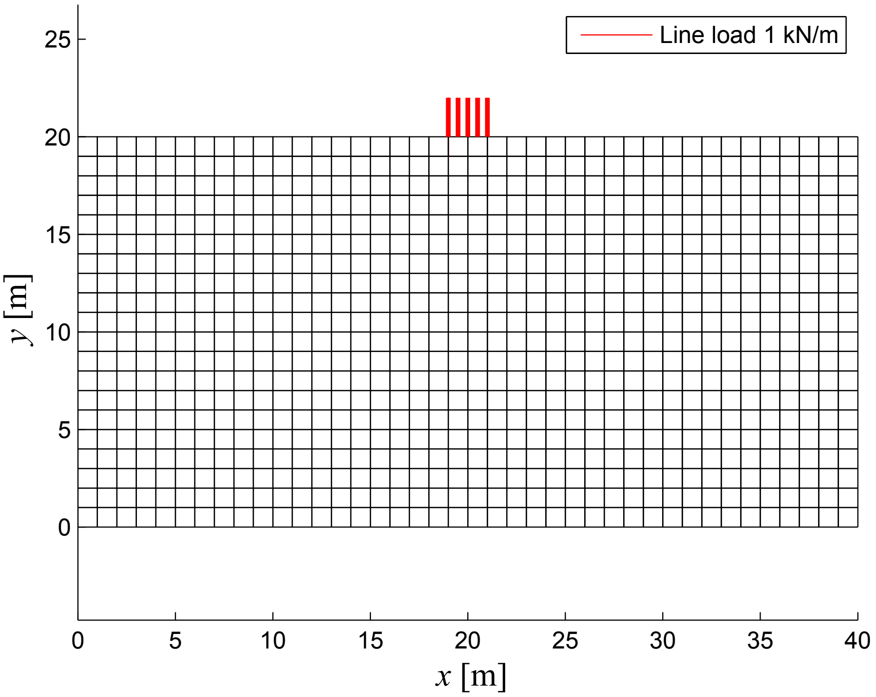

Figure 4.4. Discretisation of mesh and placement of load.

The material parameters for both models are shown in Table 4.2. The material models are linear elastic plane strain for both cases.

Young's modulus	E	50 MPa
Poisson's ratio	ν	0.3
Density	ρ	2000 kg/m^3

Table 4.2. Material properties for analysis.

The dynamic load is applied as two sine curves with at frequency of 10 Hz for the lineload shown in Figure 4.4 over a length of 2 metres. The boundary load vector $\mathbf{f}_b$ for the line load is assembled from the surface pressure $\mathbf{q}$ over the surface S with thickness t. Cook et al. [2002]

$$\mathbf{f}_b = \oint_S N^T \mathbf{q}\, t\, dS \tag{4.10}$$

The distributed load on the surface can be decomposed into a component in the x- and the y-direction as illustrated in Figure 4.5. The angle θ in Equation (4.11) is measured from a horizontal line and up to the surface load vector $\mathbf{q}$.

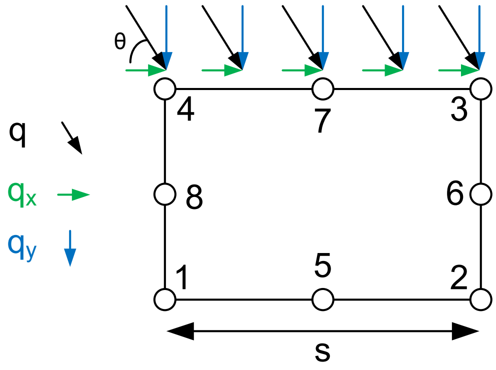

Figure 4.5. Distributed surface load on top of Q8 element.

$$\mathbf{q} = \begin{bmatrix} \mathrm{q}_x \\ \mathrm{q}_y \end{bmatrix} = \begin{bmatrix} |\mathbf{q}| \cdot \cos\theta \\ |\mathbf{q}| \cdot \sin\theta \end{bmatrix} \tag{4.11}$$

For the 8-noded isoparametric quadrilateral element with a line load on top over the thickness t as illustrated in Figure 4.5 this gives the equivalent boundary load vector given in Equation (4.12).

$$\mathbf{f}_b = \begin{bmatrix} 0\;0\;0\;0\;0\;0\;0\;0\;\tfrac{1}{6}\mathrm{q}_x\;\tfrac{1}{6}\mathrm{q}_y\;\tfrac{2}{3}\mathrm{q}_x\;\tfrac{2}{3}\mathrm{q}_y\;\tfrac{1}{6}\mathrm{q}_x\;\tfrac{1}{6}\mathrm{q}_y\;0\;0 \end{bmatrix}^T \cdot t \cdot s \tag{4.12}$$

In Plaxis the load is applied on top of a plate with stiffness corresponding to concrete. After the load is applied additional steps are calculated in order to evaluate how the waves propagate through the model. The time series for the load is shown in Figure 4.6.

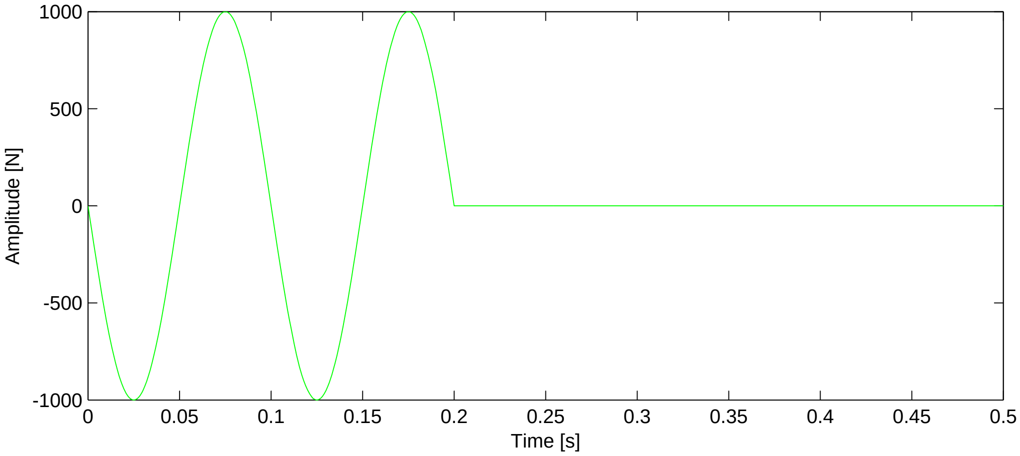

Figure 4.6. Dynamic load.

The displacement for a point at the surface 10 m from the middle of the dynamic load at $x = 30$ m are shown in Figure 4.7 for both Plaxis and Matlab. It seems that the

Matlab FE model fits very well to the Plaxis model until the waves are reflected at the boundaries. Figure 4.8 shows the same results from Plaxis with transmitting boundary conditions (TBC).

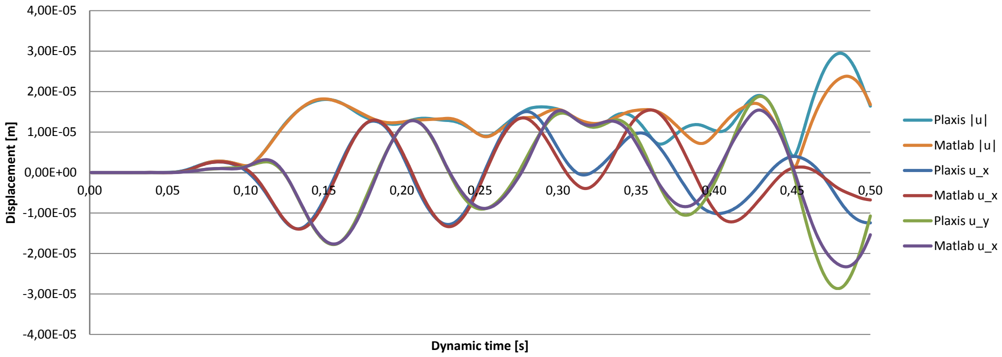

Figure 4.7. Displacement at $x = 30$ m for Plaxis and Matlab model with standard BC.

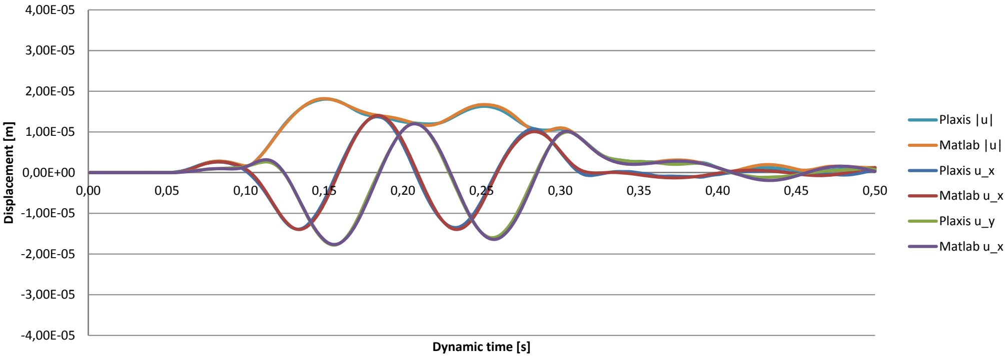

Figure 4.8. Displacement at $x = 30$ m for Plaxis and Matlab model with TBC.

The phase speed for primary waves can be calculated by:

$$c_P = \sqrt{\frac{\lambda + 2\mu}{\rho}} \tag{4.13}$$

λ | Lamé constant, see Eq. (4.14) and (4.15)
μ | Lamé constant $\mu = G$ (Shear modulus)

For three-dimensional cases and for plane strain the first Lamé constant is given by:

$$\lambda = \frac{\nu E}{(1+\nu)(1-2\nu)} \tag{4.14}$$

While it for plane stresses is given by:

$$\bar{\lambda} = \frac{\nu E}{1-\nu^2} \tag{4.15}$$

The secondary phase speed for shear waves is given by:

$$c_S = \sqrt{\frac{\mu}{\rho}} \tag{4.16}$$

The Rayleigh wave speed cannot be given explicitly, but only in terms of c_P and c_S:

$$\left(2 - \frac{c_R^2}{c_S^2}\right)^2 = 4\left(1 - \frac{c_R^2}{c_P^2}\right)^{\frac{1}{2}}\left(1 - \frac{c_R^2}{c_S^2}\right)^{\frac{1}{2}} \tag{4.17}$$

The wave speeds for the different wave types and the arrival time for different distances are shown in Table 4.3. The arrival times correspond well with the results in Figure 4.7 in which the disturbance from the boundary starts after approximate 0.22 s, which is the arrival time for the first and second reflected P-waves.

	wave speed	t ($s = 10$ m)	t ($s = 30$ m)	t ($s = 40$ m)
c_P	183.4 m/s	0.055 s	0.164 s	0.218 s
c_S	98.1 m/s	0.102 s	0.306 s	0.408 s
c_R	90.9 m/s	0.110 s	0.330 s	0.440 s

Table 4.3. Wave speeds and arrival time for P-, S- and Rayleigh wave.

Chapter 5

Transmitting Boundary Conditions

In a finite-element analysis infinite soil volumes are usually modelled using artificial boundary conditions. In a static analysis Neumann and Dirichlet boundary conditions are used to simulate fixities and the results will be accurate if the boundaries are located sufficiently far from the point of interest. In a dynamic analysis, however, complications arise as Neumann and Dirichlet boundary conditions will cause reflection of waves. Instead so-called transmitting boundary conditions (TBC) are applied.

5.1 Impedance Boundary Conditions

In [Andersen, 2012] a geometrical and a mechanical method to simulate TBC are described. The geometrical method is to include buffer elements at the transmitting boundaries with a high material damping, while the mechanical method make use of the impedance condition. The last method is used in most commercial software like Plaxis [R.B.J. Brinkgreve, 2011] and will be implemented in the program. The concept or impedance boundary conditions is illustrated in Figure 5.1.

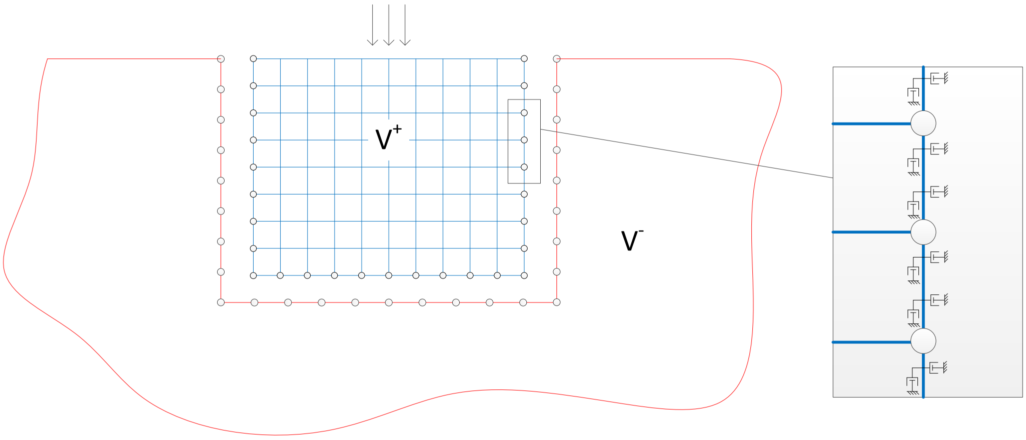

Figure 5.1. Impedance boundary condition.

As indicated a series of artificial dampers is applied along the transmitting boundary to absorb the energy from P- and S-waves. The value of the dampers depends on the wave speeds, the Lamé constants and the direction of the incoming wave as described by the following expression from [Andersen, 2006]:

$$c_{ij} = \frac{1}{c_P}\left(\lambda^- n_i^+ p_j + 2\mu^- n_k^+ p_k p_i p_j\right) + \frac{\mu^-}{c_S}\left(p_i n_j^+ + n_k^+ p_k \delta_{ij} - 2n_k^+ p_k p_i p_j\right) \tag{5.1}$$

c_{ij}	Damping per meter boundary
p	Unit direction vector for wave propagation
n	Normal vector to the boundary

Notice that the indices (+) and (-) relate to the internal and the external soil volume, respectively. The expression above is valid for a fixed coordinate system, hence the propagation direction is the same for both P- and S-waves. Generally the vector p can only be determined uniquely for very simple cases. In most situations a boundary will be affected by waves from several different directions due to e.g. reflection or moving loads. For now the following simplification is done:

- The waves propagate perpendicular to the boundary: $p = -n$

The nodal forces acting on the internal soil volume from the external volume can be related to the damping on the boundary and discretised using the following expression [Andersen, 2006]:

$$\mathbf{f}_b^+(t) = \int_{S_0} \mathbf{N}_i^T c_{ij} \mathbf{N}_i \; dS \; \dot{\mathbf{u}}_b^+(t) = -\mathbf{C}_{bb}^- \dot{\mathbf{u}}_b^+(t) \tag{5.2}$$

The index b refers to the degrees of freedom in connection with the boundary. The matrix $\mathbf{C}_{bb}^-$ is denoted the impedance matrix and can be determined by eliminating the nodal velocities from the expression.

5.2 Implementation in FEM

The impedance boundary condition is implemented by adding the impedance matrix to the system damping matrix. In practice this will be done during the assemblance of the system matrices. For simplification, only square volumes are considered where the sides are numerated according to Figure 5.2.

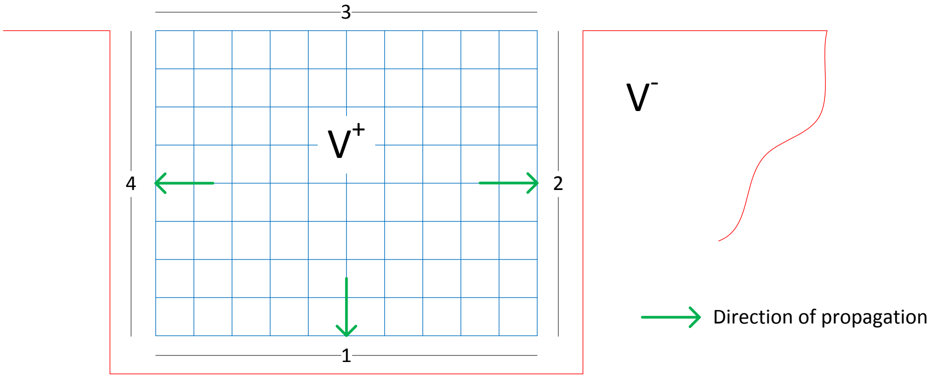

Figure 5.2. Numeration of boundaries.

A vector is set up in the load input denoted **SysAb** with a value of one for each TBC and zero for non-TBC. For the example above the equation is:

$$\mathbf{SysAb} = \begin{bmatrix} 1 & 1 & 0 & 1 \end{bmatrix} \tag{5.3}$$

A matrix **P** storing the wave propagation directions is defined as well. The propagation vectors are inserted as columns:

$$\mathbf{P} = \begin{bmatrix} 0 & 1 & 0 & -1 \\ -1 & 0 & 0 & 0 \\ 0 & 0 & 0 & 0 \end{bmatrix} \tag{5.4}$$

Notice that the third column describing the non-TBC is set to zero in order to ensure that no contribution will be made to the system damping at this boundary. All three dimensions are included in the calculation of c_{ij} whereafter the relevant part is extracted. For each element a four step loop is performed, one step for each side where the numeration for the local element follow the global numeration in Figure 5.2. The procedure in the assemblance is described by the following points:

1. Is the side of the element on the boundary? E.g. $y_{local} = y_{global}$.

   No: Start over with the next side.

   Yes: Continue
2. Calculate c_{ij} using the associated wave propagation vector **p**.
3. Perform a one-dimensional Gauss integration:

   Determine integration coordinates (Gauss points) for variable direction.

   Determine integration coordinates for constant direction, e.g. $y = y_{min}$.

   Determine the weight values.

   Calculate the local impedance matrix according to (5.2).
4. Ad the local impedance matrix to the global system matrix.

5.3 Verification

In order to validate the procedure described above two simple cases are considered, see Figure 5.3. In both cases a sinusoidal load of one period is applied and the response is measured in a node near the boundary. No damping is applied to the model and the material parameters are of no significant importance to the validation.

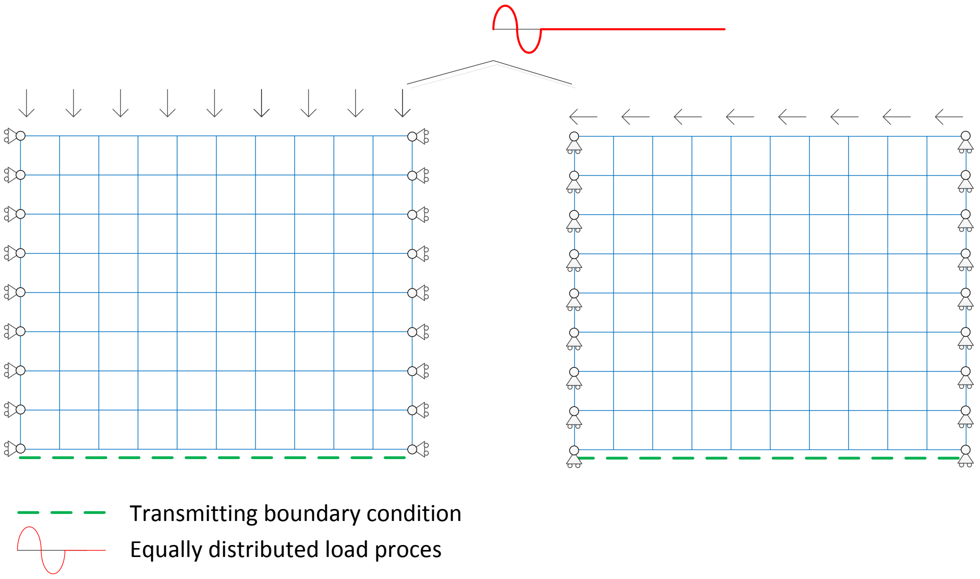

Figure 5.3. Models used for validation.

The two models represent special cases where pure pressure and shear waves are generated respectively. The line loads are applied at the surface and distributed to the nodes according to the shape functions. In order to illustrate the propagation of the two wave types, plots of the deformed mesh for both models are given in Figure 5.4.

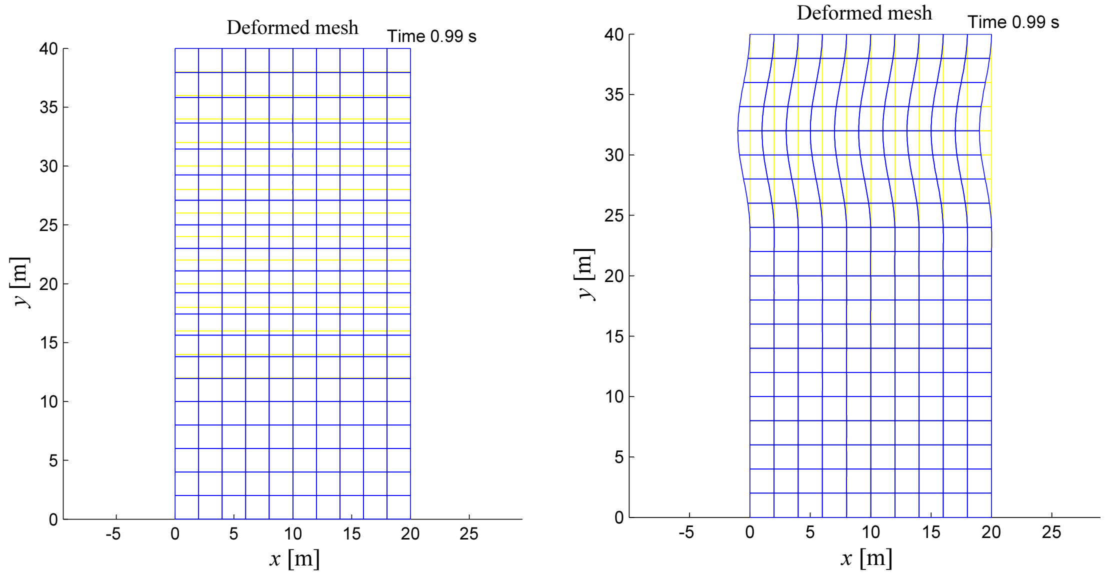

Figure 5.4. L. Deformation from pressure wave, R. Deformation from shear wave.

In order to verify that the TBC function properly a time series is plotted for a node close to the boundary, see Figure 5.5. In Figure 5.5 plots are made for the model with pure pressure wave both with and without the TBC. In the case without TBC the bottom boundary is fixed against vertical movement in order to prevent stiff body motion.

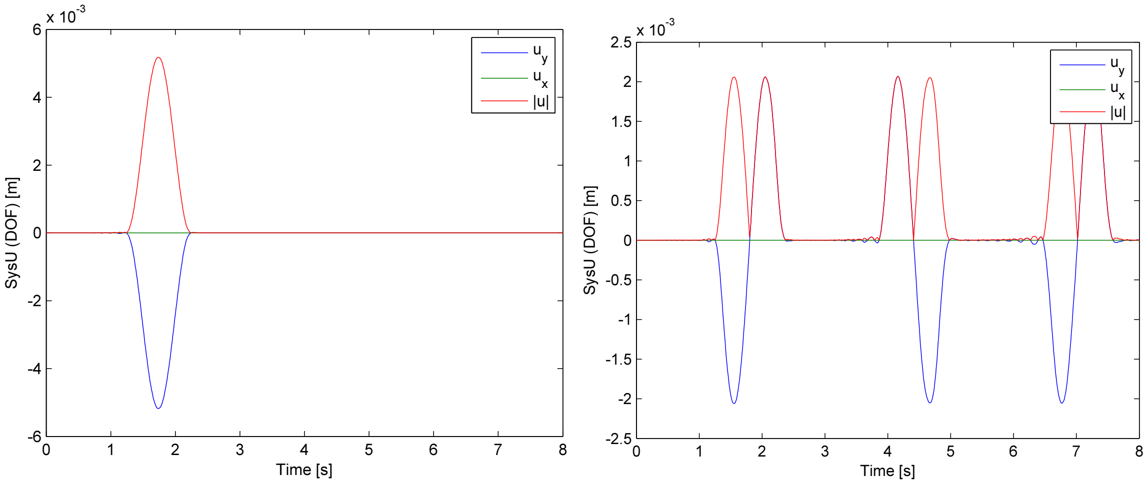

Figure 5.5. L. Node displacement with TBC (pressure), R. Node displacement without TBC (pressure).

A similar analysis can be done for the model with pure shear wave, see Figure 5.6

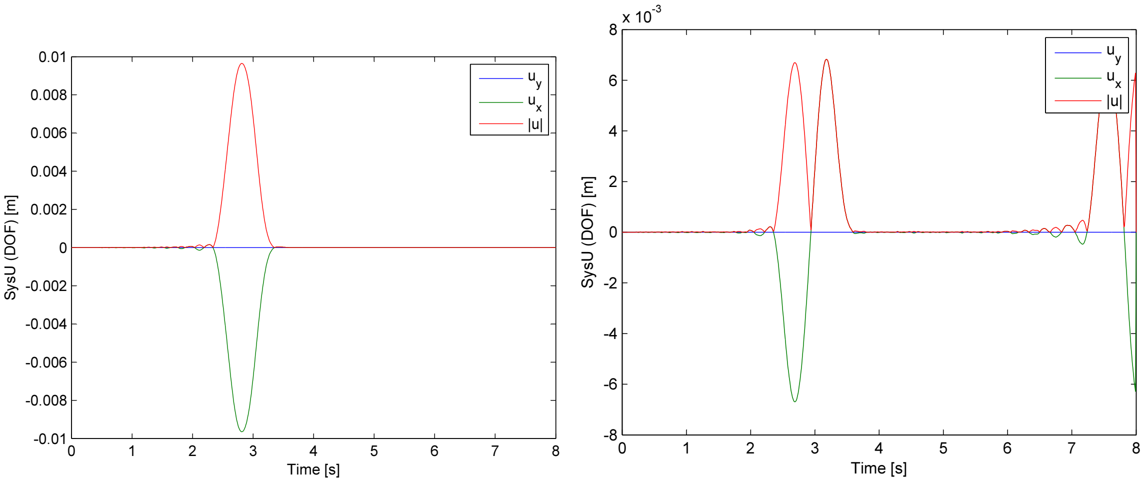

Figure 5.6. L. Node displacement with TBC (shear), R. Node displacement without TBC (shear).

As illustrated in the figures the TBC's are functioning properly for the special cases.

5.4 Soil layering

For a wave travelling through layered material with different impedance, part of the energy is reflected at the interface while a part is transmitted. For the one dimensional case the reflection and transmission coefficients, C_r and C_t, regarding particle velocities are given as: [Andersen, 2006]

$$C_r = \frac{v^r(t)}{v^i(t)} = 1 - C_t \tag{5.5}$$

$$C_t = \frac{v^t(t)}{v^i(t)} = \frac{2z_1}{z_1 + z_2} \tag{5.6}$$

In Matlab a model is constructed to see if the portion of wave energy is transmitted and reflected as expected considering (5.5) and (5.6). The model is sketched in Figure 5.7. The model is loaded uniformly from one side forming a pure pressure wave moving in the y-direction.

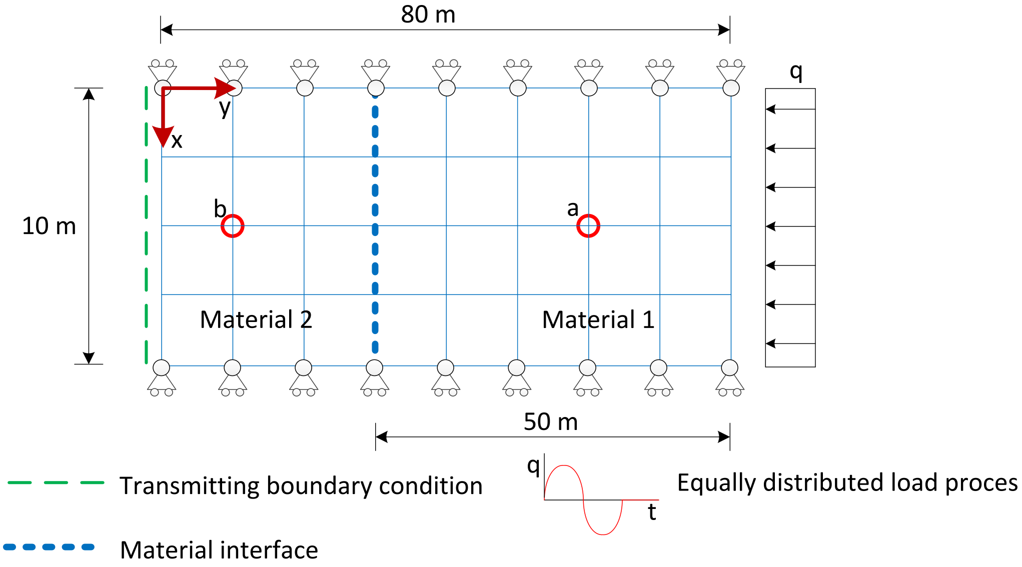

Figure 5.7. Matlab model for analysis

The model is made using 800 squared elements. It is made from two different materials given by Tabel 5.1. Assuming plane strain condition the wave speed for the pressure wave in the two materials is calculated from (4.13):

$$c_{P1} = 35.81 \text{ m/s} \tag{5.7}$$

$$c_{P2} = 61.15 \text{ m/s} \tag{5.8}$$

Evaluating (5.5) and (5.6) with the material parameters given in Table 5.1 shows the expected reflection and transmission coefficients regarding the particle velocity.

$$C_r = 0.1883 \tag{5.9}$$

$$C_t = 0.8117 \tag{5.10}$$

Material 1			Material 2		
ν	E	ρ	ν	E	ρ
0.3	2e6 Pa	2100 kg/m^3	0.3	5e6 Pa	1800 kg/m^3

Table 5.1. Material properties.

Plotting the particle velocities at point a (5, 10) and b (5, 60) as a function of time leads following results:

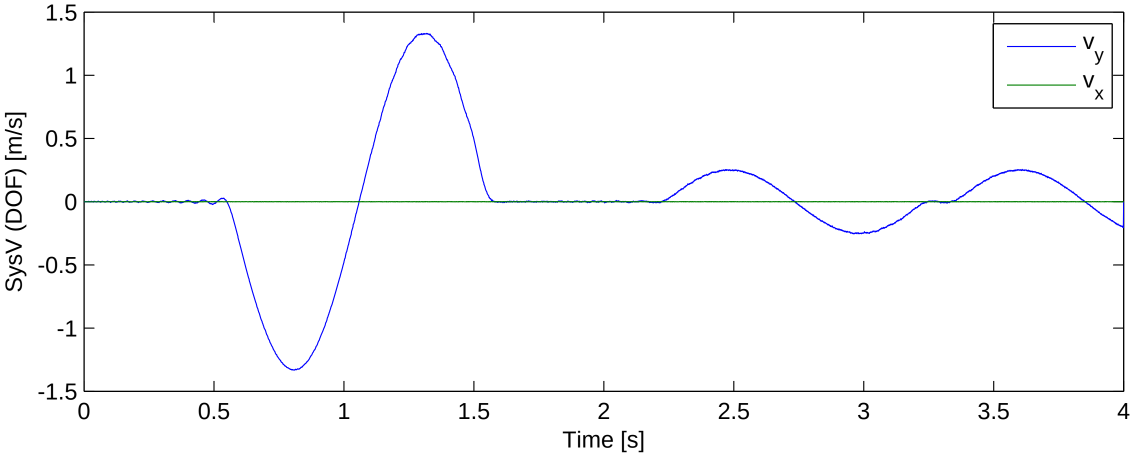

Figure 5.8. Particle velocity at point *a*

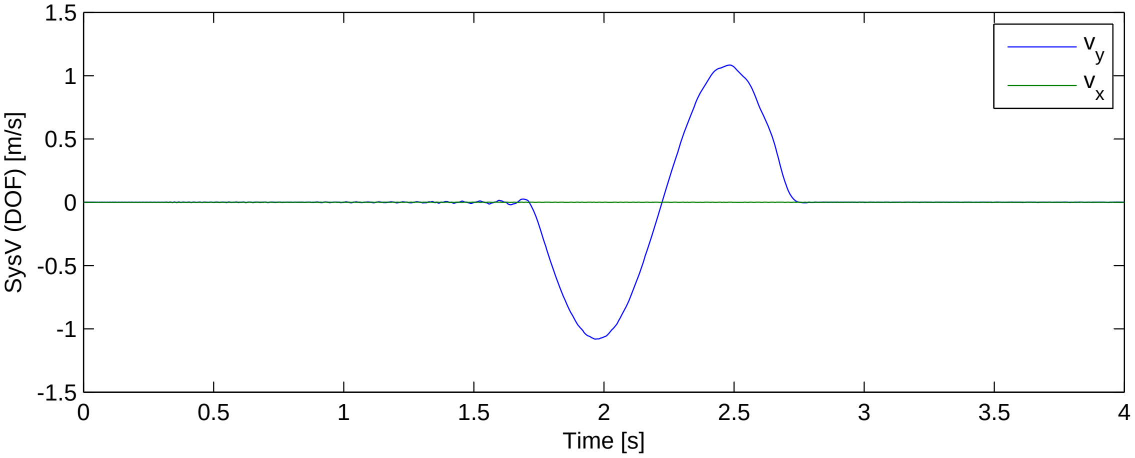

Figure 5.9. Velocity at point *b*

From Figure 5.8 it is seen that the wave, when it hits the material interface, reduces its amplitude without change in sign as it is reflected. In Figure 5.9 it is seen how a part of the wave energy is transmitted into material 2 and dissipates into the absorbing boundary.

The peak velocities at point *a* shown in Figure 5.8 are $v_y = 1.33$ m/s and $v_y = 0.25$ m/s while as the peak velocity at point *b* is $v_y = 1.08$ m/s.

Calculating the reflection and transmission coefficients based on the velocities observed.

$$C_r = \frac{v^r(t)}{v^i(t)} = \frac{0.25\ \mathrm{m/s}}{1.33\ \mathrm{m/s}} = 0.1880 \tag{5.11}$$

$$C_t = \frac{v^t(t)}{v^i(t)} = \frac{1.08\ \mathrm{m/s}}{1.33\ \mathrm{m/s}} = 0.8120 \tag{5.12}$$

The results obtained from this analysis shows a good resemblance to the analytical results presented in (5.9).

Frequency Domain Solution

Instead of solving dynamic problems in the time domain, the analysis can be carried out in the frequency domain. The procedure for doing so is described in the following. First the load ***f** (t)* is transformed into the frequency domain by use of Fast Fourier Transformation (FFT). Then (6.1) is solved for every value of ω each forming a vector in **U**. **M**, **C** and **K** are the reduced system matrices containing the free dofs. [Andersen, 2006]

$$\left(-\omega_j^2\,\mathbf{M} + i\,\omega_j\,\mathbf{C} + \mathbf{K}\right)\mathbf{U}_j = \mathbf{F}_j \tag{6.1}$$

where

$$\omega_j = 2\pi\left(j-1\right)/T, \quad j = 1{,}2...J \tag{6.2}$$

The velocity and acceleration can be obtain from the **U** matrix.

$$\dot{\mathbf{U}}_j = i\,\omega_j\,\mathbf{U}_j \tag{6.3}$$

$$\ddot{\mathbf{U}}_j = -\omega_j^2\,\mathbf{U}_j \tag{6.4}$$

Next, the solution is transformed back into the time domain by inverse Fast Fourier Transformation ifft.

6.1 Simply supported beam

To illustrate the procedure a simply supported beam with a point load acting at midspan is analysed in both the time domain and the frequency domain. The beam is analysed using Bernoulli Euler theory with Rayleigh viscous damping with the following beam properties:

I	E	A	ρ
0.01 m^4	2e9 MPa	0.5 m^2	7000 kg/m^3

Elements	Span	α	β
40	20 m	0.1	0.1

Table 6.1. Beam properties.

The time is discretized in the following way

- $dt = 0.001$ s;
- $t = 0 : dt : 25$ s;

The load is set to vary in time as a harmonic sinusoidal function with a period of 0.5 s and an amplitude of 400 N. Solving (6.1) for $\mathbf{U}$ and plotting the vertical component for the frequency which leads the biggest response in $\mathbf{U}$.

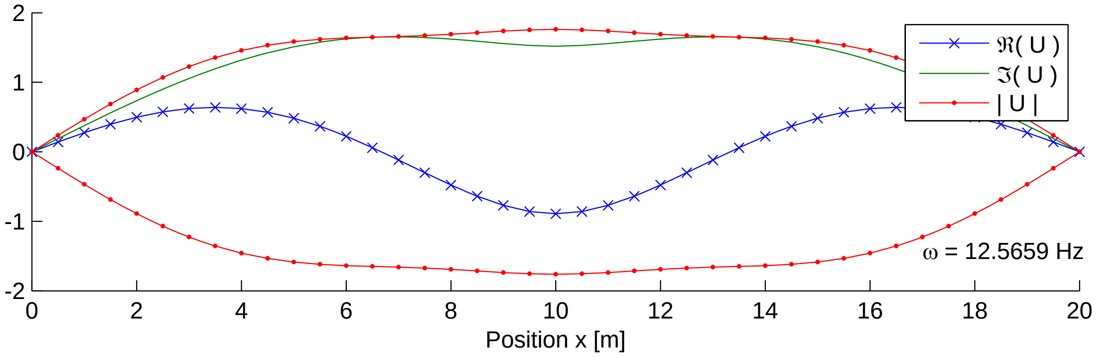

Figure 6.1. Components in $\mathbf{U}$

By conducting an ifft the result is transformed back into the time domain. In Figure 6.2, 6.3 and 6.4 the deformation, velocity and acceleration are plotted respectively along with the the response obtained by use of a Newmark scheme with the integration parameters as $\gamma = 1/2$ and $\beta = 1/4$. It is seen that the initial disturbance from the load is damped out in time for the Newmark solution and approaches the stationary response obtained from the frequency domain solution.

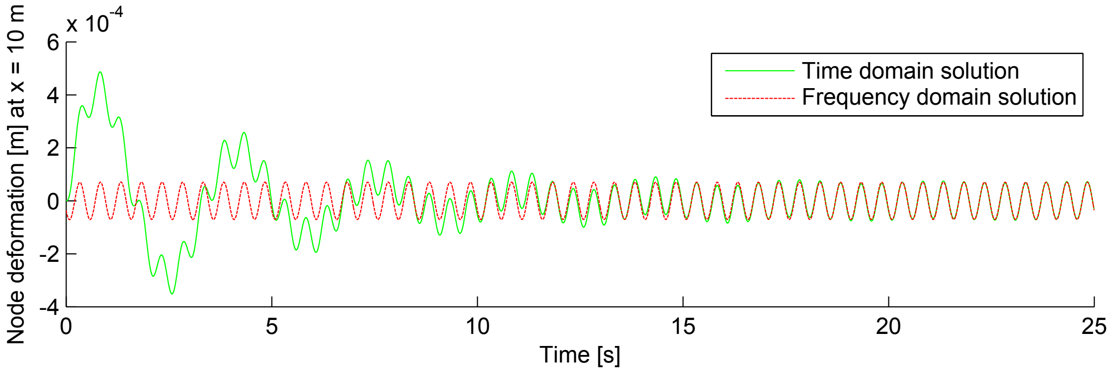

Figure 6.2. Node deformation

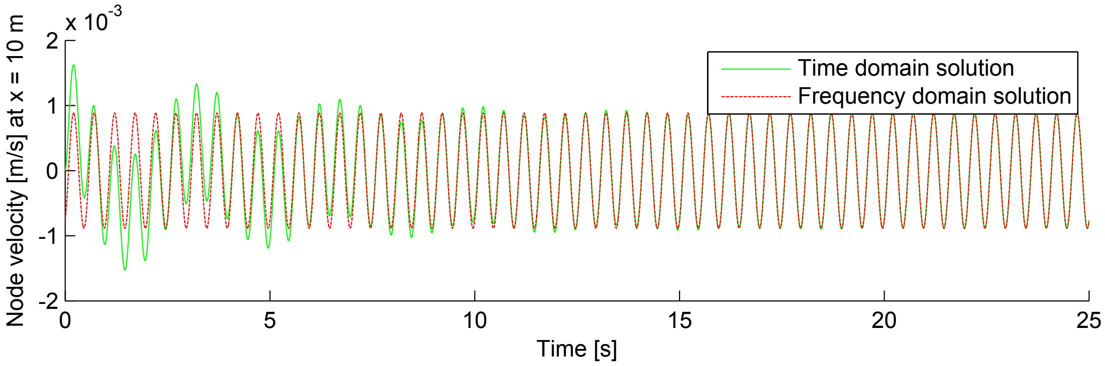

Figure 6.3. Node velocity

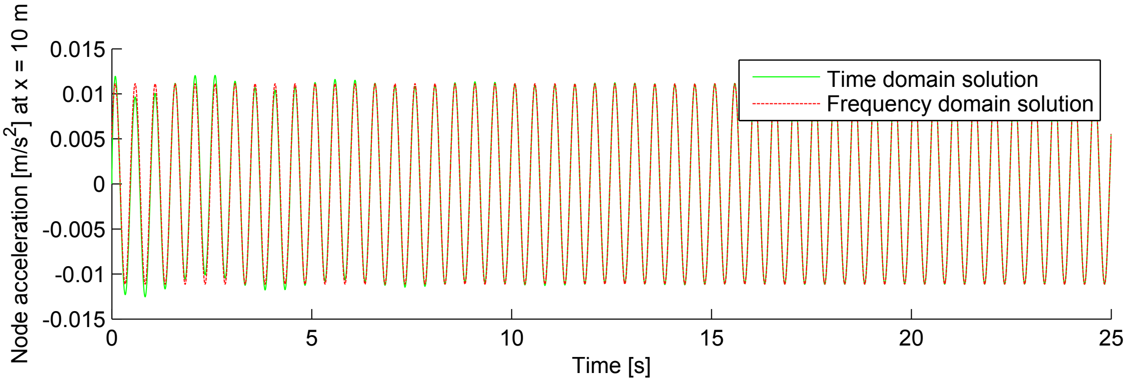

Figure 6.4. Node acceleration

6.2 Plane elements

Since the frequency domain provides the stationary solution to a harmonic load it is good for illustrating the validity of the absorbing boundary conditions described in Chapter 5. A local harmonic loading is set to act at the top mid of the model shown in Figure 6.5 on the following page. The nodal deformation is plotted for different loading frequencies. It is evident that for the model with transmitting boundary conditions the waves propagates as expected, while as for the model with fixed boundaries, the waves are reflected back into the system causing a lot of interference.

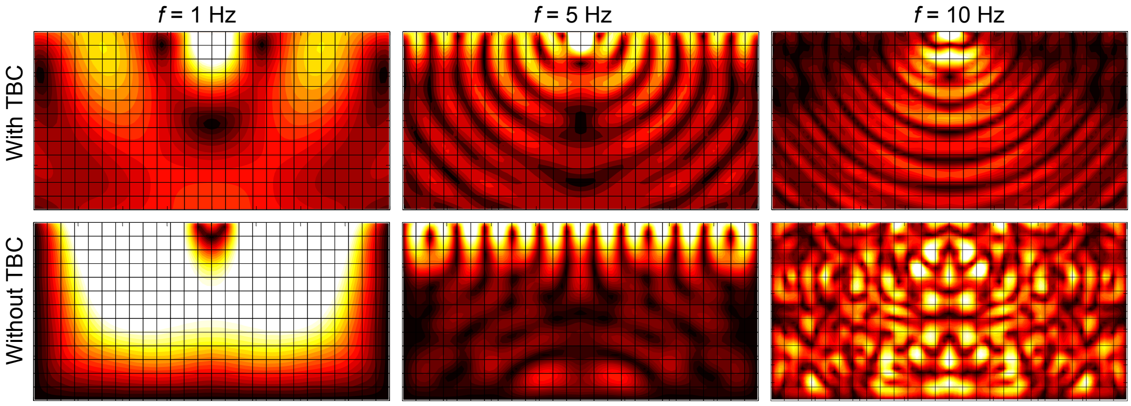

Figure 6.5. Wave propagation in a plane elastic model.

Chapter 7

Road Elements

The following chapter contains a description of the road model and the associated assumptions. The road can be devided in two parts: beams and so-called interface elements. Relevant theory will be presented and verifications of the models are performed, when it is possible.

7.1 The Kelvin Model

The purpose of the road is to connect the vehicle model with the soil volume beneath and to include the possibility of changing parameters such as the stiffness of the pavement. The road model is constructed with inspiration from the Kelvin-Pasternack foundation described in [Andersen, 2006]. A Kelvin-Pasternack foundation consist of a shear layer on top of vertical spring and damper supports. The shear layer will not be included in the model, hence, the "Pasternack" part is eliminated. The model is illustrated in Figure 7.1.

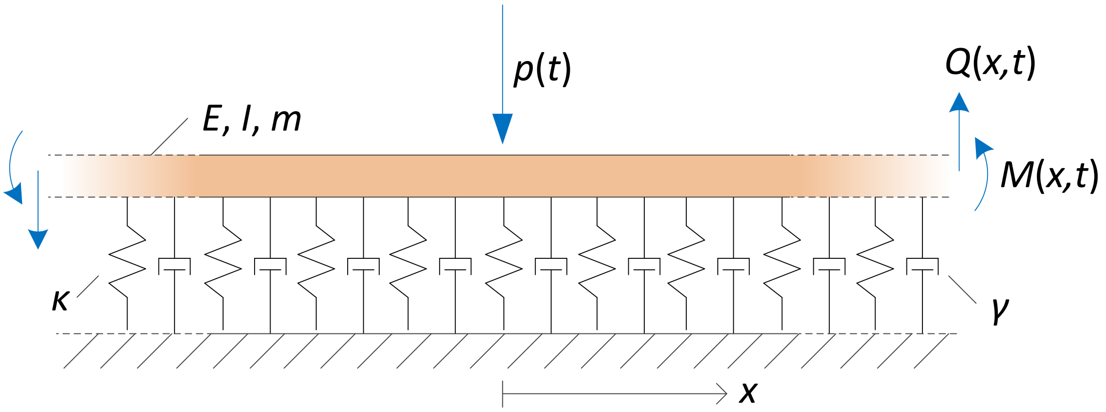

Figure 7.1. Bernoulli-Euler beam on Kelvin foundation.

One of the benefits of the model is that it can be analysed both numerically and analytically whereby the analytical solution can be used to verify the numerical model. The dynamic equation of motion to the problem is written below:

$$E\ I\ \frac{\partial^4 u}{\partial x^4} + m\frac{\partial^2 u}{\partial t} + \gamma\frac{\partial u}{\partial t} + \kappa u = f \tag{7.1}$$

EI	Bending stiffness of the beam
m	Beam weight per length
κ	Spring stiffness per length
γ	Damping constant per length
$u(x,t)$	Vertical displacement relative to equilibrium
$f(x,t)$	Applied force

An analytical solution to the equation can be found if the load is considered harmonic $f = f(\omega)$, located at $x = 0$. The solution is obtained using Fourier transformation and the sign convention from [Andersen, 2002] is adopted. Since the load is considered harmonic the fundamental solution set to Equation (7.1) can be written on the form:

$$u_n(x,t) = U_n \exp^{i(k_n x - \omega t)}, \qquad n = 1,2,3,4 \tag{7.2}$$

U_n	Amplitude of wave component at $x = 0$
k_n	Angular wave number
ω	Force frequency

The wavenumber k_n is likely complex and due to the sign convention the real part and the imaginary part represent the wave propagation and attenuation respectively. The concept is illustrated in Figure 7.2.

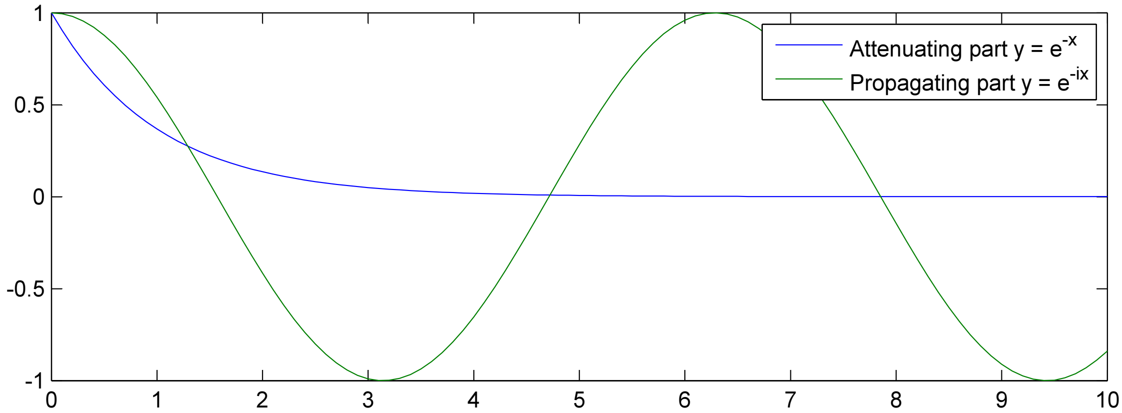

Figure 7.2. Attenuation and propagation.

For a non-moving load considered from a fixed coordinate system the solution to (7.1) is:

$$k_n^4 + \frac{\kappa - m\omega^2 - i\omega\gamma}{EI} = 0 \tag{7.3}$$

Four roots are calculated and these are divided in waves propagating at each side of the force according to [Andersen, 2002]. In most cases the wavenumbers can be sorted by considering the imaginary part, where a negative value is associated with wave propagating to the left of the force (k_1 and k_2) and vica versa. Once the wavenumbers are sorted the associated wave amplitudes can be determined from:

$$\begin{bmatrix} -1 & -1 & 1 & 1 \\ -ik_1 & -ik_2 & ik_3 & ik_4 \\ -(ik_1)^2 & -(ik_2)^2 & (ik_3)^2 & (ik_4)^2 \\ -(ik_1)^3 & -(ik_2)^3 & (ik_3)^3 & (ik_4)^3 \end{bmatrix} \begin{bmatrix} U_1 \\ U_2 \\ U_3 \\ U_4 \end{bmatrix} = \begin{bmatrix} 0 \\ 0 \\ 0 \\ \frac{P}{EI} \end{bmatrix} \tag{7.4}$$

In the matrix above P refers to the amplitude of the harmonic load. The displacement field can be calculated from the sum of the components in the solution set:

$$u(x,t) = \begin{Bmatrix} U_1(\omega)\exp^{-k_1^a x + i(k_1^p x - \omega t)} + U_2(\omega)\exp^{-k_2^a x + i(k_2^p x - \omega t)} & \text{for} \quad x \leq 0 \\ U_3(\omega)\exp^{-k_3^a x + i(k_3^p x - \omega t)} + U_4(\omega)\exp^{-k_4^a x + i(k_4^p x - \omega t)} & \text{for} \quad x > 0 \end{Bmatrix} \tag{7.5}$$

The analytical solution will be used in an example later on.

7.2 Numerical Kelvin model

The problem described above can be treated using a numerical model as well. In a numerical model a finite part of the infinite beam is modelled and boundary conditions are applied at the ends to simulate the missing part. In this problem, only vertical deformation and rotation is considered and the boundaries can hereby be simulated by applying section forces $Q_b(t)$ and $M_b(t)$ corresponding to the forces in an infinite beam, see Figure 7.3.

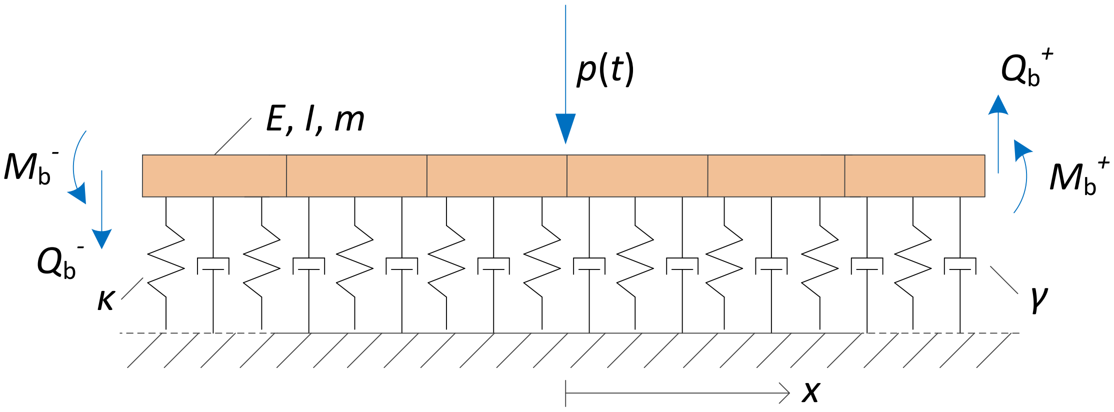

Figure 7.3. Numerical model of the Kelvin foundation problem.

The finite part of the beam is modelled using Bernoulli beam elements with a contribution from the elastic foundation. The contribution is calculated by integrating over the shape functions as it was done for the transmitting boundary conditions. The element matrices are calculated from:

$$\mathbf{M} = \int_{x_e^-}^{x_e^+} \mathbf{\Phi}^T m \mathbf{\Phi} dx \tag{7.6}$$

$$\mathbf{C} = \int_{x_e^-}^{x_e^+} \mathbf{\Phi}^T \gamma \mathbf{\Phi} dx \tag{7.7}$$

$$\mathbf{K} = \int_{x_e^-}^{x_e^+} \frac{\partial^2 \mathbf{\Phi}^T}{\partial x^2} EI \frac{\partial^2 \mathbf{\Phi}}{\partial x^2} + \mathbf{\Phi}^T \kappa \mathbf{\Phi} dx \tag{7.8}$$

The limits x_e refer to the element end points. At the boundaries additional stiffness and damping is added to the system to equivalate the section forces:

$$\begin{bmatrix} Q_b(t) \\ M_b(t) \end{bmatrix} = \mathbf{K}_b \begin{bmatrix} u_b(t) \\ \theta_b(t) \end{bmatrix} + \mathbf{C}_b \begin{bmatrix} \dot{u}_b(t) \\ \dot{\theta}_b(t) \end{bmatrix} \tag{7.9}$$

The boundary stiffness and damping matrix are calculated from the frequency response matrix, denoted $\mathbf{B}(\omega)$ in [Andersen, 2006]:

$$\mathbf{K}_b = \Re(\mathbf{B}(\omega_1)), \qquad \mathbf{C}_b = -\frac{1}{\omega_1}\Im(\mathbf{B}(\omega_1)) \tag{7.10}$$

In this method, the interface is calibrated for one frequency only ω_1 and if the response has a different frequency some reflection will occur. The frequency response matrix relates the amplitude of the deformation to the amplitude of the section forces and at the right side of the model the frequency response matrix is calculated from:

$$\mathbf{B}(\omega_1) = \mathbf{L}_1^+ (\mathbf{L}_0^+)^- 1 \quad \text{for} \quad x_b > 0 \tag{7.11}$$

$$\mathbf{L}_0^+ = \begin{bmatrix} 1 & 1 \\ k_3^a - ik_3^p & k_4^a - ik_4^p \end{bmatrix}, \quad \mathbf{L}_1^+ = -EI \begin{bmatrix} (k_3^a - ik_3^p)^3 & (k_4^a - ik_4^p)^3 \\ (k_3^a - ik_3^p)^2 & (k_4^a - ik_4^p)^2 \end{bmatrix} \tag{7.12}$$

A similar expression can be obtained for the left side of the beam. The 2×2 boundary matrices are added to the global system matrix at the associated degrees of freedom.

7.3 Model validation

In order to validate the boundary conditions a relatively large model is compared to a small section of the same model with transmitting boundary conditions. The concept is illustrated in Figure 7.4.

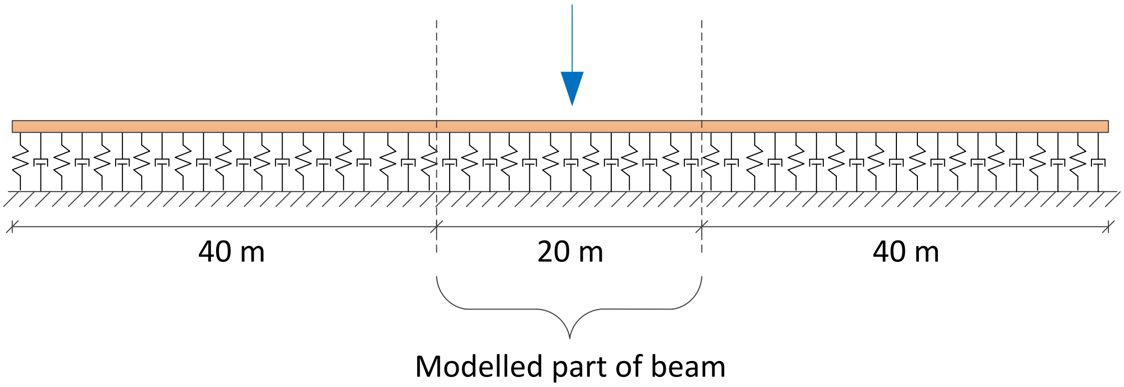

Figure 7.4. Model for validation of TBC.

The properties of the beam, the foundation etc. is irrelevant to the validation. Initially the analytical solution is calculated and for $t = 0$ the displacement field is given in Figure 7.5.

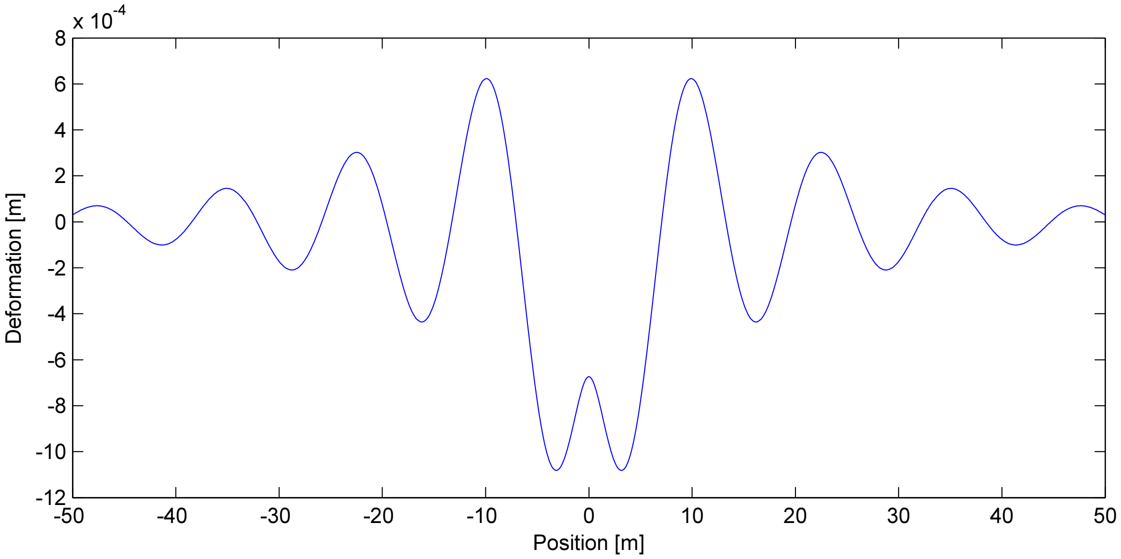

Figure 7.5. Analytical solution for the displacement field at $t = 0$.

If the total beam is modelled with fixed supports, some reflection will occur at the boundary, but due to damping in the foundation, the reflected waves will not influence the central part of the beam. A 100 meter long model with fixed supports should therefore give the same result as a similar 20 meter beam with TBC, if the model is correct. Both models are computed and the vertical displacement at the boundary of the small section is plotted in Figure 7.6. The section is modelled with free boundaries as well for comparison.

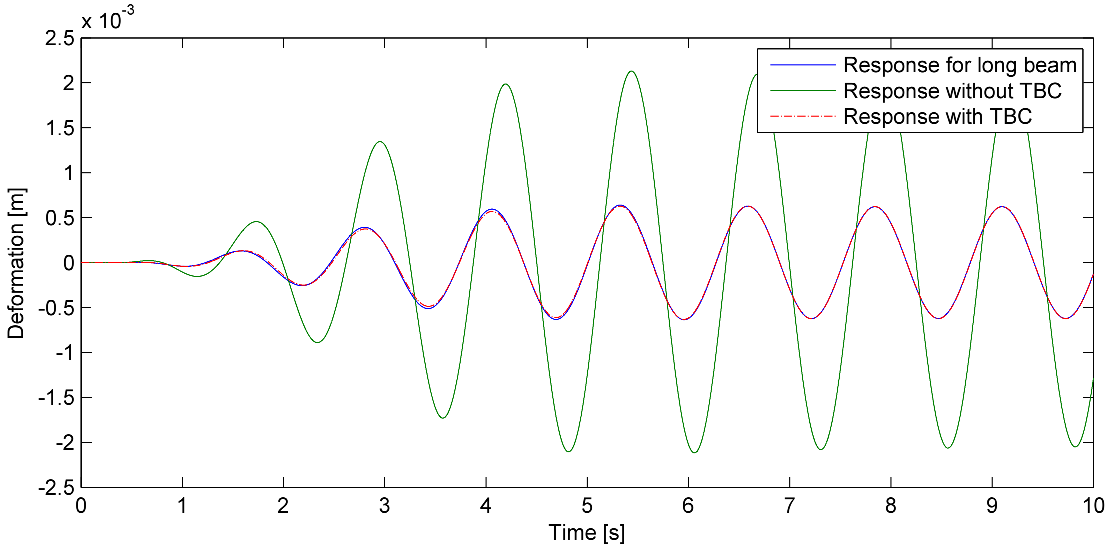

Figure 7.6. Vertical deformation at section end node.

As illustrated the deformation is the same for the 100 m beam and the 20 m section with TBC and it can hereby be concluded that the model is accurate when the boundaries are calibrated to the load frequency.

7.4 Interface elements

In the global FE model the road will partially be supported by Kelvin supports and partially by interface elements. The Kelvin supports are used at location where a direct transmission of loads in the road to the soil is undesirable, e.g. right beneath the building. The location of Kelvin supports and interface elements are illustrated in Figure 7.7.

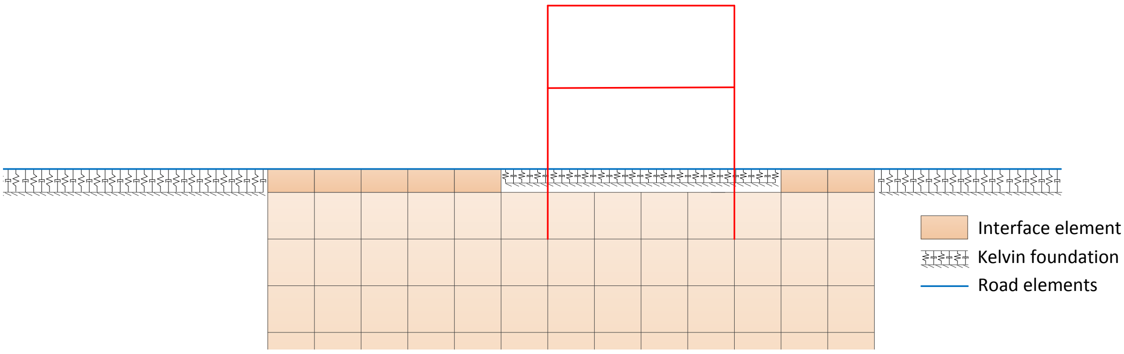

Figure 7.7. Location of Kelvin foundations and interface elements.

The interface elements will be designed to uphold the same properties as the Kelvin foundation in order to secure continuity in the road. The Kelvin foundation consists of linear vertical supports and the elements are therefore designed with six nodes and six degrees of freedom, see Figure 7.8.

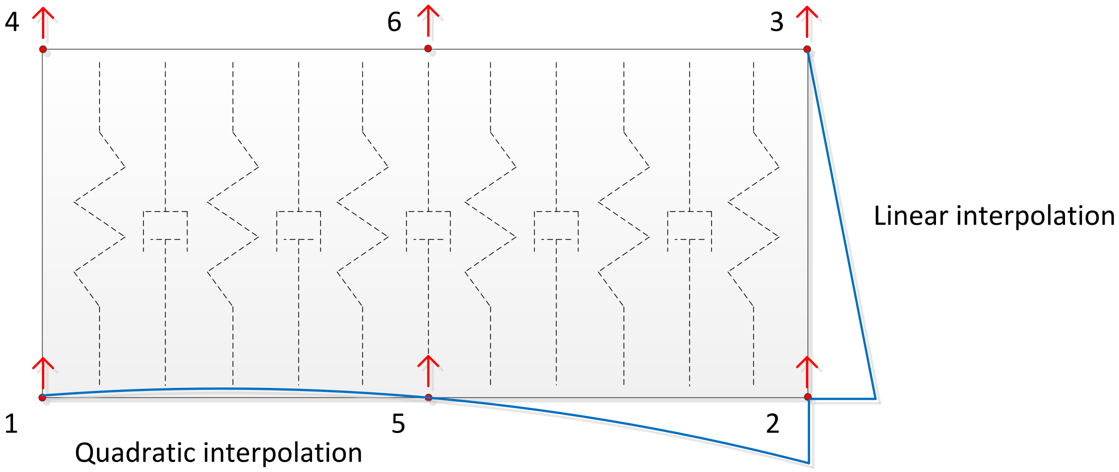

Figure 7.8. Six noded element with vertical degrees of freedom only.

The combination of linear and quadratic shape functions can be obtained by eliminating shape function 6 and 8 from the quadrilateral eight noded element. Each shape function will still be one at the associated node and zero at the other nodes as illustrated in Figure 7.9.

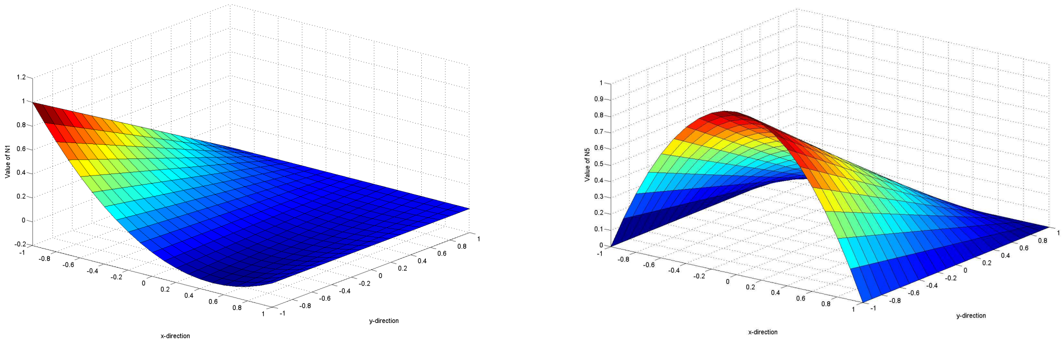

Figure 7.9. L. Interpolation value of **N**1, R. Interpolation value of **N**5.

The derivation of the element matrixes is similar to the procedure for the eight noded element except for the fact that the constitutive matrix is reduced to one parameter; the modulus of elasticity. It will be necessary to relate the parameters E and κ which can be done by considering the height and the width of the foundation, see figure 7.10.

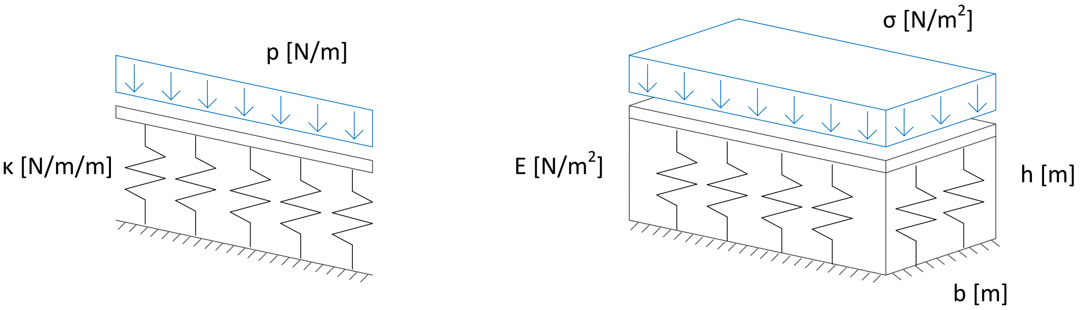

Figure 7.10. Equivalence between κ and E.

The following equations are valid:

$$\Delta h = \frac{p}{\kappa} \quad \varepsilon = \frac{\Delta h}{h} \quad \sigma = \frac{p}{b} \quad \sigma = E\varepsilon \quad \Rightarrow \quad \kappa = \frac{Eb}{h} \tag{7.13}$$

7.5 Element validation

The Kelvin model is now constructed using Bernoulli beam elements supported by interface elements, see Figure 7.11.

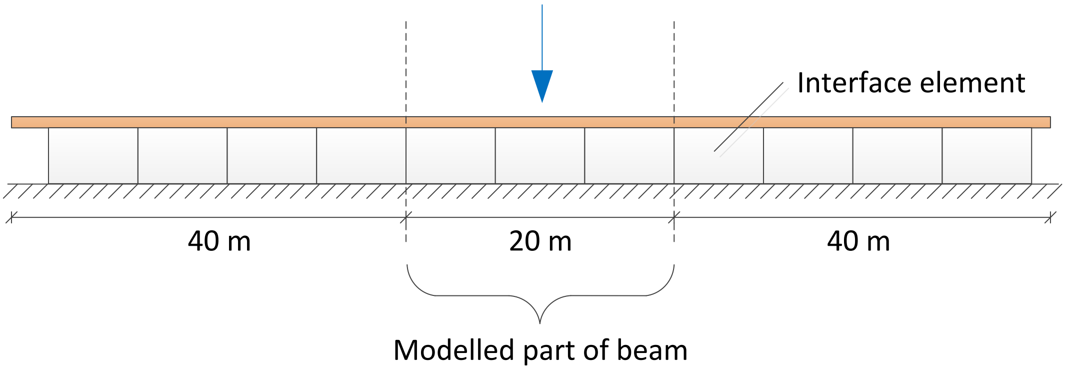

Figure 7.11. Bernoulli beam supported by interface elements.

The same assumption for harmonic load, material parameters and boundary conditions are used and a simulation is performed. The deformation of the right end node is illustrated in Figure 7.12 along with the previous results.

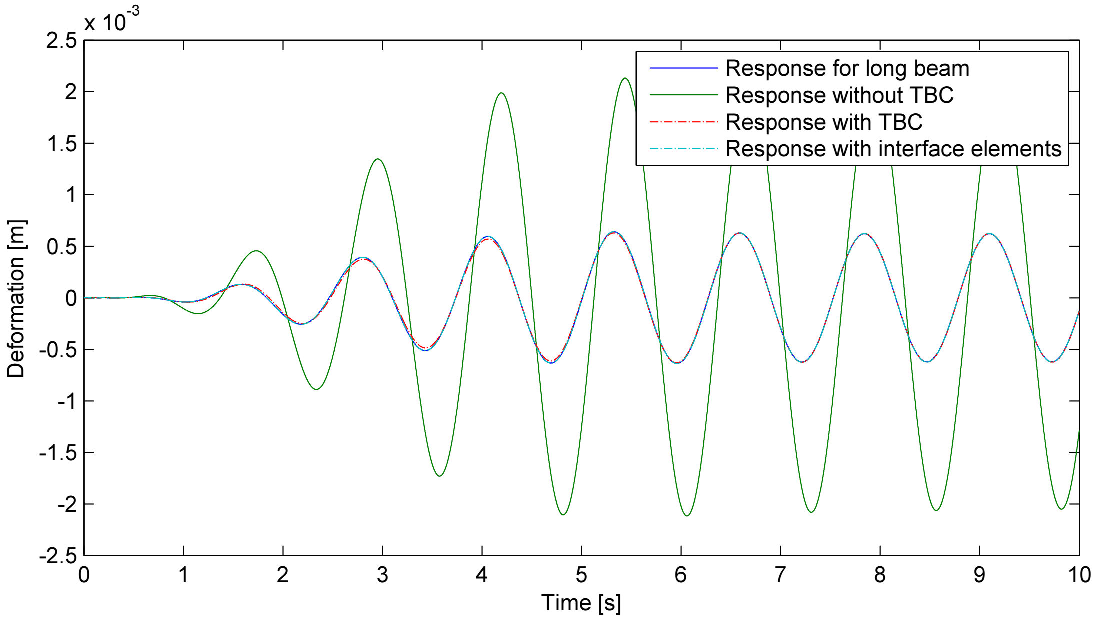

Figure 7.12. Response for Bernoulli beam on interface elements.

Evidently the response from this model is identical to the response from the Kelvin model. However, an issue arises when calibrating κ and E in the global FE model as the continuum elements below the interface elements are two dimensional. If κ is calibrated to the interface elements alone larger deformations are likely to appear at locations where the road is supported by interface and continuum elements.

7.6 Mindlin elements

The internal deformations in the continuum elements are interpolated using quadratic shape functions while the Bernoulli-Euler beam elements use cubic shape functions. When the two element types are connected, e.g. at the house-soil connection or at the road-interface connection, an issue occur as the elements may overlap or seperate between the nodes. The problem can be solved in different manners:

- Finer discretisation to reduce the error.
- Derivation of cubic shape functions for continuum elements.
- Derivation of quadratic shape functions for beam elements.

The last method will be treated using the so-called Mindlin elements. The Mindlin theory is mainly used in derivation of plate and shell elements but the theory is applicable for beams as well. The main concept is to separate the stiffness into a contribution from bending and a contribution form shear. The beam element stiffness matrices are derived according to [Cook et al., 2002]:

$$U_b = \int \int_0^L \frac{1}{2} E \varepsilon_x^2 dx \; dA = \int_0^L \frac{1}{2} EI \psi,_x^2 dx = \frac{1}{2} \{\mathbf{d}\}^T [\mathbf{k}_b] \{\mathbf{d}\} \tag{7.14}$$

$$U_s = \int \int_0^L \frac{1}{2} G \gamma_{zx}^2 dx \; dA = \int_0^L \frac{1}{2} GA_s \left(w,_x - \psi\right)^2 dx = \frac{1}{2} \{\mathbf{d}\}^T [\mathbf{k}_s] \{\mathbf{d}\} \tag{7.15}$$

The different terms in the equations above are described in [Cook et al., 2002]. The deformations w and the rotations ψ are written in terms of the nodal values $\mathbf{d}$ and the associated shape functions $\mathbf{N}$:

$$w = \mathbf{N}_1 \mathbf{d} \qquad \psi = \mathbf{N}_2 \mathbf{d} \tag{7.16}$$

As an example the derivation of the shear stiffness is given below.

$$\begin{aligned}
&\int_0^L \frac{1}{2} GA_s \left(w,_x - \psi\right)^2 dx = \int_0^L \frac{1}{2} GA_s \left(w,_x^2 + \psi^2 - 2 w,_x \psi\right) dx = \\
&\int_0^L \frac{d}{dx}\mathbf{N}_1\mathbf{d} \; \frac{1}{2} GA_s \; \frac{d}{dx}\mathbf{N}_1\mathbf{d} + \mathbf{N}_2\mathbf{d} \; \frac{1}{2} GA_s \; \mathbf{N}_2\mathbf{d} - 2\frac{d}{dx}\mathbf{N}_1\mathbf{d} \; \frac{1}{2} GA_s \; \mathbf{N}_2\mathbf{d} \; dx = \\
&\int_0^L \mathbf{d}^T\mathbf{B}_1^T \; \frac{1}{2} GA_s \; \mathbf{B}_1\mathbf{d} + \mathbf{d}^T\mathbf{N}_2^T \; \frac{1}{2} GA_s \; \mathbf{N}_2\mathbf{d} - 2\mathbf{d}^T\mathbf{B}_1^T \; \frac{1}{2} GA_s \; \mathbf{N}_2\mathbf{d} \; dx
\end{aligned} \tag{7.17}$$

By comparison of equation (7.15) and (7.17) an expression for the shear stiffness can be derived:

$$\mathbf{k}_s = \int_0^L \mathbf{B}_1^T \; GA_s \; \mathbf{B}_1 + \mathbf{N}_2^T \; GA_s \; \mathbf{N}_2 - 2 \; \mathbf{B}_1^T \; GA_s \; \mathbf{N}_2 \; dx \tag{7.18}$$

A similar derivation can be made for the bending stiffness and the result is given below:

$$\mathbf{k}_b = \int_0^L \mathbf{B}_2^T \; EI \; \mathbf{B}_2 \; dx \tag{7.19}$$

In theory any kind of shape function can be inserted as long as the fundamental properties are met.

7.7 Element validation

In order to test the Mindlin beam elements two cases are considered, as illustrated in Figure 7.13.

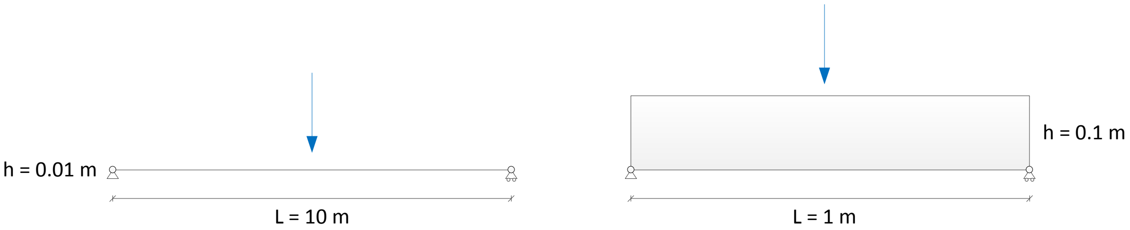

Figure 7.13. Models used for validation of Mindlin elements.

In the first model the contribution from shear is neglectable while shear deformation is likely to influence the second model. Three elements will be compared:

- Bernoulli Euler beam element
- Two noded Mindlin element with linear shape functions
- Three noded Mindlin element with quadratic shape functions

In order to demonstrate the difference between the three elements a plot is made for the first model in Figure 7.13 where the beam is discretized in four elements, see Figure 7.14.

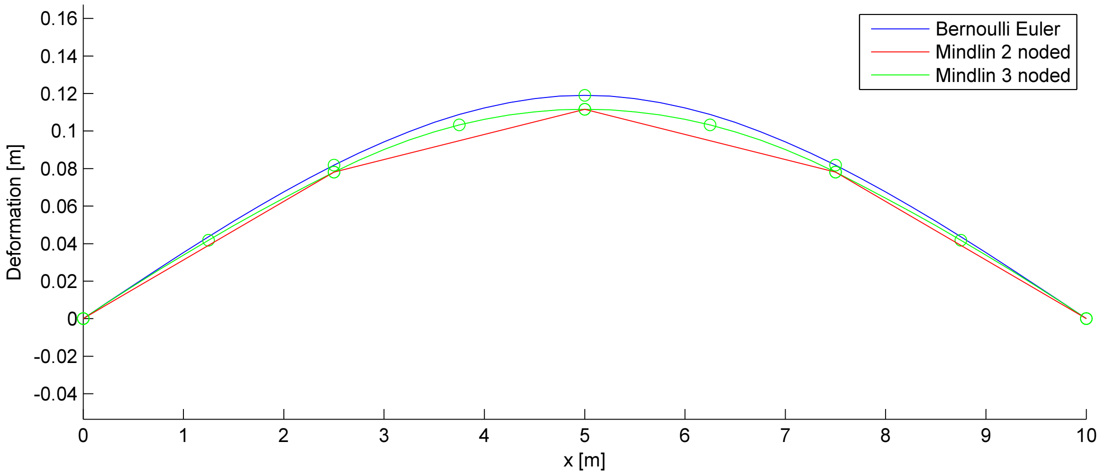

Figure 7.14. Beam deformation using four elements of different kinds.

The Bernoulli beam element provides the same result regardless of the discretisation. This, however, is not the case for the Mindlin elements and a convergence analysis is performed for both models, see Figure 7.15. The deformation of the center node is considered.

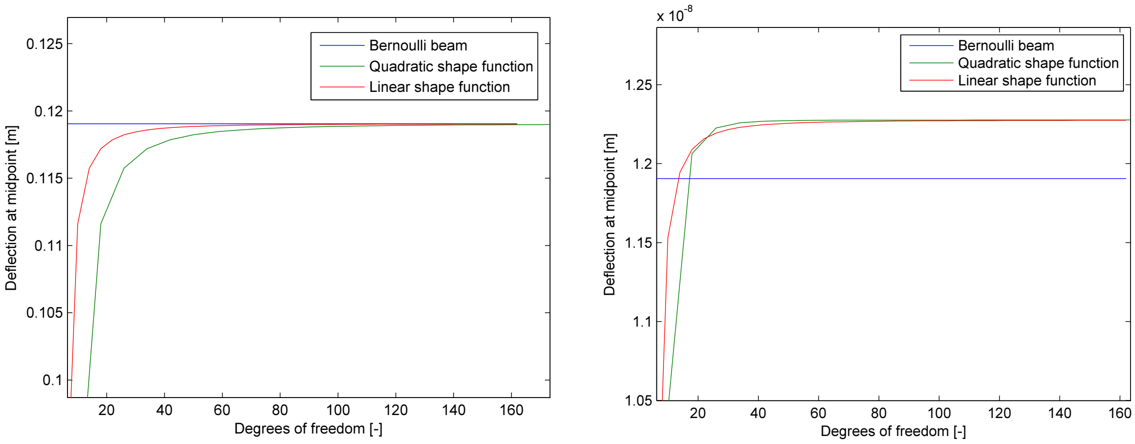

Figure 7.15. Convergence analysis for Mindlin elements L. model 1, R. model 2.

From the convergence analysis for model 1 it is evident that the two-noded element with linear shape functions converges faster than the three-noded element which contain two extra degrees of freedom per element. In model 2 shear deformation is significant and the Mindlin elements converge to a higher value than the Bernoulli element, which is expected. Furthermore it appears that the three-noded element perform better than the two-noded when shear deformation is significant.

Chapter 8

3D model

The global FE model is now expanded into a full 3D model and this chapter will briefly describe the considerations made during the construction of the model.

8.1 Three-dimensional continuum elements

The soil body is discretized by use of brick elements. The elements used are isoparametric hexahedrons with 26 nodes. The numbering of the nodes is illustrated in Figure 8.1.

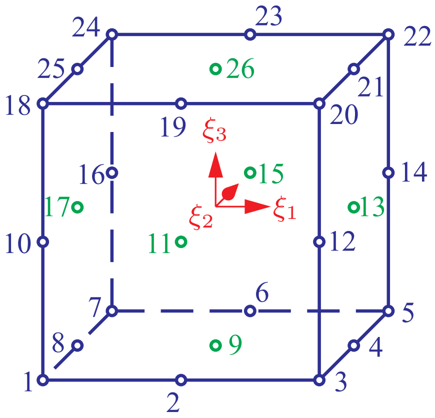

Figure 8.1. Illustration of the node ordering. [Andersen, 2002]

8.1.1 Stiffness and mass matrix

Due to the 26 nodes in the element the element stiffness matrix becomes 78 × 78. As for the 2D elements described previously the stiffness matrices are derived by use of shape functions. Shape functions can be found in [Andersen, 2002].

$$\mathbf{Ke} = \int_V \mathbf{B}^T \, \mathbf{D} \, \mathbf{B} \, dV \tag{8.1}$$

The strain interpolation matrix **B** is found from.

$$\mathbf{B} = \mathbf{H} \, \mathbf{J}_{exp}^{-1} \, \mathbf{D}_{N,exp} \tag{8.2}$$

The strain definition is made according to Huebner et al. [2001], hence the **H** matrix becomes

$$\boldsymbol{\varepsilon} = \begin{bmatrix} \varepsilon_x \\ \varepsilon_y \\ \varepsilon_z \\ 2\varepsilon_{xy} \\ 2\varepsilon_{xz} \\ 2\varepsilon_{yz} \end{bmatrix} = \begin{bmatrix} 1 & 0 & 0 & 0 & 0 & 0 & 0 & 0 & 0 \\ 0 & 0 & 0 & 0 & 1 & 0 & 0 & 0 & 0 \\ 0 & 0 & 0 & 0 & 0 & 0 & 0 & 0 & 1 \\ 0 & 1 & 0 & 1 & 0 & 0 & 0 & 0 & 0 \\ 0 & 0 & 1 & 0 & 0 & 0 & 1 & 0 & 0 \\ 0 & 0 & 0 & 0 & 0 & 1 & 0 & 1 & 0 \end{bmatrix} \begin{bmatrix} \frac{\partial u_x}{\partial x} \\ \frac{\partial u_x}{\partial y} \\ \frac{\partial u_x}{\partial z} \\ \frac{\partial u_y}{\partial x} \\ \frac{\partial u_y}{\partial y} \\ \frac{\partial u_y}{\partial z} \\ \frac{\partial u_z}{\partial x} \\ \frac{\partial u_z}{\partial y} \\ \frac{\partial u_z}{\partial z} \end{bmatrix} \tag{8.3}$$

The $\mathbf{D}_{N,exp}$ matrix is linking the partial derivatives from the parent domain to the nodal deformations in the global domain by use of shape functions.

$$\mathbf{D}_{N,exp} = \begin{bmatrix} N_{1,\xi_1} & 0 & 0 & \dots & N_{26,\xi_1} & 0 & 0 \\ N_{1,\xi_2} & 0 & 0 & \dots & N_{26,\xi_2} & 0 & 0 \\ N_{1,\xi_3} & 0 & 0 & \dots & N_{26,\xi_3} & 0 & 0 \\ 0 & N_{1,\xi_1} & 0 & \dots & 0 & N_{26,\xi_1} & 0 \\ 0 & N_{1,\xi_2} & 0 & \dots & 0 & N_{26,\xi_2} & 0 \\ 0 & N_{1,\xi_3} & 0 & \dots & 0 & N_{26,\xi_3} & 0 \\ 0 & 0 & N_{1,\xi_1} & \dots & 0 & 0 & N_{26,\xi_1} \\ 0 & 0 & N_{1,\xi_2} & \dots & 0 & 0 & N_{26,\xi_2} \\ 0 & 0 & N_{1,\xi_3} & \dots & 0 & 0 & N_{26,\xi_3} \end{bmatrix} \tag{8.4}$$

The Jacobian matrix relates the displacement derivatives in the two coordinate systems.

$$\mathbf{J} = \begin{bmatrix} \frac{\partial x}{\partial \xi_1} & \frac{\partial y}{\partial \xi_1} & \frac{\partial z}{\partial \xi_1} \\ \frac{\partial x}{\partial \xi_2} & \frac{\partial y}{\partial \xi_2} & \frac{\partial z}{\partial \xi_2} \\ \frac{\partial x}{\partial \xi_3} & \frac{\partial y}{\partial \xi_3} & \frac{\partial z}{\partial \xi_3} \end{bmatrix} = \mathbf{D}_N \left[\mathbf{X}\;\mathbf{Y}\;\mathbf{Z}\right] \tag{8.5}$$

The expanded Jacobian matrix $\mathbf{J}_{exp}$ is a 9×9 zero matrix containing $\mathbf{J}$ on the diagonal. Equation (8.1) is evaluated by use of Gauss integration. For all analysis full integration is used, hence at least 27 Gauss points are needed to derive the element stiffness matrix.

8.2 Path test

A path test is conducted to verify the stiffness matrix by use of 8 elements aligned as shown in Figure 8.2. In Figure 8.2 note that the node in the center of the model is disorientated compared to the overall grid. This is done in order to verify the Jacobian matrix.

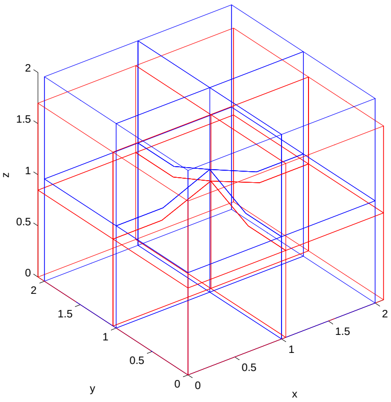

Figure 8.2. Deformed geometry

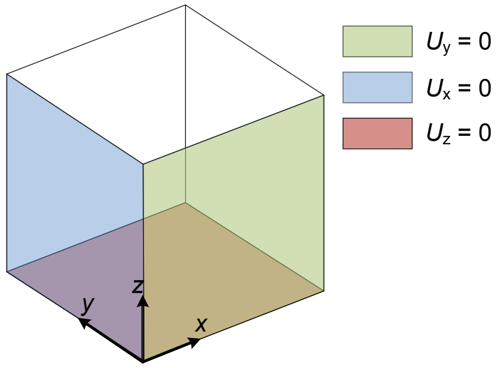

Figure 8.3. Kinematic BC

The cube is subjected to a pressure load acting on the top surface with a magnitude of $Q = 100$ Pa acting in the negativ z-direction. The cube has following material properties: $E = 1 \cdot 10^{10}$ Pa and $\nu = 0.3$

The deformation obtained from the static analysis in matlab is found as: change in height $\Delta z = -2.0 \cdot 10^{-8}$ m, change in width $\Delta x = \Delta y = 6.0 \cdot 10^{-9}$ m.

From an analytical approach the deformation of the cube is found as:

$$\Delta z = (Q/E) \cdot 2 \text{ m} = -2.0 \cdot 10^{-8} \text{ m} \tag{8.6}$$

and in the lateral direction:

$$\Delta x = \Delta y = (Q/E)\, \nu \cdot 2 \text{ m} = 6.0 \cdot 10^{-9} \text{ m} \tag{8.7}$$

It is seen that the deformations obtained from the Matlab model matches the ones from the analytical calculations. Based on the results above and a graphical inspection of the deformed mesh it is concluded that the system stiffness is correct.

8.3 Convergence

A cantilever beam with the dimensions $x = 0.1$, $y = 0.1$ and $z = 5$ with a surface load at the top acting in the y direction is analyzed with different distribution of the elements, see Figure 8.4. The load magnitude and material properties are the same as in the above example.

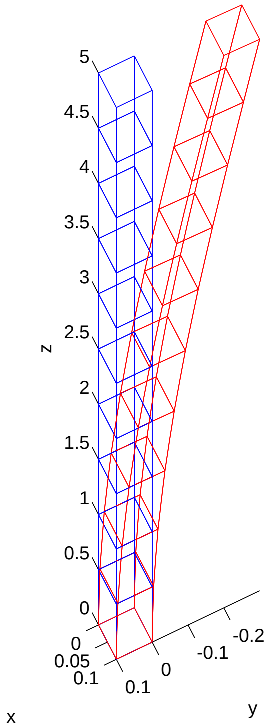

Figure 8.4. Cantilever beam

The convergensce analysis is performed with different mesh delicacy for the cross section and for the longitudinal direction. One model has 1 × 1 elements in the cross section and the other has 2 × 2. Both models have increasing elements in the longitudinal direction from 1 to 100 elements and a convergence analysis is conducted. The results for the vertical deflection is plotted in Figure 8.5.

Variation 1

$$numel = \begin{bmatrix} x:1 \\ y:1 \\ z:2 \\ total:2 \end{bmatrix} \text{ increasing to } \begin{bmatrix} x:1 \\ y:1 \\ z:100 \\ total:100 \end{bmatrix} \tag{8.8}$$

Variation 2

$$numel = \begin{bmatrix} x:2 \\ y:2 \\ z:2 \\ total:8 \end{bmatrix} \text{ increasing to } \begin{bmatrix} x:2 \\ y:2 \\ z:100 \\ total:400 \end{bmatrix} \tag{8.9}$$

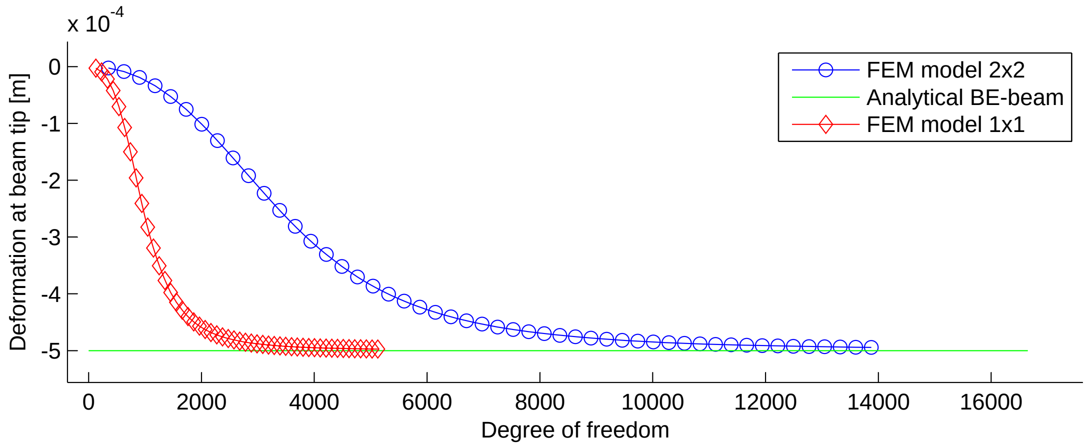

Figure 8.5. Convergence analysis of a cantilever beam model

The above example shows that refinement of the mesh in the x and y direction doesn't improve the accuracy of the calculations, but only increases the computations. In general a good result is obtained for $he \approx we \approx de$

8.3.1 Geometrical dissipation

To exam the propagation of waves in three dimensions a model is set up with a point source as illustrated in Figure 8.6. Due to symmetry only half of the soil body is created in the FE model, however, some might suggest that one quarter would be sufficient. The source of deformation is a sinusoidal load equally distributed on the face of one element. Transmitting boundary conditions are applied on four sides of the model while lateral deformations are constrained in the x-axis on the symmetry plane.

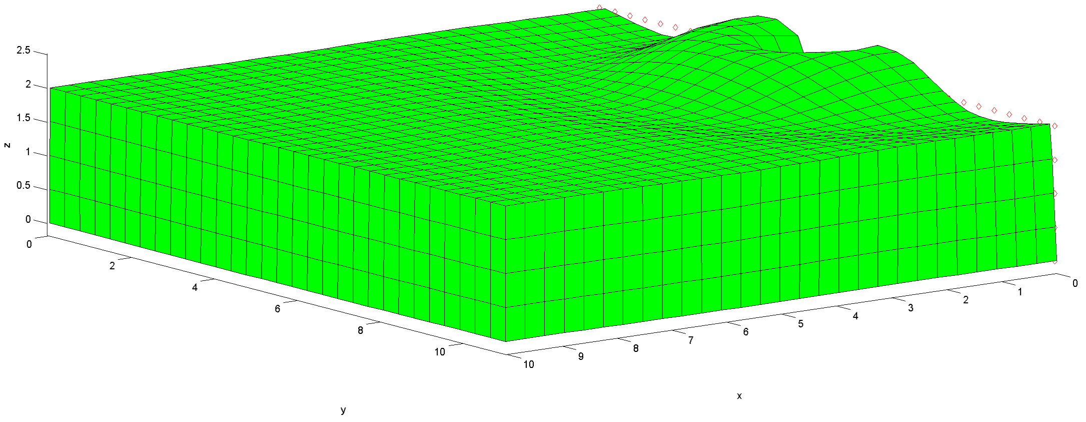

Figure 8.6. Spreading of waves in three dimensions.

Observation points at the surface along the x-axis are considered. The amplitude of the deformation in each point is plotted in Figur 8.7. The figure demonstrates how the energy dissipates. In Figure 8.7, along with the data from the FE model, an expected decay model is plotted based on geometrical expansion of an hemisphere, see Figure 8.8. The expected decay in amplitude is then found as:

$$A_2 = A_1 \frac{R_1^2}{R_2^2}, \tag{8.10}$$

for 3D and

$$A_2 = A_1 \frac{R_1}{R_2}, \tag{8.11}$$

for 2D.

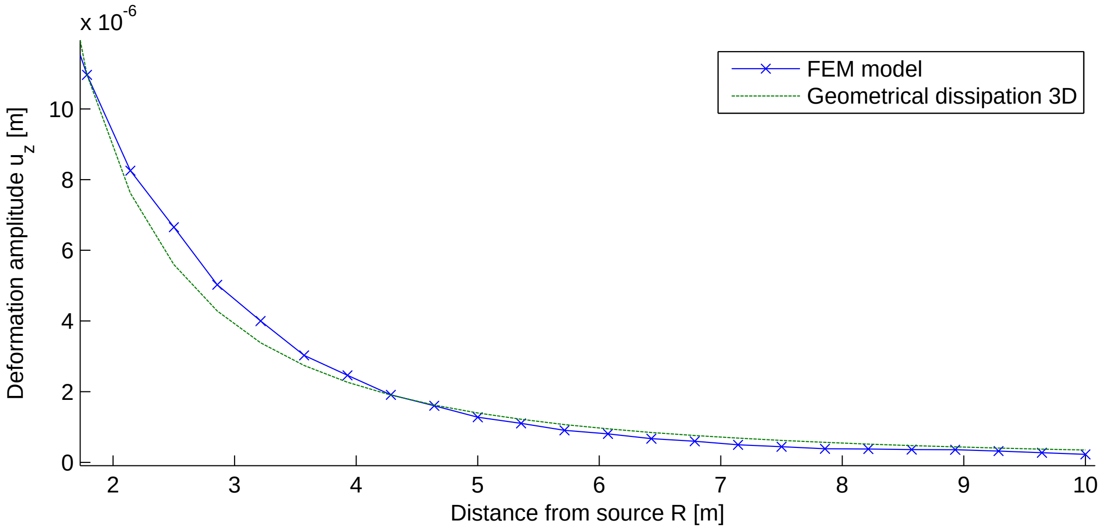

Figure 8.7. Deformation amplitude decay.

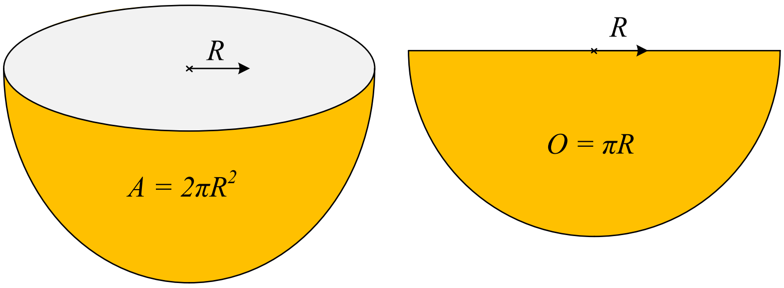

Figure 8.8. Spreading of waves.

8.4 Construction of Global 3D FE model

The model is constructed using brick elements as soil body. 3D Bernoulli beam elements are used for the building and the road is constructed using 2D Mindlin elements distributed in a grid as shown in Figure 8.9. The model in Matlab is constructed using the geometric inputs in Figure 8.9.

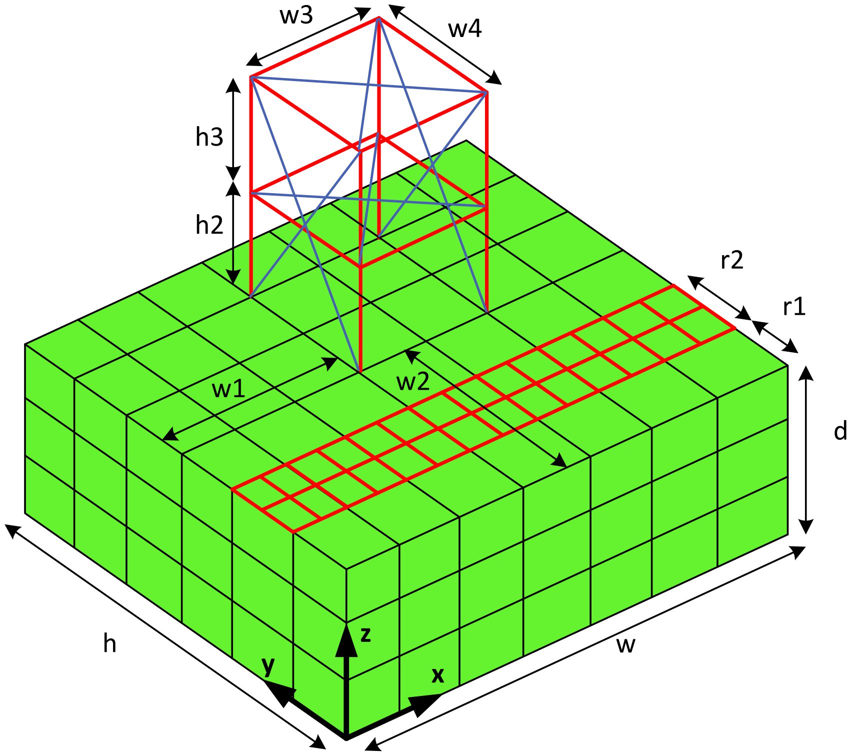

Figure 8.9. Global 3D FE model.

The road is constructed by use of Mindlin elements aligned in a grid as shown in Figure 8.10. The elements are provided with 6 degrees of freedom - two for each node. Hence the elements do not provide axial or torsional stiffness.

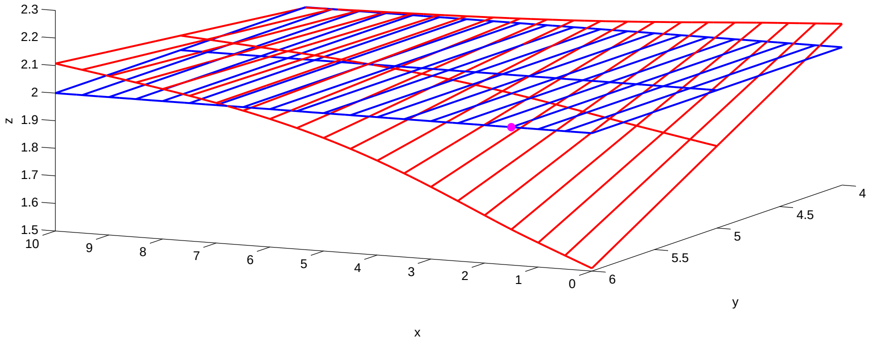

Figure 8.10. Road elements.

The three parts are assembled into the global system matrices in following order: Soil, Building, Road. Figure 8.11 illustrates where in the global stiffness matrix contribution from the different parts are located. Note that the road and building elements also share dofs with the soil and will add stiffness in some of the "blue points" as well. Regarding the road, only the rotational degrees of freedom are presented in the figure, while all the dof associated with translation are shared with the soil elements.

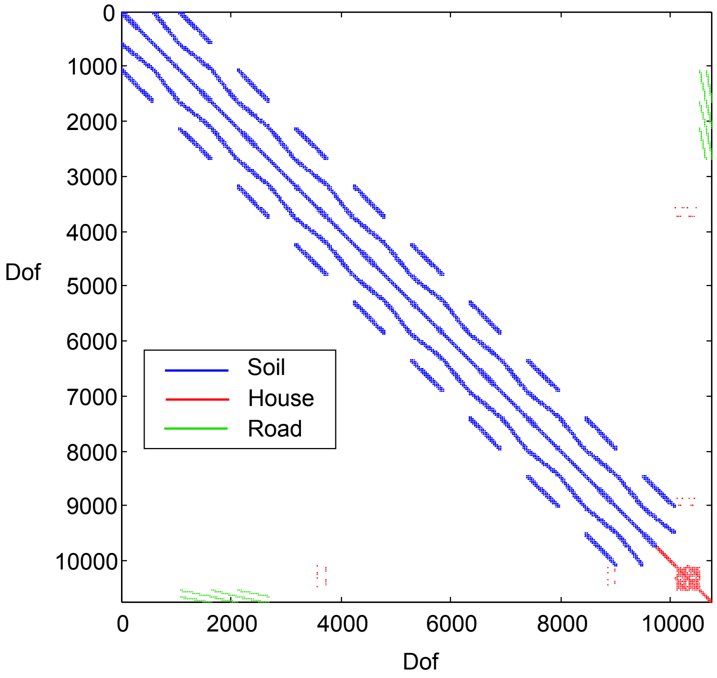

Figure 8.11. Representation of non-zero values in SysK.

8.5 Transmitting Boundary Conditions

The transmitting boundary conditions are created in accordance to Chapter 5. Changes are minor as the same principles are applied. The input vector for the absorbing boundary conditions is

$$\mathbf{SysAb} = [1 \;\; 1 \;\; 1 \;\; 1 \;\; 1 \;\; 0] \tag{8.12}$$

with side numbering according to Figure 8.12. The remaining steps are roughly the same as in Chapter 5 with exception to step 3, where a two dimensional Gauss integration over the boundary surface is performed.

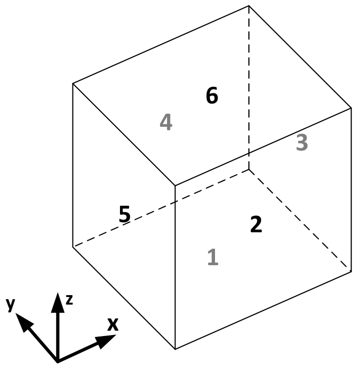

Figure 8.12. Side numbering used for boundary conditions.

Chapter 9

Evaluation of Vibrations

The scope of the following chapter is to clarify, how the vibration from traffic is evaluated and compared to the recommendations in [ISO, 1997]. The general procedure is to perform a frequency weighting to account for human response where after the root mean square of the acceleration can be used for comparison.

9.1 Frequency Weighting

In order to demonstrate the procedure a time series from a simulation and a simple time series of two sinus curves are considered. The frequency, the amplitude and the phase of the two sinus curves are:

- $f_1 = 1$ Hz $A_1 = 2$ $\Phi_1 = 0$
- $f_2 = 0.2$ Hz $A_2 = 4$ $\Phi_2 = \pi/2$

The two time series are illustrated in Figure 9.1.

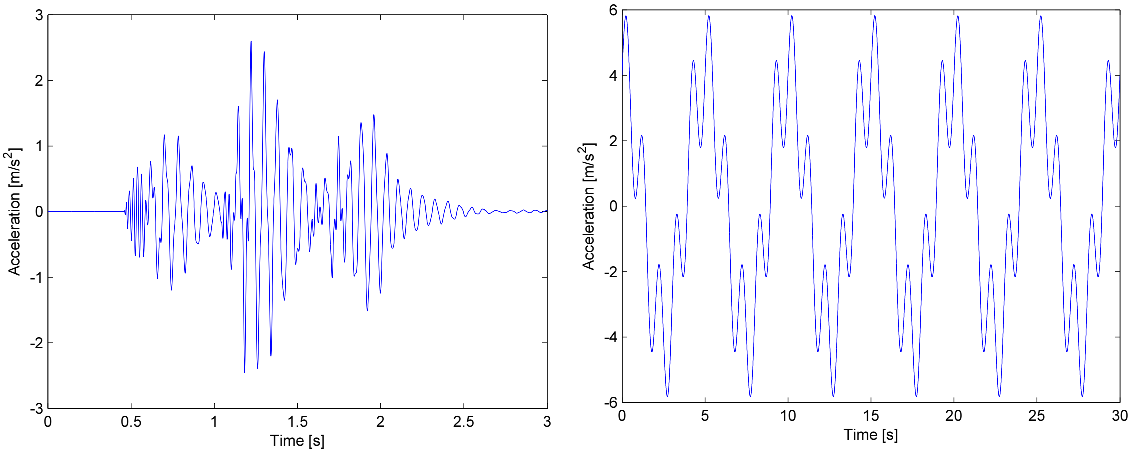

Figure 9.1. L. Time series from simulation, R. Fictive simple time series.

The accelerations are weighted according to the frequency weight functions given in [ISO, 1997]. The mathematical expressions for the three principal weighting functions are given in the appendix of the standard and plotted in Figure 9.2.

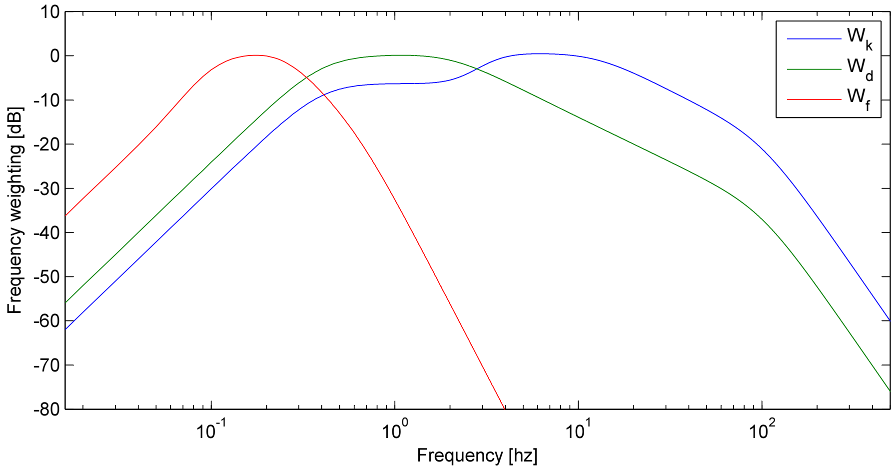

Figure 9.2. Frequency weight functions for different response types.

The weight function is selected based on the response type and the direction of vibration. In general the weight functions W_k and W_d refer to health and comfort response for the z-axis and the x- and y-axis respectively, while W_f is used for motion sickness. As illustrated the weight function for motion sickness induce a narrowing of the frequency spectrum as motion sickness occurs in a frequency range of $0.1 - 0.5$ Hz only. The weight function is expressed in decibel calculated from:

$$\Delta L_{a[dB]} = 20 \ \log_{10} \frac{a_w}{a} = 20 \ \log_{10} W_{[-]} \tag{9.1}$$

a_w denotes the weighted acceleration while $\Delta L_{a[dB]}$ expresses the change in acceleration due to frequency weighting. The weight is frequency depended and the time domain description of the accelerations are therefore converted to a frequency domain description using the following expression from [Pierce, 1994]:

$$\hat{a}(\omega) = \frac{1}{2\pi} \int_{-\infty}^{\infty} a(t) \exp^{i\omega t} dt \tag{9.2}$$

The inverse transformation is given as:

$$a(t) = \int_{-\infty}^{\infty} \hat{a}(\omega) \exp^{-i\omega t} d\omega \tag{9.3}$$

The weighted and unweighted accelerations of the time series from Figure 9.1 are plotted in Figure 9.3.

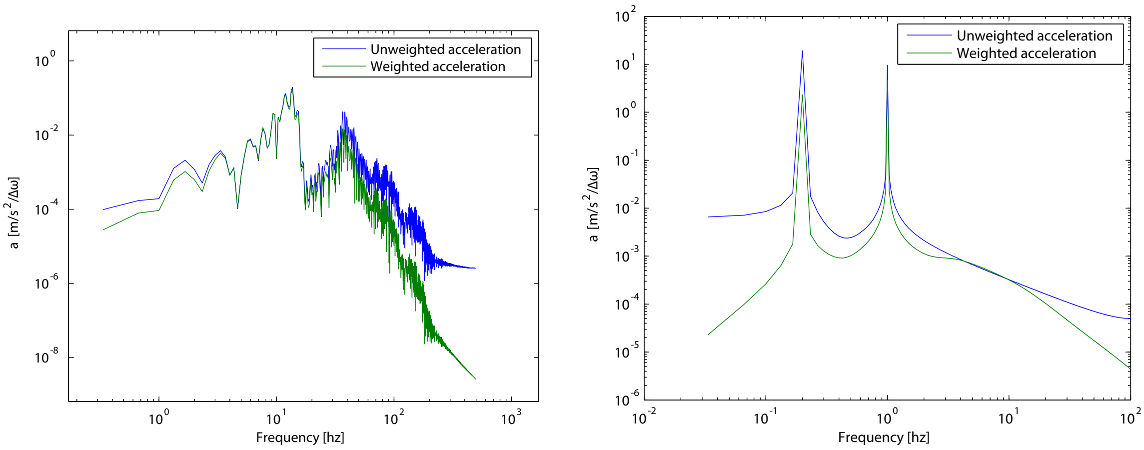

Figure 9.3. L. Frequency domain for simulation, R. Frequency domain for simple time series.

The frequency domain solution can be validated by calculating the variance of the time series, which can be done in both the frequency and the time domain:

$$\sigma_\omega^2 = \int_0^\infty a(\omega)d\omega \qquad \sigma_t^2 = \frac{1}{N}\sum_{i=1}^{N}(x_i - \mu)^2 \tag{9.4}$$

The variance is calculated for both time series using both methods, see Table 9.1. It should be noticed that $a(\omega)$ can be a complex number, whereby the integration is conducted multiplying the complex number and its complex conjugated.

Time serie	Simulation	Simple
Time domain	0.32 m/s^2	10 m/s^2
Frequency domain	0.32 m/s^2	10 m/s^2

Table 9.1. Variance of the two time series calculated from frequency and time domain.

As demonstrated, the same results are obtained in both the time domain and the frequency domain.

9.2 Frequency Bands

In acoustic and vibration engineering it is common to present vibration using frequency bands. By using bands the frequency spectrum is averaged over a range of frequencies, whereby the results are significantly easier to interpret compared to the graphs in Figure 9.3. Octave bands have the property that the ratio between the last and the first frequency of a band is 2, which cause the width of each band to be the same when a logarithmic scale is applied. One third octave bands are commonly used and have the following properties:

$$f_1 = 2^{-1/6} f_0 \qquad f_2 = 2^{1/6} f_0 \qquad f_2 = 2^{1/3} f_1 \tag{9.5}$$

f_0 denotes the center frequency of the band while f_1 and f_2 denote the lower and upper range respectively. One third octave bands are beneficial as the ratio between the centerfrequencies of band b_i and band b_{i+10} is approximately 10. The acceleration content of each band a_b can be calculated from,

$$a_b(\omega_0)^2 = \int_{\omega_1}^{\omega_2} a(\omega) d\omega, \tag{9.6}$$

where, ω_0 is the angular center frequency of the band from ω_1 to ω_2. The acceleration level for each band L_{a_b} is evaluated using,

$$L_{a_b} = 20 \ \log \frac{a_b}{\Delta\omega_b \ a_{ref}}, \tag{9.7}$$

where, $\Delta\omega_b$ is the band width. a_{ref} is an acceleration reference level stated as 10^{-6} m/s^2 in [Sound et al., 2013]. Both time series are separated in bands and the acceleration level has been calculated, see Figure 9.4.

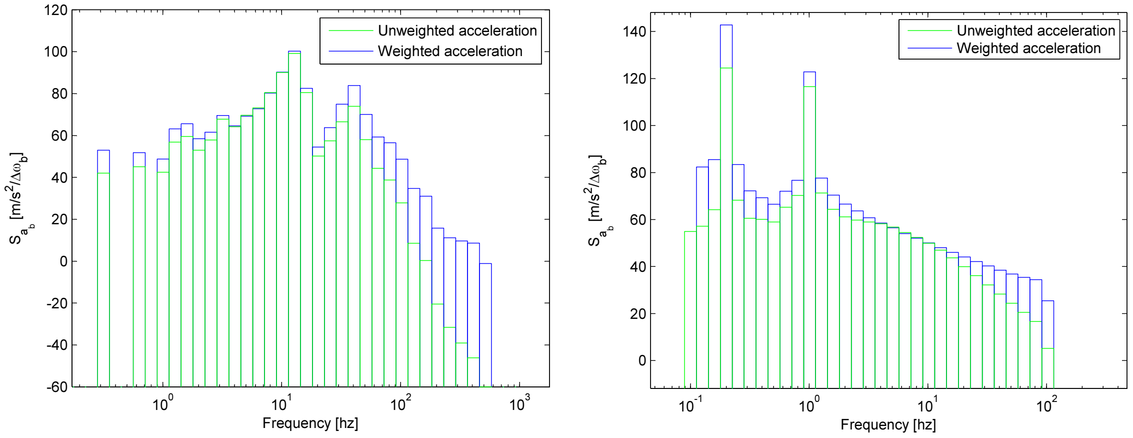

Figure 9.4. Frequency one-third octave band content for (left) Simulation, (right) Simple time series.

9.3 Maximum Transient Vibration Value

Vibration from traffic can usually be considered as occasional shocks and in such case it is recommended to evaluate the vibration using the maximum transient vibration value (MTVV) according to [ISO, 1997]. The MTVV is calculated from,

$$\text{MTVV} = \max\left(a_v(t)\right) \quad t \in [\tau; T], \tag{9.8}$$

$$a_v(t) = \sqrt{k_x^2 \ a_{wx}^2(t) + k_y^2 \ a_{wy}^2(t)}, \tag{9.9}$$

$$a_w(t_0) = \left\{ \frac{1}{\tau} \int\limits_{t_0-\tau}^{t_0} \left[a_w(t)\right]^2 dt \right\}^{\frac{1}{2}}, \tag{9.10}$$

As indicated a running r.m.s. value is used in which τ is set to one second according to [ISO, 1997]. The expression for calculation of $a_w(t_0)$ is only useful if the frequency weighted acceleration is transformed back into the time domain. This operation is unnecessary since,

$$a_{r.m.s.}^2 = \mu_a^2 + \sigma_a^2. \tag{9.11}$$

The mean value of the acceleration is zero whereby the r.m.s. of the acceleration is equal to the standard deviation. Ultimately the frequency weighted r.m.s. acceleration $a_w(t_0)$ can be calculated from:

$$a_w(t_0) = \left[\sum_i (W_i a_i)^2 \right]^{\frac{1}{2}} \tag{9.12}$$

Bibliography

Andersen, **2002**. Lars Andersen. *Wave propagation in Infinite Structures and Media.* Aalborg University, first edition edition, 2002.

Andersen, **2006**. Lars Andersen. *Linear Elastodynamic Analysis.* Aalborg University, third edition edition, 2006.

Andersen, **2012**. Lars Vabbersgaard Andersen. *Lecture 3 - Soil Dynamic in Finite Element Analysis*, 2012.

Cook, Malkus, Plesha, and Witt, **2002**. Robert D. Cook, David S. Malkus, Michael E. Plesha, and Robert J. Witt. *Concepts and Applications of Finite Element Analysis.* John Wiley and Sons, INC, fourth edition edition, 2002.

Henchi, Fafard, Talbot, and Dhatt, **1997**. K. Henchi, M. Fafard, M. Talbot, and G. Dhatt. *An Efficient Algorithm for Dynamic Analysis of Bridges under Moving Vehicles using a Coupled Modal and Physical Components Approach.* 1997.

Huebner, Dewhirst, Smith, and Byrom, **2001**. K. Huebner, D. Dewhirst, D. Smith, and T. Byrom. *The finite element methods for engineers.* 2001.

ISO, **1997**. ISO. *Mechanical vibration and shock - Evaluation of human exposure to whole-body vibration*, International Organization For Standardization, 1997.

Jensen, **2012**. Bjarne Chr. Jensen. *Teknisk Staabi.* 2012.

Kima, Kawatania, and Kimb, **2005**. Chul Woo Kima, Mitsuo Kawatania, and Ki Bong Kimb. *Three-dimensional dynamic analysis for bridge/vehicle interaction with roadway roughness.* 2005.

Nielsen, **2004**. Soeren R. K. Nielsen. *Vibration Theory, Vol. 1.* 2004.

Pierce, **1994**. Allan D. Pierce. *Acoustics - An Introduction to Its Physical Principles and Applications.* Acoustical Society of America, third edition edition, 1994.

R.B.J. Brinkgreve, W.M. Swolfs, **2011**. E. Engin R.B.J. Brinkgreve, W.M. Swolfs. *Plaxis - Scientific Manual*, 2011.

Sound, Hire, and Specialists, **2013**. The Sound, Vibration Instrument Hire, and Calibration Specialists. *Acoustic Glossary*, 2013. URL `http://www.acoustic-glossary.co.uk/definitions-a.htm`.

Sterner, **2009**. Joergen Sterner. *BYERNES TRAFIKAREALER - Haefte 7 Fartdaempere*, Vejdirektorated, 2009.